DEVELOPMENT AND ANALYSIS OF A 100 MEV PROTON BEAM FACILITY

by

Peer M. Portner

A thesis submitted to the Faculty of Graduate Studies and Research of McGill University in partial fulfillment of the requirements for the degree of Master of Science.

Foster Radiation Laboratory,
McGill University,
Montreal.

August, 1964.

TABLE OF CONTENTS	Page
Abstract	i
Acknowledgement	ii
List of Figures	iii
List of Plates and Tables	v
Chapter 1 - Introduction	1
Chapter 2 - Theory of Magnetic Deflection and	
Focusing Systems	
2.1 Introduction	3
2.2 Drift Space	5
2.3 The Magnetic Quadrupole	5
2.4 Uniform Field Bending Magnet	11
2.5 Fringing Fields in Quadrupoles and	
Bending Magnets	21
2.6 Use of Transfer Matrices in Tracing Particle	
Trajectories	22
2.7 The Phase Space Ellipse	23
Chapter 3 - The External Beam Transport System	
3.1 General Requirements	27
3.2 Section to the Entrance of the 28^{0} Bending	
Magnet	28
3.3 Deflection Into Beam Hall	38
3.4 Transport Into Beam Hall	44
3.5 Magnet Power Supplies	46

3.6 Summary of Magnet Properties

Chapter 4 - Momentum Analysis of the Proton Beam

3.7 Performance of the Beam Transport System

47

47

TABLE OF	CONT	ENTS	Page
	4.1	Introduction	56
	4.2	Experimental Apparatus and Procedure	61
	4.3	Experimental Range-Energy Results	70
	4.4	Determination of the Energy and Energy Spread	
		of the External Beam	77
Chapter	5 -	Conclusion	81
Bibliogr	aphy		86

ABSTRACT

This thesis describes the design, installation, and analysis of the external beam transport system of the McGill Proton Synchrocyclotron.

A review of the basic theory of magnetic deflection and focusing systems is also presented.

The extraction system has been optimized and a final beam intensity of 2.5 x 10^{-8} amperes obtained, for an extraction efficiency of 2.7%.

The floating wire technique has been successfully used in the momentum analysis of the external beam. A point on the range energy curve for aluminum has been established with high precision at 99.88 ± 0.06 MeV corresponding to a range of 9814 ± 7 mg/cm² in pure aluminum. This point has been used to calibrate a range energy measurement of the external beam and the beam has been found to have an energy of 100.0 MeV and an energy spread of 0.33 MeV (full width at half maximum).

ACKNOWLEDGEMENT.

The expansion of the laboratory facilities allowing the development of a well behaved external beam system was largely due to the efforts of Professor R. E. Bell, Director of the laboratory.

The engineering of the beam transport system was carried out primarily by Dr. W. T. Link in collaboration with Dr. R. B. Moore and Dr. W. R. Frisken. The author would like to acknowledge the continued support of these men in the development and analysis of the system.

In measurements on range energy, the moral support, guidance, and generous help of Dr. Moore are gratefully acknowledged.

Thanks are due to Mr. S. Doig and the machine shop for excellent work done, often at short notice, on vacuum system hardware and general beam handling equipment.

The design and development of the magnet power supplies by Dr. J. Crawford is acknowledged, and Mr. P. Kirkby is thanked for the use of his Faraday Cup.

Presently at Brookhaven National Laboratories

LIST OF FIGURES

Figure		Page
1.	Magnetic Quadrupole Lens	6
2.	Principal Planes and Focal Points of Quadrupole	6
3.	Beam Envelope in Quadrupole Doublet	12
4 a	Geometry of a Simple Wedge Magnet	14
4b	Constructions for Calculating Trajectories in a	
	Simple Wedge Magnet (No Vertical Focusing)	14
5.	Rotation of Exit Pole Edge	17
6.	Non-Normal Entry Through the Fringing Field of a	
	Wedge Magnet	19
7.	Phase Space Ellipses	25
8.	Layout of the Beam System	29
9.	System Apertures	31
10.	Beam Intensity Variation with Regenerator Strength	33
11.	Emittance Plots at $z = 160$ "	37
12.	Faraday Cup External Beam Monitor	39
13.	Beam Intensity Profiles at Trimming Slits ($z = 133$ ")	41
14.	Shimming of 28° Bending Magnet	42
15.	Excitation Curves	48
16.	Beam Envelope Through Deflection System	51
16 a	Horizontal Phase Space Ellipses	52
17.	Experimental Layout for Range Energy Measurement	62
18.	The Balance Frame	66
19.	Floating Wire Current Regulator	69
20	Poncil Roam Profile	71

(iv)

Figure		Page	
21.	Range Curve for Aluminum	73	
22.	Theoretical Range Energy Curves	70	
23.	Range in Aluminum of Total Beam	78	
24.	Beam Energy Spread	79	

LIST OF PLATES AND TABLES

Plate		Page
1.	Beam Pictures	35
2.	Beam Pictures at Points Through the Transport	
	Deflection System	36
3.	The Balance Frame Used in the Floating Wire Measurement	67
4.	Beam Exit From the Cyclotron	82
5.	The Thin Collimator, Trimming Slits, and Faraday Cup	83
6.	The Deflection Magnets	84
7.	Switching and Focusing Facility in the Beam Hall	85
1	able (able	Page
ı.	Coordinates z of elements in System	30
2.	Bending Magnet Parameters	48a
3.	Quadrupole Parameters	48a
4.	Transfer Matrices for Deflection System	50
5.	Floating Wire Energy Calibration	74

1. INTRODUCTION.

In the fall of 1961 an intense external beam was successfully extracted from the McGill 82" proton Synchrocyclotron using the principle of magnetic regenerative deflection (Moore, 1962). This beam had an average intensity of 4×10^{-9} amperes or 2.5×10^{10} protons/sec, and a pulsed time structure of $15 \mu sec$. bursts at a repetition rate of 400 per second.

In order to make the best use of this external beam, it was decided to incorporate an extension to the cyclotron vault in a general expansion of the Laboratory. The addition to the cyclotron vault was to be a large experimental area, well-shielded from the cyclotron, and out of the direct line of neutron flux produced in the beam extraction process.

During the initial, planning stage, both internal and external beam facilities were used for research. A temporary transport system utilizing available equipment was described by Barton and McPherson (1963). Construction on the building extension was started in December 1962 and completed in May, 1963. The new beam transport system was operational by November 1963.

It was felt at this time that an accurate determination of the energy of the external beam would be of value, since the available method of energy measurement using the theoretical range-energy relationship yielded uncertainties of the order of two percent.

This thesis, then, describes the design and installation of the external beam transport system of the McGill Synchrocyclotron

and a precise, absolute determination of the energy and energy spread of the external beam.

2. THEORY OF MAGNETIC DEFLECTION AND FOCUSING SYSTEMS

2.1 Introduction

The use of an external beam of charged particles from an accelerator necessitates a transport system to deliver the beam to the experimental location. In most nuclear experiments, it is desirable to have a well defined beam of small cross-sectional area and small momentum-spread. A transport system typically provides: deflection, focusing, and momentum analysis and the methods of forming such beams comprises beam, or particle optics. Surveys of the techniques of beam transport have been given by Luckey (1961), Chamberlain (1960), and de Raad (1963).

Beam optics involves the study of systems using electromagnetic forces to define the paths of charged particles. The simplest and most practical systems at medium and high energies use purely magnetic fields: deflection and momentum—analysis being obtained with bending magnets and focusing with quadrupole magnets. (Electrostatic focusing becomes impractical at high energies due to the excessively high fields required).

Particle beams are usually characterized by small displacement, angular spread and momentum spread. When these criteria are satisfied, first order theory for the equations of motion can be used, and by definition the equations of the trajectories become linear in these three parameters (displacement, angular and momentum spreads). The calculation of trajectories and of the properties of magnetic systems then lends itself ideally to matrix formalism as developed by Penner (1961). Second-and higher-order theories to correct for aberrations not accounted

for in the first-order theory can be found in the literature (Brown et al, 1964), but will not be considered here.

In designing a beam transport system the first assumption is the existence of a "central" ray with magnetic rigidity equal to the average magnetic rigidity of the accelerator beam (or a particle with momentum equal to the average momentum of the particles of the beam) whose trajectory coincides with the central path through the system. An arbitrary ray is then specified at any point in the system by giving the position along the optic axis z, the perpendicular displacements x, y, from the axis, the corresponding conjugate momenta (x' = dx/dz, y' = dy/dz) and the momentum difference $\Delta p/p$ between the particles making up this ray and those of the central ray of the system. (By convention x, y, z, form a left handed coordinate system). Finally each particle is assumed to have a constant velocity in the z direction v_z since the angular displacement is small and v_z can therefore be considered equal to v the total velocity.

In the following sections the equations of motion of the particles in a beam are derived for a drift space, a magnetic quadrupole and a uniform-field bending magnet. Use of the matrix method in tracing trajectories of these particles is shown; and the concept of phase space representation of the total beam is presented. Much of the theory presented here can be found in the literature and reference has been made to several sources. In general, however, most references do not cover uniformly all parts of the theory and it was felt that a more comprehensive review in an integral form would be useful.

2.2 Drift Space

In a drift space, or field free region particles in the beam experience no forces. If at position z=0, a particle has coordinates (x_0, x_0') ; at $z=\ell$ the coordinates will be $(x_0 + x_0'\ell, x_0')$. This can be simply expressed in matrix formalism by introducing the three dimensional position vector for the particle:

The matrix equation for a drift space is then:

$$\begin{bmatrix}
x \\
x' \\
\underline{\Delta p} \\
\overline{p}
\end{bmatrix} = \begin{bmatrix}
1 & \ell & 0 \\
0 & 1 & 0 \\
0 & 0 & 1
\end{bmatrix} \begin{bmatrix}
x_0 \\
x_0' \\
\underline{\Delta p} \\
\overline{p}
\end{bmatrix}$$
(1)

A similar relationship holds for the y,z plane (conventionally the vertical plane).

2.3 The Magnetic Ouadrupole

The geometry and field pattern for a magnetic quadrupole are shown in Fig. 1, the z axis representing the optic axis and x and y the horizontal and vertical directions respectively. The quadrupole field is created by making the pole pieces rectangular hyperbolic cylinders which are symmetrical about the x,z and y,z planes. If adjacent poles have opposite polarity as shown, the field gradients are constant and the force on a charged particle is proportional to its displacement from the optic axis. This can be shown as follows: Within the region of the quadrupole lens, Maxwell's equations give

FIGURE 1:

MAGNETIC QUADRUPOLE LENS

The geometry of the pole tips and field lines is shown.

FIGURE 2:

PRINCIPAL PLANES AND FOCAL POINTS OF QUADRUPOLE

The symbols are explained in the text.

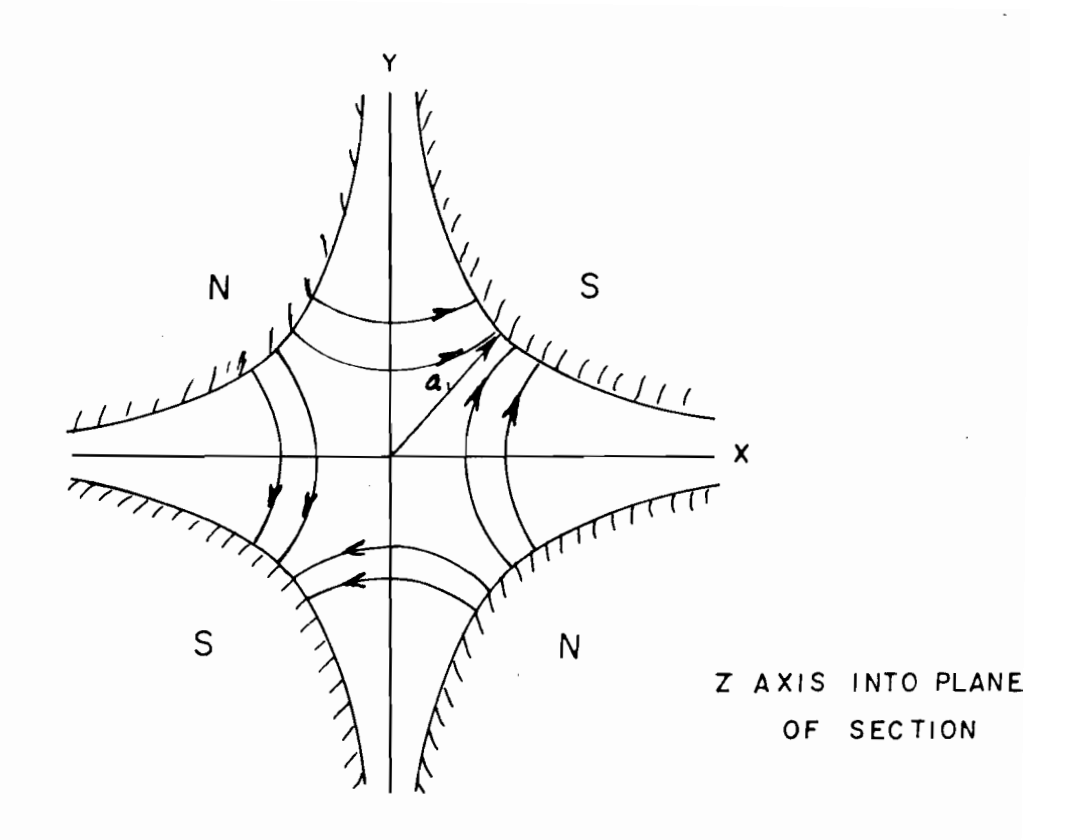


FIG I - MAGNETIC QUADRUPOLE LENS

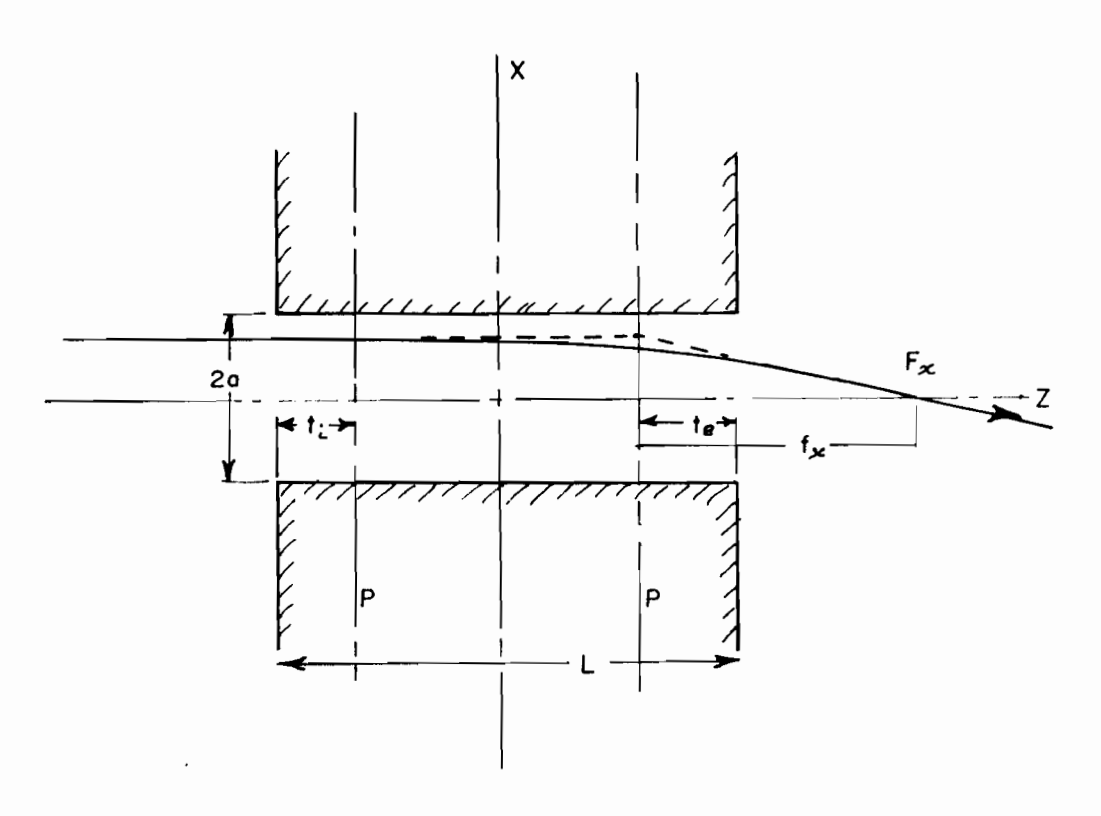


FIG 2 - PRINCIPAL PLANES AND FOCAL POINTS
OF QUADRUPOLE

curl
$$B = 0$$
,

or
$$\frac{\partial B_x}{\partial y} = \frac{\partial B_y}{\partial x}$$

which in the first (and linear) approximation gives

$$B_{X} = ky$$
and
$$B_{Y} = kx$$
 (2)

where k is the field gradient of the quadrupole.

Now consider the scalar potential V;

$$V = \int_a^b \vec{H} \cdot d\vec{s}$$

where
$$\vec{H} = \frac{\vec{B}}{\mu_0} = \frac{1}{\mu_0} (\vec{i}B_X + \vec{j}B_y)$$

then:
$$V = \frac{1}{\mu_0} \int_a^b (B_x dx + B_y dy) = \frac{k}{\mu_0} \int_a^b (y dx + x dy)$$

and choosing V at the centre of the quadrupole to be zero:

$$V = \frac{k}{\mu_0} \int_0^{X_2} (y dx + x dy) = \frac{k}{\mu_0} XY$$

This obviously implies hyperbolic equipotential lines, and the pole pieces of quadrupoles are assumed to be of high enough permeability (non-saturated) that their surfaces are magnetic equipotentials. The equation describing the pole face of the quadrupole is in fact $2xy = a^2$ where a is the aperture radius shown in Fig. 1.

The Lorentz force components in the \boldsymbol{x} and \boldsymbol{y} directions are given by:

$$F_{\mathbf{x}} = -q\mathbf{v}_{\mathbf{z}}\mathbf{B}_{\mathbf{y}} = -q\mathbf{v}\mathbf{k}\mathbf{x} \tag{3}$$

and $F_v = qvky$

These equations immediately show that in this configuration the

quadrupole is focusing in the x direction and defocusing in the y direction. Polarity reversal of the quadrupole gives focusing in the y direction and defocusing in the x direction. The equations of motion for the focusing plane may be derived as follows:

$$\frac{d}{dt} (mv_X) = F_X = -qvkx$$

and since the force is entirely radial,

$$\frac{d^2x}{dt^2} + \frac{qv}{m} kx = 0$$

changing variables using the relation z = vt:

$$\frac{d^2x}{dz^2} + \frac{q}{mv} kx = 0$$

and substituting the magnetic rigidity $B\rho$ for mv/q:

$$\frac{d^2x}{dz^2} + \frac{kx}{B\rho} = 0$$

which has a solution of the form:

$$x = A\cos Kz + B\sin Kz \tag{4}$$

where $K^2 = k/B\rho$.

The derivative with respect to z of (4) gives

$$x^{\bullet} = -AKsinKz + BKcosKz$$
 (5)

The initial conditions $x = x_0$, $x' = x_0'$ when $z = z_0 = 0$ give the constants A and B in (4) and (5), and evaluating at z=L, the length of the quadrupole, gives the equations of motion in the horizontal plane:

$$x = x_0 \cos KL + \frac{x_0^*}{K} \sin KL$$

$$x^* = -x_0 K \sin K L + x_0^* \cos K L$$
 (6)

Similarly the equations of motion in the y plane are given by:

$$y' = y_0 \cosh KL + \frac{y_0'}{K} \sinh KL$$

$$y' = y_0 K \sinh KL + y_0' \cosh KL$$
(7)

Equations (6) and (7), being linear, may be rewritten in matrix form.

$$\begin{pmatrix} x \\ x' \end{pmatrix} = M_F \begin{pmatrix} x_0 \\ x_0' \end{pmatrix} \quad \text{and} \quad \begin{pmatrix} y \\ y' \end{pmatrix} = M_D \begin{pmatrix} y_0 \\ y_0' \end{pmatrix}$$

where the transfer matrices \mathbf{M}_{F} in the focusing plane and \mathbf{M}_{D} in the defocusing plane are given by:

$$M_{F} = \begin{cases} \cos KL & \frac{1}{K} \sin KL \\ -K \sin KL & \cos KL \end{cases}$$

$$M_{D} = \begin{cases} \cosh KL & \frac{1}{K} \sin hKL \\ K \sin hKL & \cosh KL \end{cases}$$
(8)

The quadrupole can be represented by a thick lens with principal planes P_i , P_e as shown in Fig. 2. The entrance principal plane P_i is a distance t_i after the magnet entrance and the exit principal plane a distance t_e before the magnet exit. The transfer matrix for the thick lens (Penner, 1961) is:

$$M = \begin{pmatrix} 1 & t_e \\ 0 & 1 \end{pmatrix} \begin{pmatrix} 1 & 0 \\ -1/f & 1 \end{pmatrix} \begin{pmatrix} 1 & t_i \\ 0 & 1 \end{pmatrix}$$

$$(9)$$

where f is the lens focal length. The optical properties of the quadrupole are then simply obtained by equating the matrix of (9) with those of (8), and are summarized here:

for the focusing plane:

$$f = 1/(KsinKL)$$

$$t_i = t_e = (1-cosKL)/(KsinKL)$$
(10)

and for the docusing plane:

$$f = -1/(KsinhKL)$$

$$t_i = t_e = (coshKL-1)/(KsinhKL)$$
(11)

Calculations involving quadrupoles are greatly simplified by using the thin lens approximation, which in most cases is quite adequate. A quadrupole lens is thin if the principal planes practically coincide: i.e. $t_i = t_e = L/2$. If the expressions for t_i or t_e (10, 11) are expanded in powers of KL:

$$t_i = t_e = L(1 + \frac{K^2L^2}{12} + ...)$$

for a converging lens and,

$$t_i = t_e = L(1 - \frac{K^2L^2}{12} + ...)$$

for a diverging lens; and the thin lens approximation is satisfied when $K^2L^2 << 1$. Now expanding the focal lengths in power series gives:

$$\frac{1}{f_F} = \kappa^2 L(1 - \frac{\kappa^2 L^2}{6} + ...)$$

and $\frac{1}{f_D} = K^2 L (1 + \frac{K^2 L^2}{6} + ...)$

which in the thin lens approximation gives:

$$P_{F} = -P_{D} = K^{2}L$$

where P the power of the lens is the reciprocal of the focal length.

Quadrupoles are most frequently used in combinations of two (doublets) or three (triplets) to obtain systems which give overall focusing in both the x, z, planes. The focusing properties for doublets and triplets can be found in the literature (Luckey 1961, Enge 1959). The simplest procedure for focusing simultaneously in both planes,

employs a doublet consisting of two quadrupoles with approximately equal strength but opposite polarity. The beam envelope in a typical doublet is shown in Fig. 3.

2.4 Uniform Field Bending Magnet

The uniform field bending magnet (or simple wedge), serves three basic functions in a beam transport magnet system:

- i) a combination of bending magnets can deflect a beam through any required angle, or translate a beam by successive deflections in opposite directions.
- ii) The dispersive property of a bending magnet (the property of giving particles of different magnetic rigidity proportionately different deflections) provides a means of momentum (or energy) selection. Consequently bending magnets are frequently used as energy analysers.
- iii) A bending magnet can also be designed (by correct choice of entry and exit angles) to give a certain amount of focusing in the radial (horizontal) and, or the vertical planes.

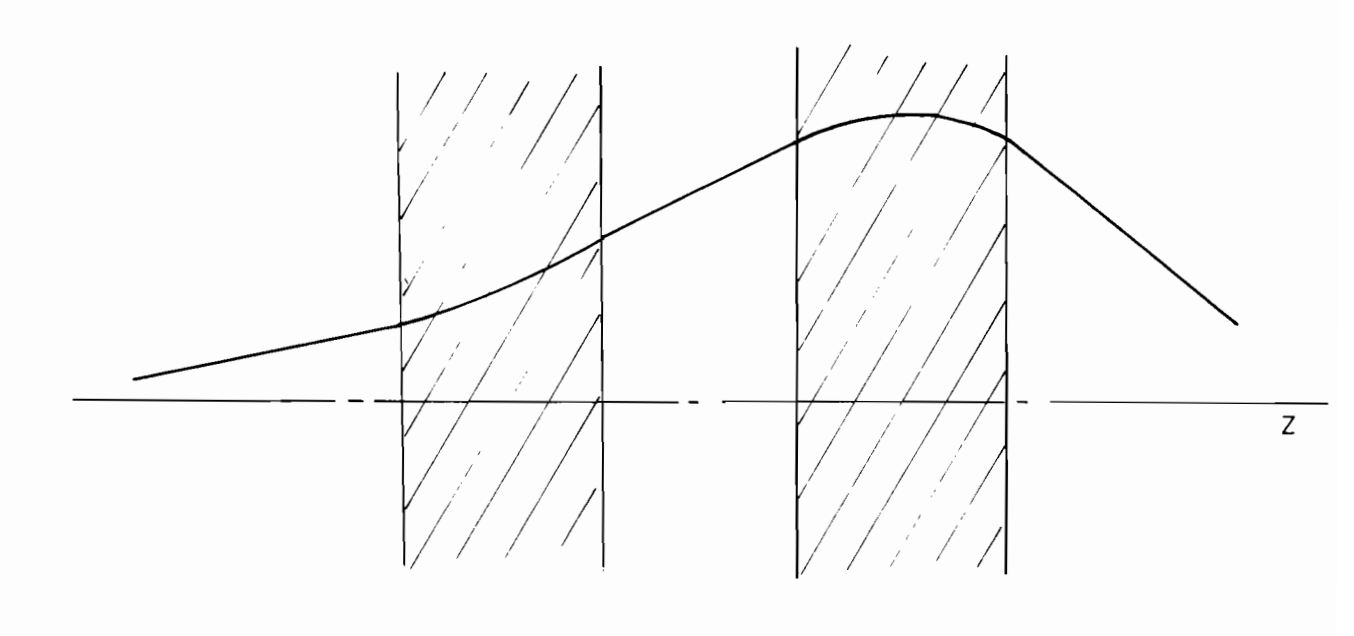
The geometry of a simple wedge magnet is shown in Fig. 4a. The central trajectory is deflected through an angle α in the radial plane and is undeflected in the vertical plane. The angles β_1 and β_2 are chosen, conventionally, to be positive in the direction which provides positive vertical focusing. This convention can be restated: β is positive if the beam trajectory is on the same side of the normal to the pole edge as the centre of curvature of the trajectory.

The radial orbits for a simple wedge with β_1 = β_2 = 0 will be considered first, then generalized to include the case of angled pole

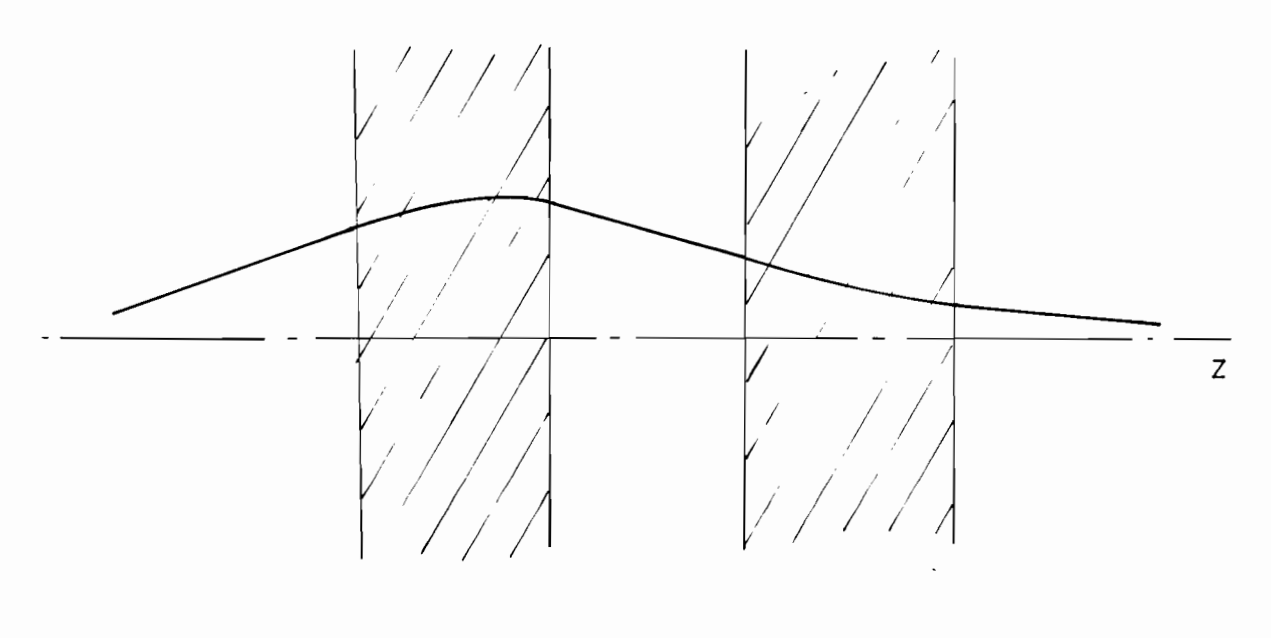
FIGURE 3:

BEAM ENVELOPE IN QUADRUPOLE DOUBLET

The quadrupole configuration illustrated here has the first quadrupole focusing in the y plane and the second in the x plane.



X PLANE



Y PLANE

FIG 3 - BEAM ENVELOPE IN QUADRUPOLE DOUBLET

edges; and followed by the vertical equations of motion.

Following the procedure of Penner (1961), the coordinates (x, x') will be calculated at the magnet exit for a particle which enters the magnet with coordinates (x_0, x_0') and momentum $p' = p + \Delta p$, for the case $\beta_1 = \beta_2 = 0$. The central trajectory $(x_0 = x_0' = 0, p = p)$ is a circular arc of radius ρ and length $\rho\alpha$, and the trajectory of the case considered is an arc of radius $\rho' = \rho + \Delta \rho$,

where
$$\Delta p = \Delta \rho \rho$$

This case is illustrated in Fig. 4b. AC is the central trajectory with centre of curvature at O. BD is the trajectory of the particle with momentum p' with centre of curvature at P. The initial and final coordinates are x_0 (=AB), x_0 ' and x (=CD), x'. Construct OQ perpendicular to OA, PQ parallel to OA, and RP perpendicular to OC. Then, since:

$$OA = OC = \rho$$

$$BP = DP = \rho + \Delta \rho$$

$$OC + CD = OR + RD$$

and RD = PDcosx'

it follows that:

$$x = OR + (\rho + \Delta \rho)\cos x^* - \rho$$

$$= OQ\sin \alpha + PQ\cos \alpha + (\rho + \Delta \rho)\cos x^* - \rho$$

$$= BP\sin x_0' \sin \alpha + (OB - BP\cos x_0')\cos \alpha + (\rho + \Delta \rho)\cos x^* - \rho$$

$$= (\rho + \Delta \rho)\sin x_0'\sin \alpha + \left[\rho + x_0 - (\rho + \Delta \rho)\cos x_0'\right]\cos \alpha$$

$$+ (\rho + \Delta \rho)\cos x^* - \rho$$

The first order solution in x is obtained by using the inequalities $x_0' << 1$, $x_0 << \rho$, $\Delta \rho << \rho$, x' << 1 and rejecting all terms which are second order or higher in x_0 , x_0' , x', $\Delta \rho$.

FIGURE 4:

- a) GEOMETRY OF A SIMPLE WEDGE MAGNET
- b) CONSTRUCTIONS FOR CALCULATING TRAJECTORIES IN A SIMPLE WEDGE MAGNET (NO VERTICAL FOCUSING) Refer to the text for a description of the symbols.

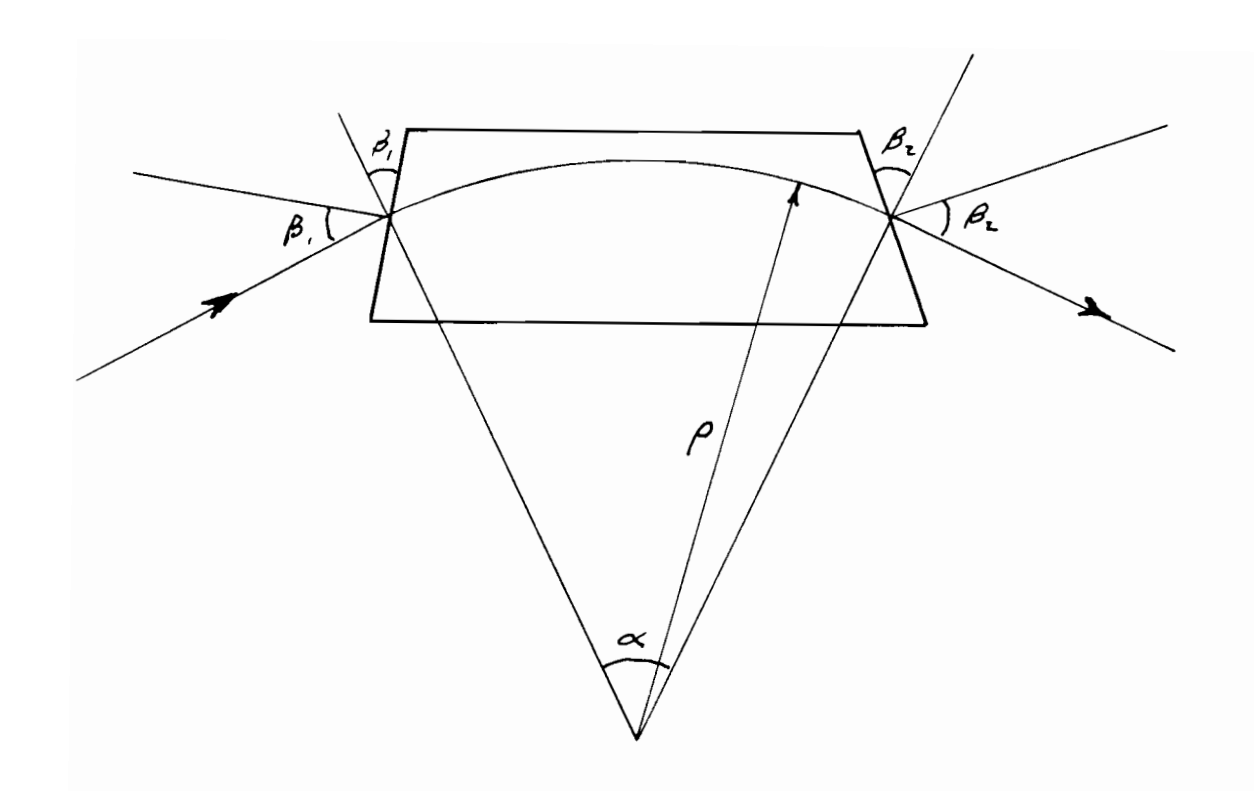


FIG 4a - GEOMETRY OF SIMPLE WEDGE MAGNET

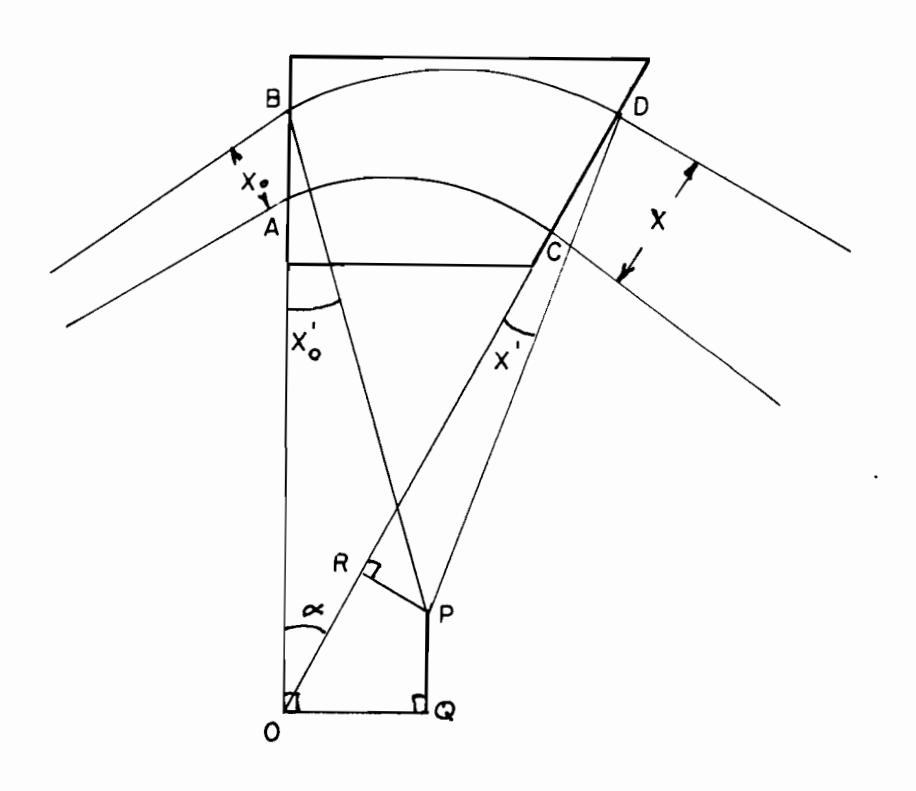


FIG 4b - CONSTRUCTIONS FOR CALCULATING
TRAJECTORIES IN A SIMPLE WEDGE MAGNET

•

To first order then:

$$x = x_0 \cos \alpha + x_0 \cdot \rho \sin \alpha + \Delta \rho (1 - \cos \alpha). \tag{12}$$

The coordinate x' may be obtained by using the relation $\tan x' = (1/\rho)(\frac{\partial x}{\partial \alpha})$, considering α to be a variable and evaluating the derivative of (12) at α :

$$x' = \frac{-x_0}{\rho} \sin\alpha + x_0' \cos\alpha + \frac{\Delta \rho}{\rho} \sin\alpha \tag{13}$$

Since to first order tanx' = x'.

In matrix form the radial equation of motion is:

It should be noted here that for the case $\Delta p = 0$ the above transfer matrix can be reduced to a two by two submatrix which on comparison with (8) indicates essentially the same transformation as for a converging quadrupole. Here α has replaced KL and ρ , 1/K. Thus in addition to deflection of a particle of momentum p the bending magnet also focuses horizontally with a focal length of $f = \rho/\sin\alpha$.

Consider now the effect of rotation of the pole edges on the radial trajectories. Fig. 5 illustrates the effect of rotation of the exit pole edge through an angle β_2 . OQ is the central trajectory and AB the pole edge with $\beta_2 = 0$. With $\beta_2 = 0$ the trajectory of a particle with initial coordinates $(x_0, x_0', \Delta p/p)$ is RV, which is an arc of radius $\rho + \Delta \rho$ between R and T with centre of curvature at C and a straight line from T to V. The final coordinates are $(x_1, x_1', \Delta p/p)$

where $x_1 = PT$ and $x_1' = angle ATC$ as shown above.

If the pole edge is now rotated through β_2 about the point P on the central trajectory to A'B' then the new trajectory for the particle $(x_0, x_0', \Delta p/p)$ is RW, which consists of an arc RS with centre at C and a straight line SW. The final coordinates of this trajectory are $(x, x', \Delta p/p)$ where $x = x_1 + TU$ and $x' = x_1' + angle TCS$. From Fig. 5 it can be seen that SU and ST are of the same order of magnitude as x_1 (provided β_2 is not much greater than 45^0). The angle TCS is therefore small (of order x/p) and TU is zero to first order. Also to first order SU = ST and the perpendicular distance of S to the edge AB is SUcosx' = SU. Thus:

$$SU = PTtan\beta_2 = x_1tan\beta_2 = xtan\beta_2$$

and the angle TCS = SU/(ρ + 4ρ) = (x/ ρ)tan β_2 .

The effect of an exit pole edge rotation can therefore be expressed by an additional transfer matrix as follows:

$$\begin{pmatrix} x \\ x' \end{pmatrix} = \begin{pmatrix} 1 & 0 \\ \tan \beta_2/\rho & 1 \end{pmatrix} \begin{pmatrix} x_1 \\ x_1' \end{pmatrix}$$

which essentially is the same as adding a thin lens to the normal exit wedge.

The effect of rotating the entrance pole edge through an angle β_l can be considered by a similar method using the mirror image of Fig. 5 and is given by the transfer matrix

$$\begin{bmatrix} 1 & 0 \\ \tan \beta_1/\rho & 1 \end{bmatrix}$$

The transfer matrix then for radial motion through a uniform field

FIGURE 5:

ROTATION OF EXIT POLE EDGE

The symbols are explained in the text.

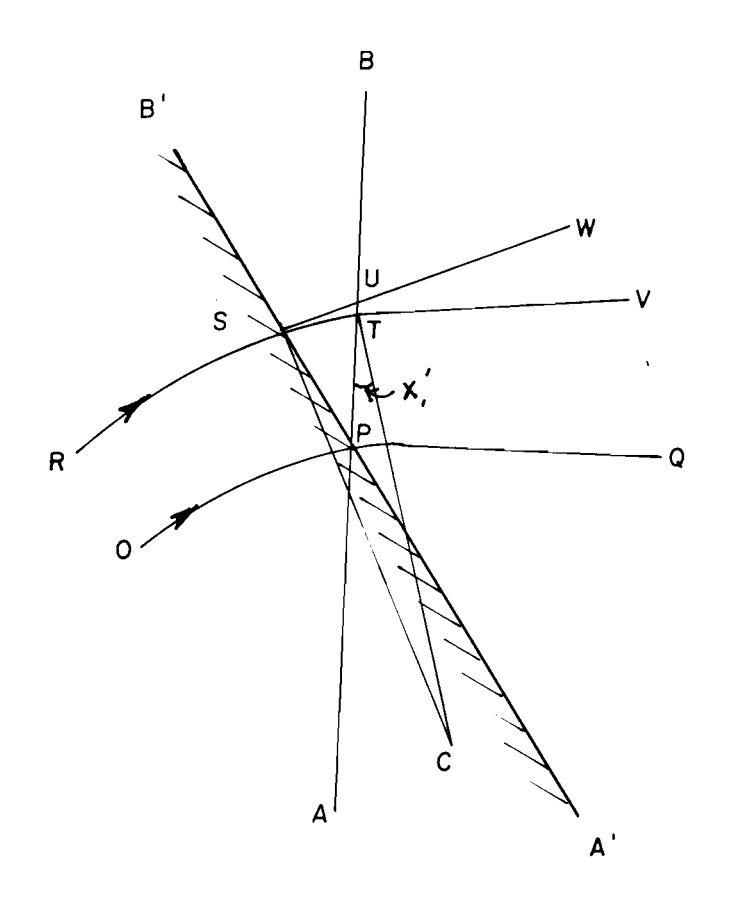


FIG 5 - ROTATION OF EXIT POLE EDGE

bending magnet with both pole edges rotated, is obtained by combining the above edge matrices (extended to three dimensions) with (14):

$$M(\alpha, \beta_1, \beta_2) = \begin{bmatrix} 1 & 0 & 0 \\ \tan \beta_2/\rho & 1 & 0 \\ 0 & 0 & 1 \end{bmatrix} \begin{bmatrix} \cos \alpha & \rho \sin \alpha & \rho (1-\cos \alpha) \\ -\sin \alpha/\rho & \cos \alpha & \sin \alpha \\ 0 & 0 & 1 \end{bmatrix} \begin{bmatrix} 1 & 0 & 0 \\ \tan \beta_1/\rho & 1 & 0 \\ 0 & 0 & 1 \end{bmatrix}$$

which gives:

$$M = \begin{bmatrix} \cos{(\alpha-\beta_1)} & \rho \sin{\alpha} & \rho(1-\cos{\alpha}) \\ \hline \frac{\cos{\beta_1}}{\cos{\beta_1}} & \cos{(\alpha-\beta_2)} & \sin{\alpha} + (1-\cos{\alpha})\tan{\beta_2} \\ \hline \frac{-(1-\tan{\beta_1}\tan{\beta_2})\sin{(\alpha-\beta_1-\beta_2)}}{\rho\cos{(\beta_1+\beta_2)}} & \cos{(\alpha-\beta_2)} & \sin{\alpha} + (1-\cos{\alpha})\tan{\beta_2} \\ \hline 0 & 0 & 1 \end{bmatrix}$$
(15)

It should be noted here that positive β_1 or β_2 (vertical focusing) implies defocusing in the horizontal plane.

A uniform field bending magnet with normal entrance and exit does not deflect trajectories in the vertical direction and can be represented by a drift space of length ρα for the vertical motion. If, however, the pole edges are rotated there are magnetic field components in the x direction of the horizontal plane near the pole edges (due to the fringing field). This is illustrated in Fig. 6 where a coordinate system including the normal to the pole edge z' has been superimposed on the coordinate system of the trajectory z.

In the fringing field region, from Maxwell's equations curl B = 0and: $\frac{\partial B}{\partial y'} = \frac{\partial B}{\partial z'}$

FIGURE 6:

NON - NORMAL ENTRY THROUGH THE FRINGING FIELD OF A WEDGE MAGNET

 \boldsymbol{z} represents the optic axis or particle trajectory, and \boldsymbol{z}^{\star} the normal to the entrance pole edge.

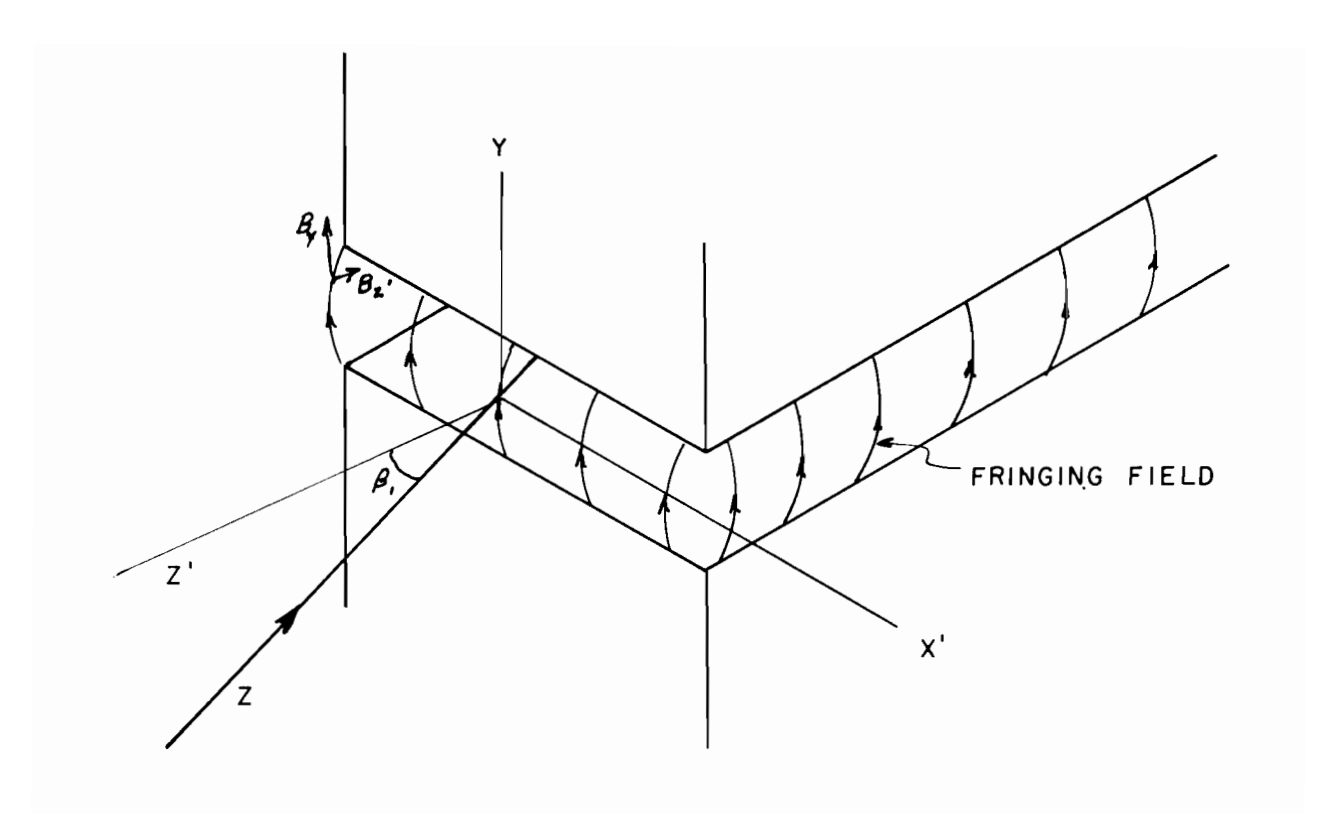


FIG 6 - NON-NORMAL ENTRY THROUGH THE FRINGING
FIELD OF A WEDGE MAGNET

or to first order:

$$dB_{z} = dB_{y} y'$$

It is also obvious that y' = y and z' = $z\cos\beta_l$.

Hence:
$$B_{x} = B_{z} \cdot \sin \beta_{1} = \sin \beta_{1} \frac{dB_{y}}{dz} y$$

$$= \tan \beta_{1} \frac{dB_{y}}{dz} y$$

From the Lorentz force:

$$\mathbf{F}_{\mathbf{v}} = \mathbf{q} \mathbf{v} \mathbf{B}_{\mathbf{X}}$$

The change in momentum in the y direction is then derived as follows:

$$\Delta p_y = -F_y dt = -F_y \frac{dz}{v} = -qv B_x \frac{dz}{v}$$

(the negative sign being introduced since $p_{\boldsymbol{y}}$ is decreasing i.e. vertically focusing)

$$\frac{\Delta p_y}{p} = \Delta y' = \frac{-q}{p} \tan \beta_1 dB_y y$$

and integrating:

$$y' = \frac{-q}{p} \tan \beta_1 yB$$

$$= \frac{-B \tan \beta_1 y}{B \rho} = -(\frac{1}{\rho} \tan \beta_1) y$$

The only first order effect therefore is to cause an angular deflection of the trajectories in the vertical direction. A similar expression can be obtained for the exit pole edge deflection, and the transformation matrix for the whole magnet in the vertical plane is then given by:

$$\begin{bmatrix} \mathbf{y} \\ \mathbf{y} \end{bmatrix} = \begin{bmatrix} 1 & 0 \\ -\tan\beta_2/\rho & 1 \end{bmatrix} \begin{bmatrix} 1 & \rho\alpha \\ 0 & 1 \end{bmatrix} \begin{bmatrix} 1 & 0 \\ -\tan\beta_1/\rho & 1 \end{bmatrix} \begin{bmatrix} \mathbf{y}_0 \\ \mathbf{y}_0 \end{bmatrix}$$

which gives the vertical transfer matrix:

$$M = \begin{bmatrix} 1 - \alpha \tan \beta_1 & \rho \alpha \\ -\frac{1}{\rho} (\tan \beta_1 + \tan \beta_2) + \frac{\alpha}{\rho} \tan \beta_1 \tan \beta_2 & 1 - \alpha \tan \beta_2 \end{bmatrix}$$
(16)

2.5 Fringing Fields in Quadrupoles and Bending Magnets.

In the previous sections, the fields in quadrupoles and wedge magnets have been treated as if they had sharp boundaries. In fact there are fringing fields which extend out for distances of the order of several gap widths for uniform bending magnets and of the order of a fraction of the aperture for a quadrupole. The theoretical fringe field for plane-parallel square poles has been calculated by Coggeshall (1947) and more generally for deflecting magnets by Enge (1964). In order to make the "sharp cut-off" theory compatible with "non-ideal" magnets having fringe fields, the conventional modification is to introduce the concept of the "effective length" of the field. In the case of a uniform field magnet, the effective length is simply defined as:

$$L_{eff} = \int Bdz /B_{max}$$

where B_{max} is the maximum field inside the magnet, and the integral is taken along the optic axis to include the fringing field areas. The fringing field for a bending magnet can be approximated in the region near the gap by $B = B_{max}e^{-z/a}$ (Coggeshall, 1947) where a is the gap width and z the distance from the pole edge.

With quadrupoles the correction is somewhat more difficult to define. In the fringing field, the field gradient is still mainly constant at fixed z, although it decreases with distance from the magnet edge approximately as $e^{-z/2a}$ (Luckey 1961) where 2a is the

quadrupole aperture. A fairly good, although somewhat tedious, approximation to the quadrupole behaviour can be obtained by dividing the fringe region into small sections, each with a transfer matrix characterized by the gradient k at the centre of the section, multiplying the matrices together, and so defining an equivalent or effective length and gradient for the quadrupole.

In practice the effective lengths for both bending magnets and quadrupoles are found empirically. For uniform field bending magnets use is made of:

$$\alpha = (B\rho)^{-1} \int Bdz = \frac{B_{\text{max}} \cdot L_{\text{eff}}}{B\rho}$$

where α is the angle of deflection of particles of rigidity Bp. The effective length usually exceeds the physical length of the iron pole face by about two gap widths. The correction to the quadrupole length depends on several parameters, in particular the overhang of the coils, and is usually of the order of ten to thirty percent of the quadrupole aperture.

2.6 Use of Transfer Matrices in Tracing Particle Trajectories

It has been shown above that the transformation properties of the various magnetic devices of a beam transport system on a beam of charged particles can be represented by a set of transfer matrices. A magnet system consists of an arrangement of bending magnets and quadrupoles separated by drift spaces. The problem then of tracing out the trajectory of a particle with a given set of initial conditions $(x_0, x_0', \Delta p/p)$ reduces to the simple multiplication of matrices. By convention, three by three matrices are used in the horizontal plane

to include dispersion effects (note that quadrupoles are non-dispersive to first order, and the matrices of (8) can be readily expanded to three dimensions). In almost all cases it is sufficient to use two dimensional matrices in the vertical plane since dispersion is not encountered to first order.

It should be remembered however, that the matrix formulation is only an approximation, albeit a good one in most cases, and depends for its accuracy on the criteria of first order theory being satisfied.

The matrix method of tracing particle trajectories, although elegant and simple, only follows one particle at a time. Consequently many trajectories have to be traced in order to determine the overall behaviour of a beam, and unless done with the help of a computer this can prove very tedious. A more practical method of theoretical prediction or verification of the performance of a beam transport system uses the concept of the phase space ellipse in tracing the beam envelope through the system.

2.7 The Phase Space Ellipse.

The spread of a beam of mono-energetic particles can be represented by an ellipse in phase space. The individual particles comprising the beam are plotted as points on a plot of the displacement from the optic axis against the angular spread in the horizontal or vertical phase plane. The points are then found to lie within an area bounded by a closed curve, which for most beams has a generally elliptical shape. In linear systems the phase space area is a constant and is a characteristic of the beam known as its "emittance". The concept of the "density of particles in phase space" comes from statistical mechanics, and the

preservation of the area in phase space in a linear system is a direct consequence of Liouville's theorem (Tolman 1950). Liouville's theorem states that volumes in phase space are conserved if the particle motion can be derived from a Hamiltonian (i.e. if the energy remains constant). The phase space for a particle beam is in fact six dimensional, but since there is no appreciable coupling between the motion in the three planes, two dimensional phase space plots can be used. Another very useful consequence of Liouville's theorem is that any transformation matrix describing the motion of particles in a linear system has a determinant of unity (Penner 1961). This provides a very convenient method for detecting errors, or checking calculations involving transfer matrix calculations.

The behaviour of phase space diagrams can be qualitatively explained as follows for simple linear transformations. The effect of a drift space is illustrated in Fig. 7a: particles with positive divergence x' and negative displacement will drift towards the optic axis, whereas particles with positive displacement will drift even further from the optic axis. The net effect is that the ellipse shown in Fig. 7a will drift to the ellipse of 7c. An ellipse in the second and fourth quadrants then represents a converging beam, and in the first and third a diverging beam. As the beam passes through a crossover or focus (7b), the ellipse has its axes parallel with the x', x axes, and for a beam with finite area in phase space, size or displacement at the focus will not be a point but rather have finite size. The quality of a beam is therefore largely determined by its area in phase space. Zero phase area implies that a beam can be

FIGURE 7:

PHASE SPACE ELLIPSES

The behaviour of a phase space ellipse in the ${\bf x}$ plane is illustrated for a drift space and a thin lens.

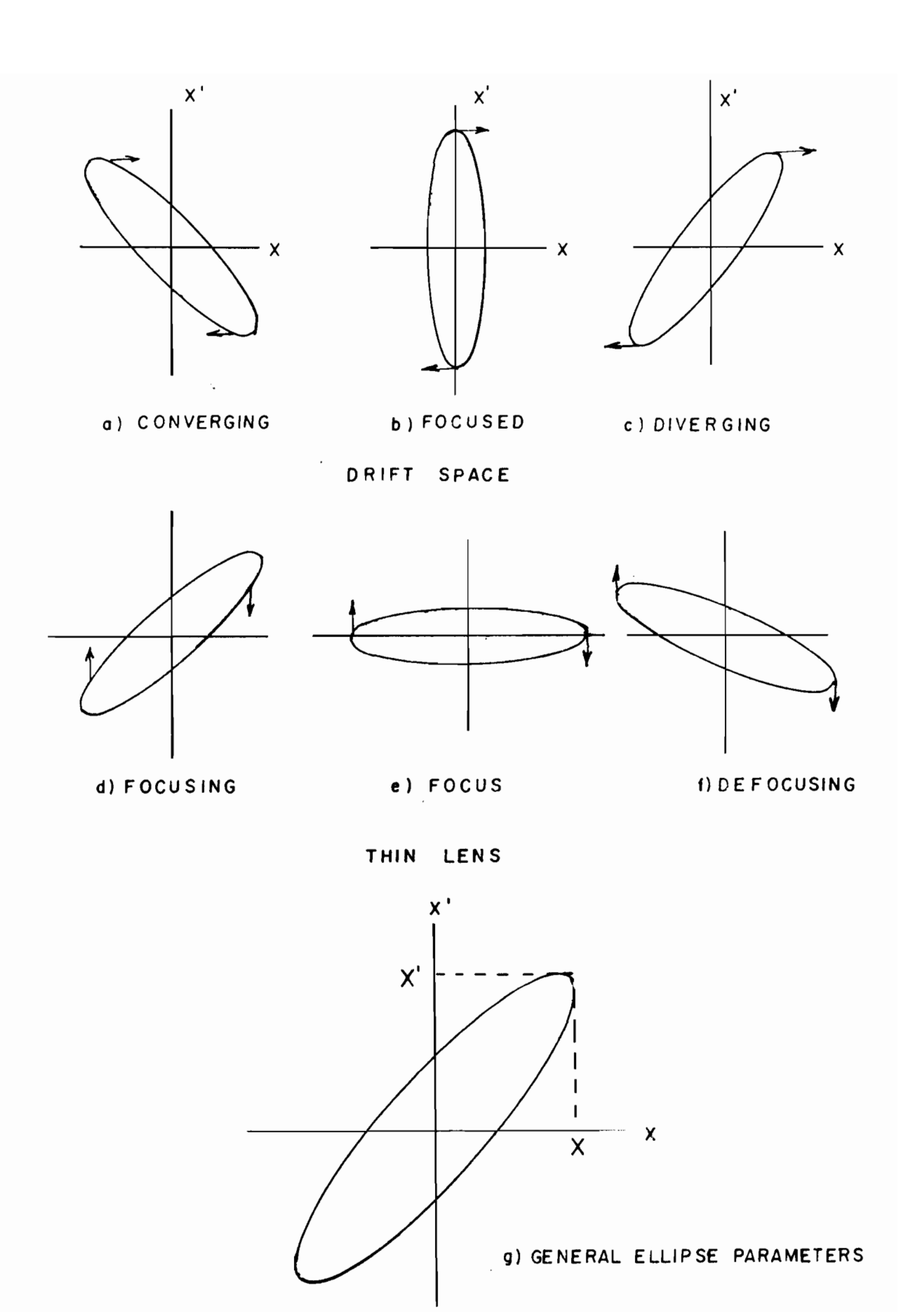


FIG 7 - PHASE SPACE ELLIPSES

focused to a point or cast an infinite distance remaining parallel.

The case of a simple focusing thin lens is illustrated in Figs. 7d,e,f.

In transporting a phase space ellipse through a beam transport system, a useful parameterization of the ellipse is given by:

$$x = \chi \cos(\theta + \Psi_X)$$
; $x' = \chi \sin(\theta - \Psi_X)$

$$y = Y\cos(\theta + \Psi_y); \quad y^* = Y^*\sin(\theta - \Psi_y)$$

where X, X' and Y, Y' are the maximum displacement and divergence in the x and y planes as illustrated in Fig. 7g, ψ_x , ψ_y characterize the slope of the major axis of the ellipse (ψ is negative for a diverging and positive for a converging beam), and θ is a running parameter. The three parameters X, X', ψ_x , or Y, Y', ψ_y then characterize any particular ellipse. Consider a transfer matrix which takes a point x_0 , x_0 ' into x, x':

$$\begin{pmatrix} x \\ x' \end{pmatrix} = \begin{pmatrix} a & b \\ c & d \end{pmatrix} \begin{pmatrix} x_0 \\ x_0' \end{pmatrix}$$

The effect of this transformation on a phase space ellipse can be shown to give:

$$x^2 = a^2 x_0^2 + b^2 (x_0)^2 - 2x_0 x_0 \sin 2 \psi_{x_0}$$
 ab

$$(x^{\bullet})^2 = c^2 x_0^2 + d^2 (x_0^{\bullet})^2 - 2x_0 x_0^{\bullet} \sin^2 \psi_{x_0} cd$$

$$XX^*\sin^2 \Psi_X = X_0X_0^*\sin^2 \Psi_{X_0} (ad + bc) - X_0^2ac - (X_0^*)^2bd$$

and Area = $\pi X_0 X_0$ 'cos2 Ψ_X with similar equations for the y plane. Hence, knowing any specified initial ellipse, these equations can be used to find the behaviour of the ellipse (by giving the parameters X_1, X_1, Ψ_X , Y_1, Y_1, Ψ_Y) at any point in a transport system.

3. THE EXTERNAL BEAM TRANSPORT SYSTEM

3.1 General Requirements

The beam transport system was designed to fulfil several basic requirements:

- a) To bend the external proton beam from the cyclotron through an angle of some 75° into the direction of the new Beam Hall.
 - b) To provide some means for varying the energy of the beam.
- c) To collect and deliver this beam to any experimental location at the end of the Beam Hall.
- d) To provide sufficient flexibility in focusing the beam on to a target in the experimental area.

Part of the required deflection was achieved by modifying the existing 45° C-frame bending magnet and the additional bend was obtained by the design of a new 28° H-frame bending magnet. In order to achieve energy variation by the normal method of energy degrading, and at the same time minimize the increase in phase space area of the beam due to multiple scattering in the degrader, the added requirement of an intermediate focus at which to place the degrader had to be incorporated in the design. This was achieved by designing the entrance and exit pole edge angles of the two bending magnets to give strong overall focusing in both the horizontal and vertical planes. Collection and refocusing of the degraded beam was accomplished with a quadrupole doublet which was designed to cast a converging beam into the Beam Hall. A switch magnet was used to deflect the beam horizontally across the Beam Hall and a second pair of quadrupoles mounted on a carriage pivoted about the centre of the switch magnet provided the final focusing

at the experimental area.

The final layout of the external beam transport system is shown in Fig. 8, and as a general reference for the following sections

Table I summarizes the coordinate z of the various elements comprising the system. Fig. 9 presents these in a graphical form showing, in addition, the horizontal and vertical apertures. The origin of the optic axis of the system was arbitrarily chosen as the aluminum exit flange of the cyclotron. It should be noted that all distances and lengths shown in these diagrams are actual physical dimensions and correction to the effective lengths should be made for any transport calculations (effective lengths are tabulated in tables 2, 3). The following sections give a more detailed account of the installation and performance of the transport system.

3.2 Section to the Entrance of the 28° Bending Magnet

a) Alignment: The beam enters the transport system through a pair of horizontal and vertical slits at the exit of the cyclotron and is transported to the bending magnet system in 4" o.d. copper vacuum pipe. The beam pipe was aligned on the beam by exposing Polaroid Land Film Packets (Polapan 200, type 52) at several points along the optic axis and carefully surveying the beam path. This in fact was the procedure followed in the alignment of almost all sections of the beam transport system and some representative examples of the beam patterns obtained are shown in Plates 1 and 2. The convention used in all polaroid exposures followed a left handed coordinate system with y - displacement up, x-displacement to the right and displacement along the optic axis into the plane of the picture.

FIGURE 8:

LAYOUT OF THE BEAM SYSTEM

EARTH FILL

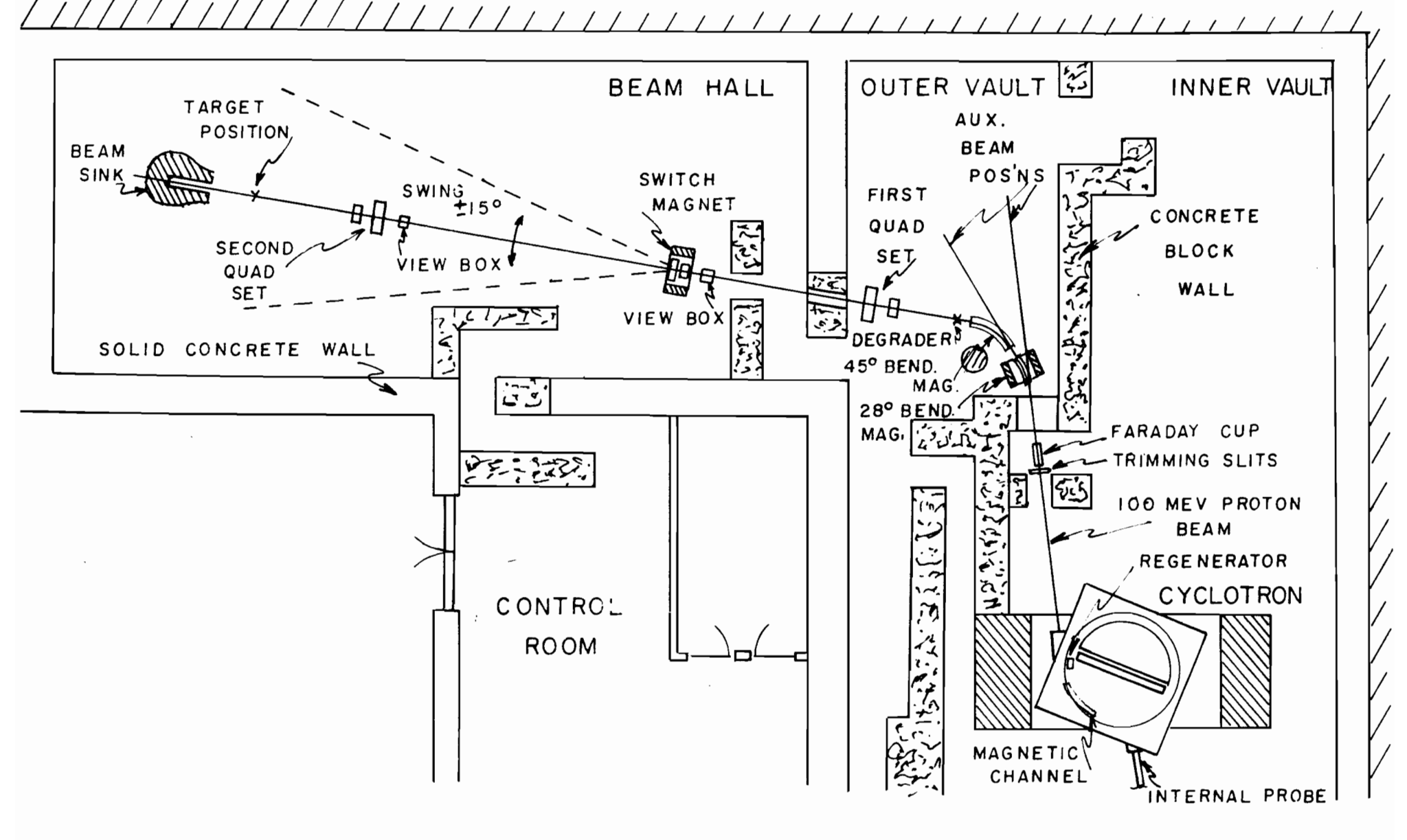


FIG 8 - LAYOUT OF BEAM SYSTEM

TABLE 1

Coordinate z of the elements comprising the system measured from the aluminum flange at the cyclotron exit.

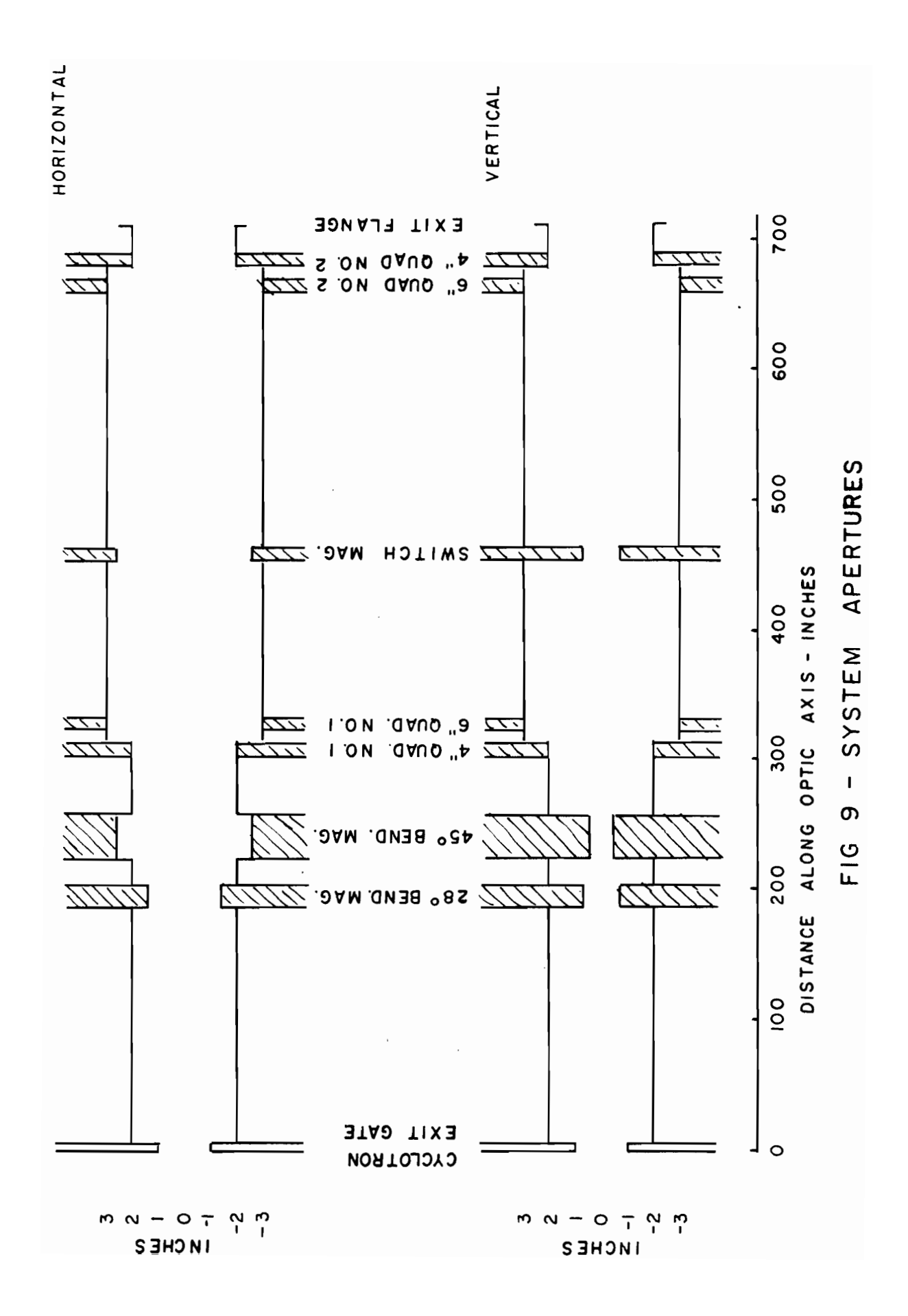
	z in inches
Horizontal exit Slit	-5.0
Vertical exit Slit	-2.5
Thin Collimator	131.4
Trimming Slits	132.7
28° Bending Magnet Entry	186.1
Exit	204.1
Straight through exit	218.8
45° Bending Magnet Entry	225.1
Exit	258.6
Straight through exit	254.6
4" Quadrupole No. 1 Centre	306.9
6" Quadrupole No. 1 Centre	327.5
View Box No. 1 Centre	437.1
Switch Magnet Entry	453.8
Exit	465.9
View Box No. 2 Centre	646.8
6" Quadrupole No. 2 Centre	665. 8
4" Quadrupole No. 2 Centre	685.7
End of final "T" flange	712.8

All distances are physical dimensions and correction to effective lengths should be made for transport calculations.

FIGURE 9:

SYSTEM APERTURES

Here the vertical and horizontal defining apertures of the main elements of the system are shown with their coordinate z.



The simplicity and speed of this method make it ideal for the purpose. The exposure used is typically of the order of 10^9 protons, depending of course on the cross-sectional area of the beam.

- b) Improvement to Beam Extraction. The external beam intensity, as originally reported by Moore (1962), was 4 x 10⁻⁹ amps. or approximately 2.5 x 10¹⁰ protons/sec. It was found that an increase in regenerator strength of 10 % gave an increased beam intensity of 2.5 x 10⁻⁸ amps or 1.6 x 10¹¹ protons/sec, after optimizing the regenerator position and magnet current. The variation of beam intensity with regenerator position (at optimum magnet current setting) is shown in Fig. 10 for three regenerator strengths. Exposures taken before and after the change of regenerator strength at z=98" are shown in Plate 1, pictures (1) and (2) respectively. On the basis of these exposures, the strength of the internal horizontal-focusing quadrupole section in the extraction channel was decreased to minimize the horizontal divergence of the extracted beam. The pattern of the final extracted beam is shown in Plate 2, (1),(2), (3).
- c) Emittance of the Beam. Phase space diagrams of the new external beam were obtained by placing a brass block with a rectangular array of 0.030" diameter holes spaced 0.125" horizontally and 0.090" vertically in the beam and tracing the rays to a polaroid exposure some 50" downstream. The diagrams are shown in Fig. 11. The beam

At the time of writing, the beam intensity is 8×10^{-9} amps. This loss in intensity is associated with a reduction of about 50% in the cyclotron internal beam and is probably due to poor r.f. oscillator performance.

FIGURE 10:

BEAM INTENSITY VARIATION WITH REGENERATOR STRENGTH

Each point represents optimum magnet current. The reading of the regenerator position on the micrometer barrel increases for radial motion into the cyclotron.

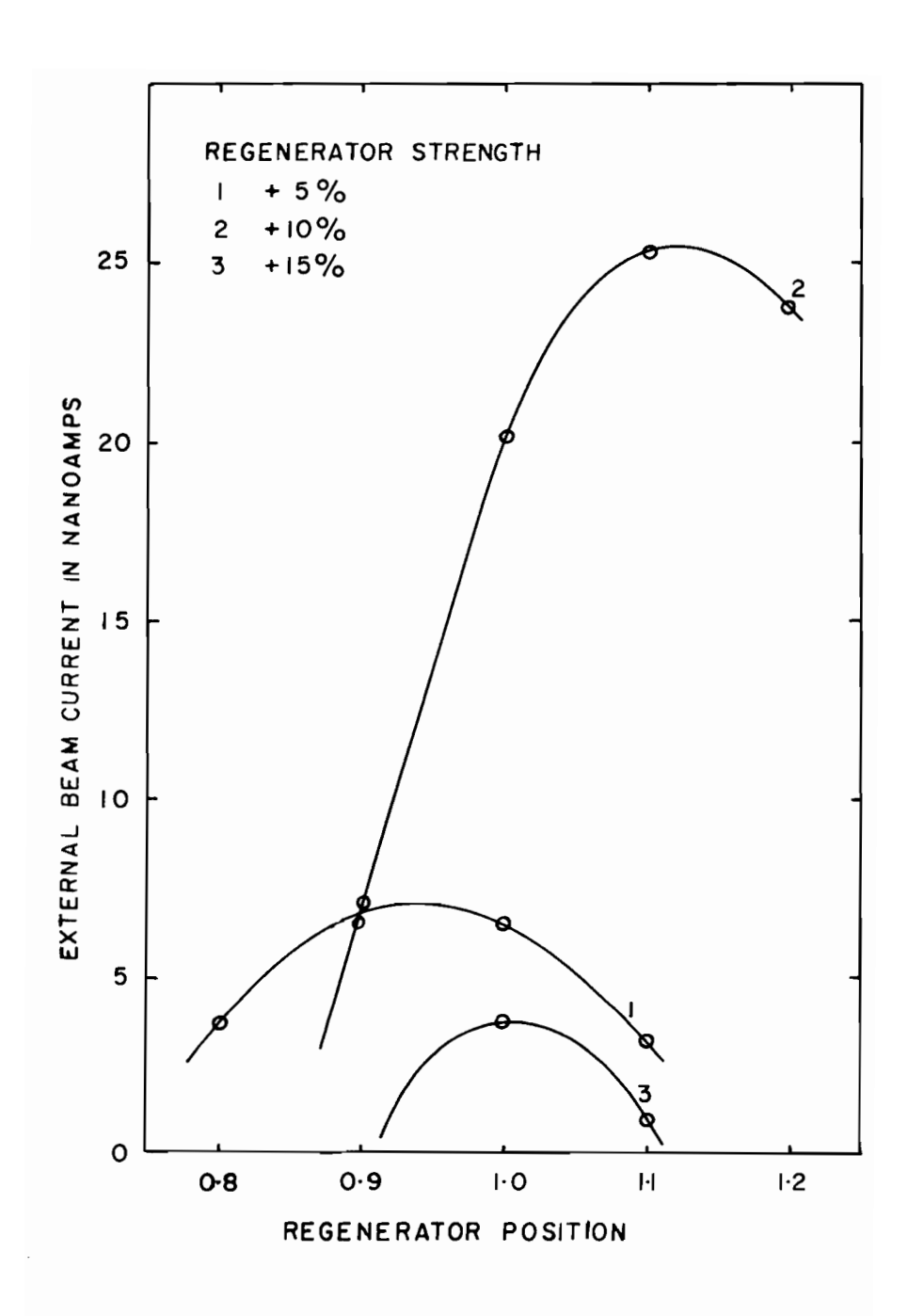


FIG IO - BEAM INTENSITY VARIATION WITH REGENERATOR STRENGTH

has an area of 0.675 inch milliradians in the horizontal phase plane and 1.69 inch milliradians in the vertical plane.

- d) Trimming Slits. A set of horizontal and vertical slits were designed and constructed with a view to trimming the beam to ensure perfect transmission through the system. These slits are located at z = 133" and are geared so that each slit can be adjusted separately or in pairs. The slits can also be moved remotely by use of a "selsyn" servo-motor.
- e) Faraday Cup. In order to provide a quick measurement of the external beam current, a Faraday Cup with a swinging bottom was installed in the section before the entrance to the 28° magnet. A sketch of the Cup is shown in Fig. 12.

The Faraday Cup is an accurate and absolute method of measuring the current of a charged particle beam. However precautions must be taken to ensure that inaccuracies due to systematic errors do not arise. The most common sources of error are due to:

- i) ionization of residual gas in the cup by the proton beam
- ii) knock-on electrons from the cup window
- iii) secondary emission of electrons from the cup due to the incident protons
- iv) aperture of cup too small to accept the entire proton beam The first two errors can be effectively removed by coupling the cup directly to the external beam vacuum system (10⁻² microns). The third error is commonly minimized by placing a magnetic field of a few hundred gauss across a fairly deep cup (length commonly twice the diameter) or a bias Fing" or grid at a negative voltage of a few hundred volts in front of the cup.

PLATE 1:

BEAM PICTURES

These pictures were obtained by exposing Polaroid Land Packets (Polapan 200, type 52) directly in the beam. The convention used in all polaroid exposures follows a left handed coordinate system with y displacement up, x displacement to the right and displacement along the optic axis (the beam direction) into the plane of the picture.

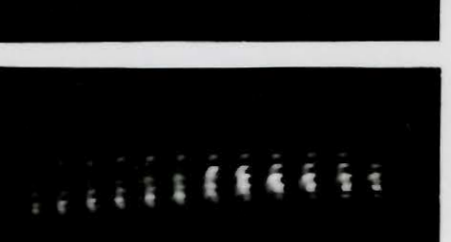
ORIGINAL EXTRACTED BEAMS

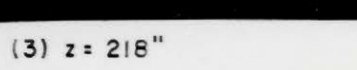


(2) z= 98"

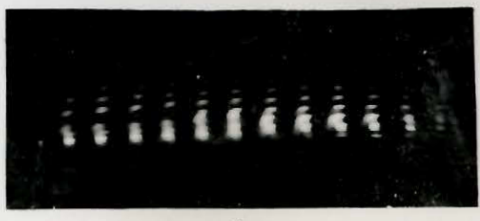
EFFECT OF WEDGES ON 28° BENDING MAGNET











(4) z = 218"

FOCUS AFTER THIN (ΔΕ)
COLLIMATOR



(5) z = 271"

FINAL FOCUSED BEAM SPOT



(6) z: 761"

PLATE I - BEAM PICTURES

PLATE 2:

BEAM PICTURES AT POINTS THROUGH THE TRANSPORT DEFLECTION SYSTEM.

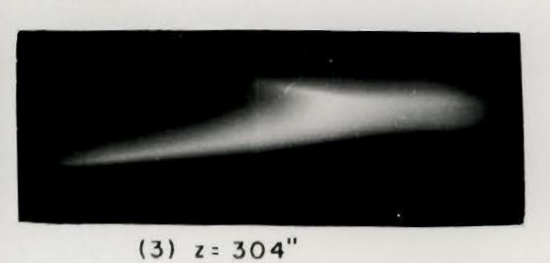
DRIFTING BEAM FROM CYCLOTRON



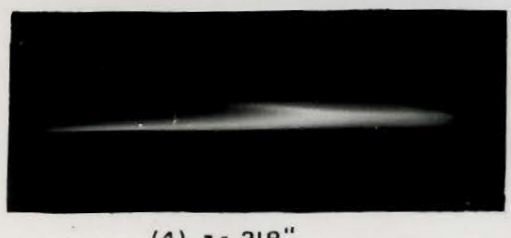
(1) z = 10"



(2) z = 178"



BEAM DEFLECTED BY 28° BENDING MAGNET



(4) z = 218"



(5) z = 255"

BEAM DEFLECTED 73° - BOTH BENDING MAGNETS



(6) z=262"



(7) z= 267"



(8) z= 271"



(9) z = 274"



(10) z = 283"

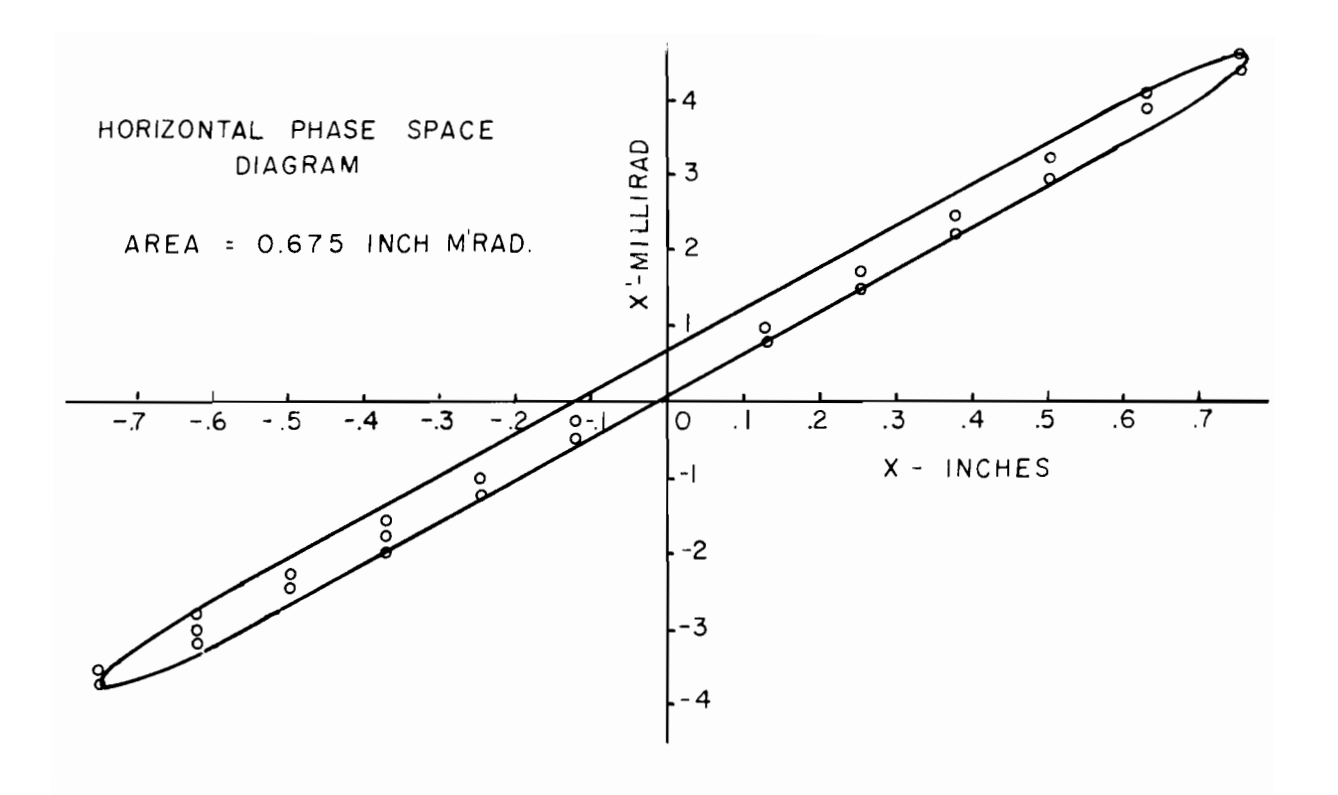


(II) z = 303"

PLATE 2 - BEAM PICTURES AT POINTS THROUGH TRANSPORT DEFLECTION SYSTEM

FIGURE 11:

EMITTANCE PLOTS AT z = 160"



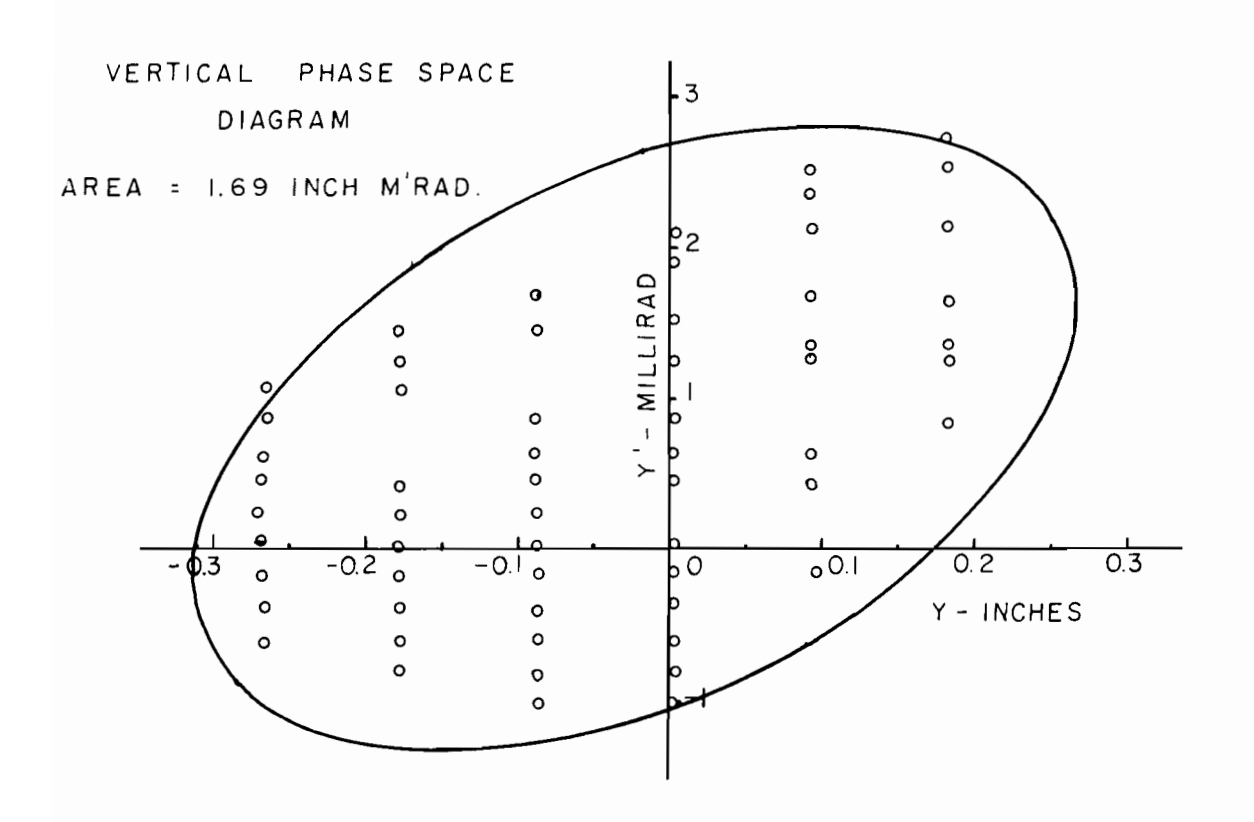


FIG II - EMITTANCE PLOTS AT Z = 160"

The end of the cup rotates on a teflon insulated shaft, and can be moved into the proton beam remotely from the cyclotron control desk. The shaft is rotated by a pair of solenoids, operating on a rack and pinion and controlled from the cyclotron control desk. The current from the Faraday Cup is measured with a Keithly micro-micro ammeter (model 414). The cup is located immediately after the trimming slits, where the cyclotron fringing field combined with the 8" length of the cup appears to be sufficient in the suppression of secondary emission electron losses. It was found that a bias voltage, on the bias ring (both positive and negative), had no noticeable effect on the current measured by the cup.

f) Intensity Profile of Beam. Intensity profiles of the beam were obtained at the trimming slit position by sweeping a 2 mm slit across the beam in both horizontal and vertical planes, and measuring the intensity of the beam through the slit with the Faraday Cup. The profiles obtained are shown in Fig. 13.

3.3 Deflection Into Beam Hall.

The beam pipe from the cyclotron passes through a window in the inner cyclotron vault shielding wall and is coupled to the $28^{\rm O}$ Bending Magnet vacuum chamber with a short section of flexible bellows. The vacuum chamber of the $28^{\rm O}$ Bending Magnet is directly coupled through another short section of bellows to the $45^{\rm O}$ Magnet chamber.

a) 28° Bending Magnet. The 28° H-frame bending magnet was designed in this Laboratory and the iron fabricated by Dominion Engineering. The coils were wound in the Laboratory using 6" wide by 0.012" thick pure (1S) Alcan aluminum strip, and insulating with

FIGURE 12:

FARADAY CUP EXTERNAL BEAM MONITOR

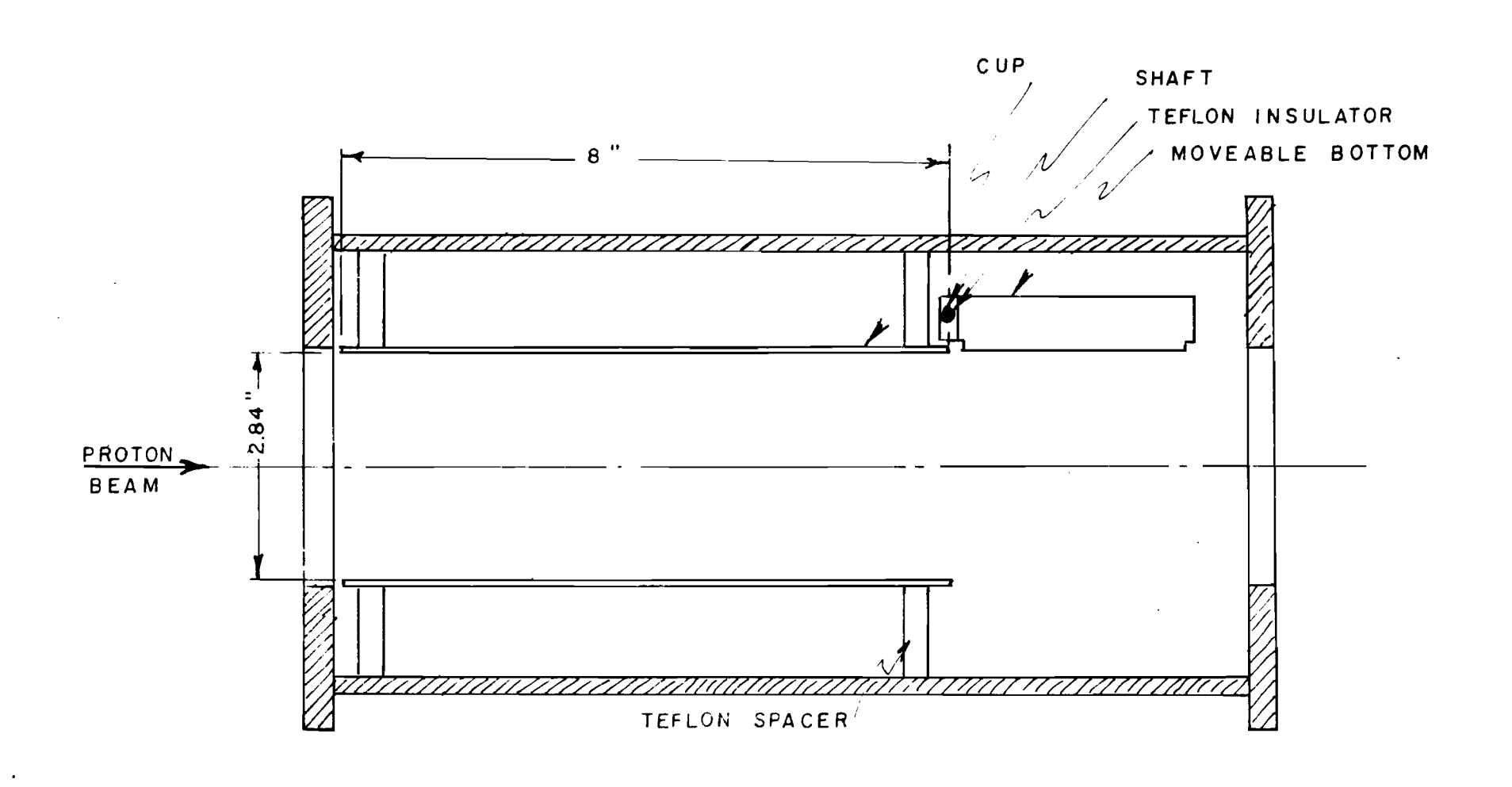


FIG 12 - FARADAY CUP FOR EXTERNAL BEAM MONITORING

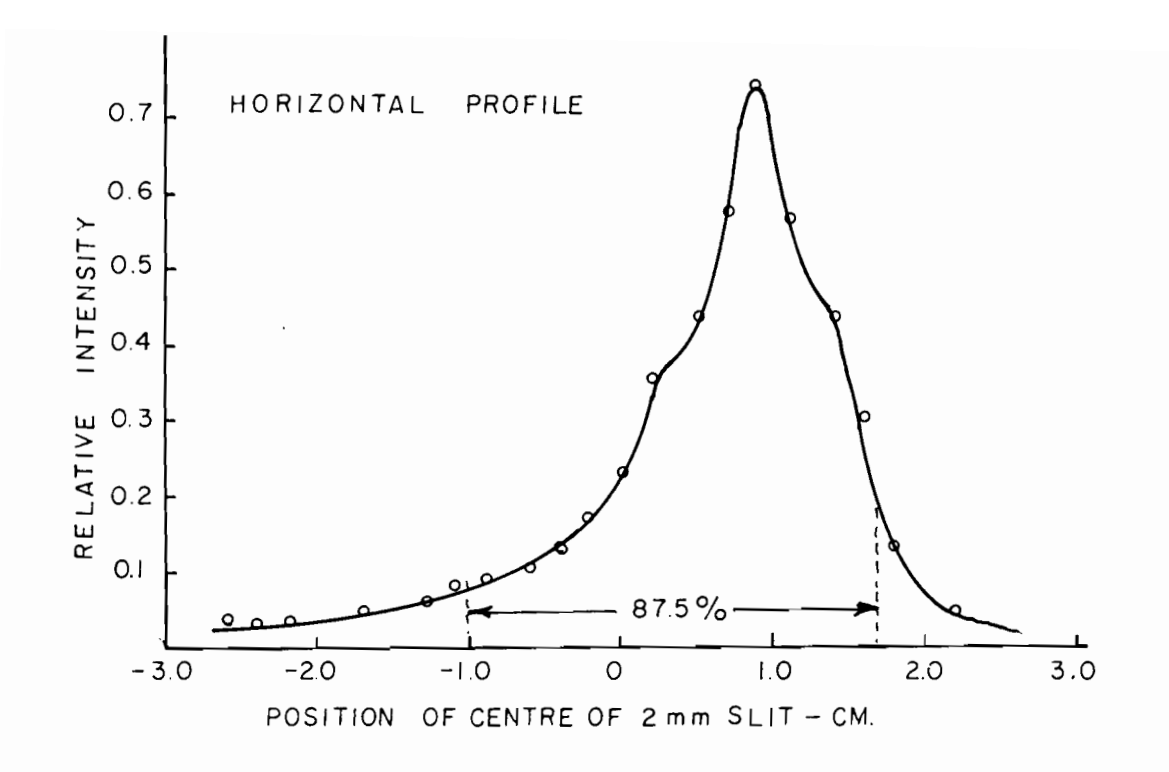
Edge cooling of the coils was achieved with copper plates. pole tips were designed to provide strong vertical focusing at the entrance and horizontal focusing at the exit. (The main limitation to transmission through the magnets being the small vertical aperture of the 45° Magnet). The tapered pole pieces are $4 \frac{1}{2}$ " wide and the general shape of the pole can be seen in Fig. 8. To provide a more uniform field over a greater area of the poles, adjustable edge shims of 3/8" wide x 1/8" iron were mounted on the pole edges and their position adjusted empirically by carefully mapping the field with a Hall probe (Moore 1962). The method of mounting the shims can be seen in Fig. 14. The vacuum chamber is made from copper waveguide and has an aperture 2.84" wide by 1.34" high. It is provided with a straight through section which helped in aligning the magnet and allows a target area to be set up along the line of the undeflected beam. The initial alignment of the 28° Magnet was performed by optically aligning the straight through section of the vacuum chamber on the previously surveyed beam path with a theodolite. Final alignment was accomplished with the proton beam, both using polaroid exposures and viewing a fluorescent screen with closed circuit television. alignment of the beam in the vacuum chamber was checked by bombarding a plexiglass block placed in the vacuum and observation of the beam pattern produced by discolouration of the plexiglass.

Pictures of the beam exiting from the cyclotron are shown in plate 2 (1,2,3). Non-linearities due to saturation in the sharp corners of the pole tips were observed, using the ray tracing technique described earlier (3.2c). This non-linearity was effectively removed

FIGURE 13:

BEAM INTENSITY PROFILES AT TRIMMING SLITS (z = 133")

The beam outside the indicated 87.5% in the horizontal plot does not get through the $28^{\rm O}$ Bending Magnet due to insufficient horizontal aperture.



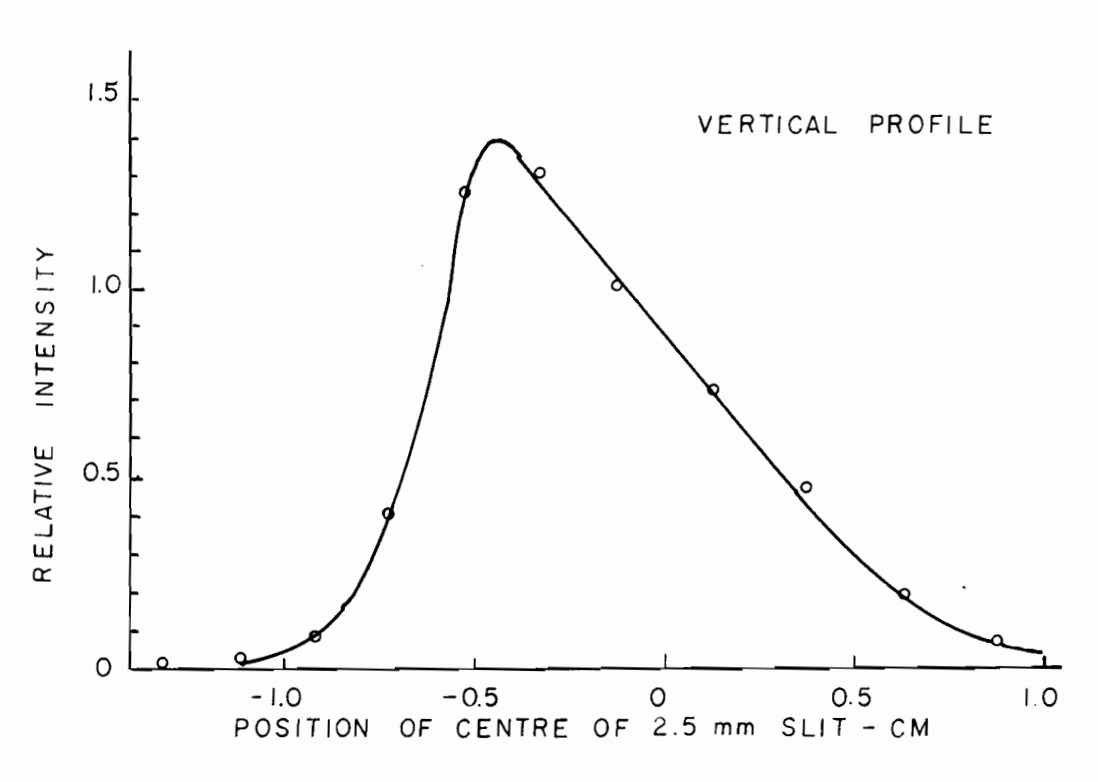


FIG 13 - BEAM INTENSITY PPOFILES AT TRIMMING SLITS (Z = 133")

FIGURE 14:

SHIMMING OF 280 BENDING MAGNET

The iron edge shims were used to provide a more uniform field across a wider portion of the pole pieces and the wedge shims were empirically adjusted to remove non-linearities.

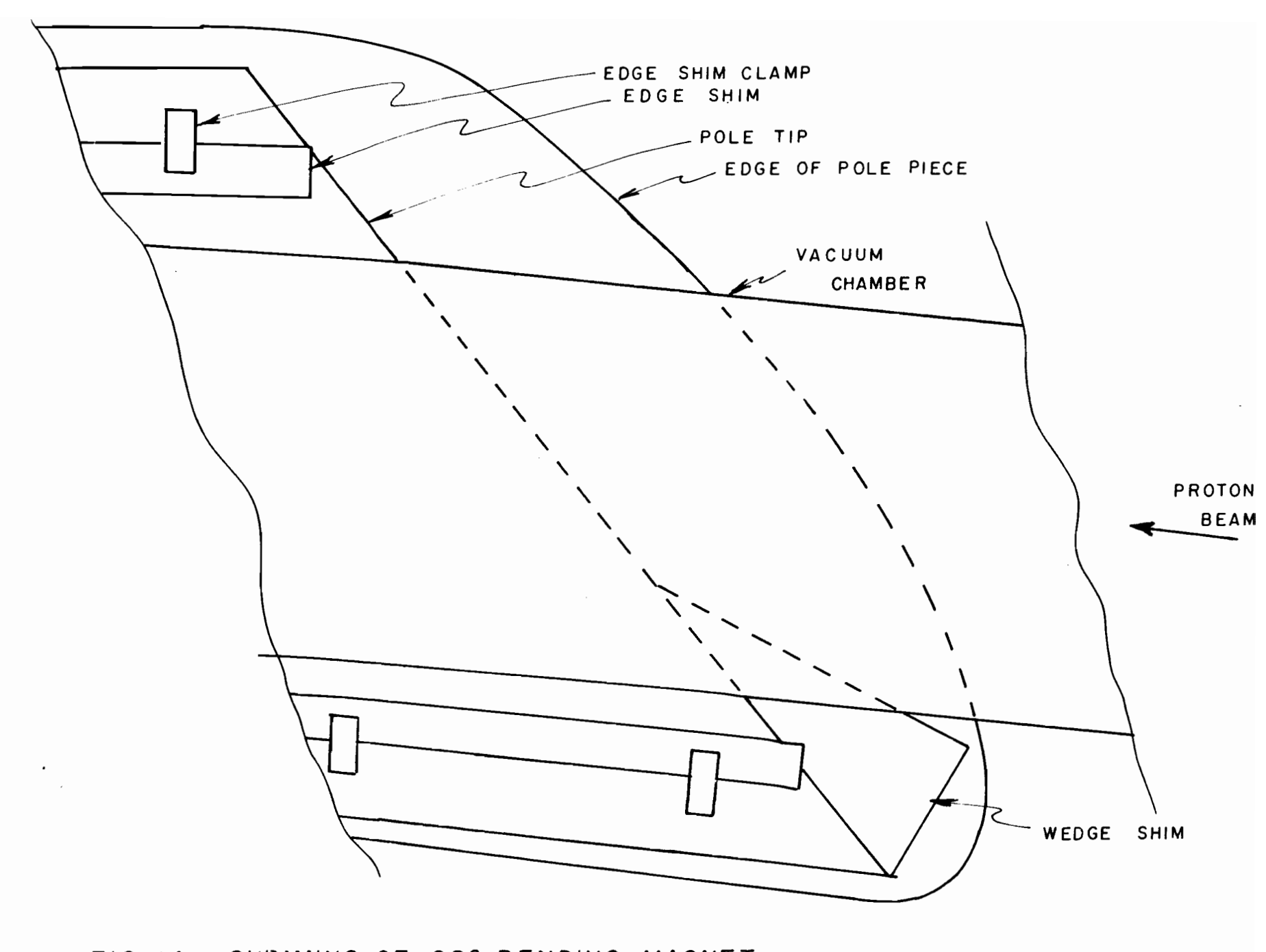


FIG 14 - SHIMMING OF 28° BENDING MAGNET

by cutting 15° from the exit angle of the poles and empirically wedge shimming the entrance pole tip as illustrated in Fig. 14. The effect of wedge shimming on the non-linearities can be seen in pictures (3) and (4) of Plate 1. In (3) and (4), both the entire beam and the array of "pencil" beams are shown, clearly demonstrating the improvement in (4) with wedge shims. The 28° Magnet was provided with a tilting adjustment screw with which the whole magnet could be rotated slightly on an axis parallel to the straight through optic axis, thus permitting the beam to be cast up or down by a few degrees in the vertical plane. This adjustment was carefully aligned to ensure a truly horizontal beam after deflection. The beam exiting from the cyclotron dips about four milliradians, and the beam now entering the beam hall dips by less than 0.2 milliradians. Pictures (4) and (5) of Plate 2 illustrate the strong vertical focusing and somewhat weaker horizontal focusing obtained with the 28° Bending Magnet.

b) The 45° Bending Magnet. This is a uniform field C-frame bending magnet and has been described in some detail by Hunt(1955). Slight modifications were made to the magnet including: a new vacuum chamber with a straight through section, a narrower pole gap to allow a higher field and new entrance and exit angles designed to give horizontal focusing. The aperture of the vacuum chamber is 5" wide by 0.94" high. No shimming of the poles was necessary, the field being uniform over a large area. The 45° Magnet was aligned following the same procedure as for the 28° Magnet with special care being placed in the vertical alignment.

The focusing effect of the two bending magnets on the proton beam is well illustrated by the pictures (6) to (11) of Plate 2.

c) Beryllium Degrader. A Beryllium degrader has been designed and is presently being constructed. When completed it will be placed at a location immediately following the $45^{\rm O}$ Magnet close to the horizontal focus. The degrader will be remotely controlled at the cyclotron console and will provide a large range of proton energies.

3.4 Transport into Beam Hall.

a) First Quadrupole Set: The beam from the focus at the exit to the 45° Magnet is strongly diverging (the minimum total divergence with no degrader is about 64 milliradians). This beam is collected, refocused and cast into the new Beam Hall by a pair of quadrupoles, consisting of one 4" aperture quadrupole manufactured by Spectromagnetics Industries, followed by a 6" aperture quadrupole manufactured by Pacific Electric Motor. The 4" quadrupole is normally used vertically focusing, and the consequent defocusing in the horizontal plane necessitated the larger aperture quadrupole for horizontal focusing.

The optimal position of this quadrupole pair is governed by two main considerations: the admittance of the quadrupole set after degrading which decreases with the solid angle subtended by the 4" quadrupole at the degrader, as the quadrupoles are moved further downstream. The focal length of the quadrupole doublet is shortest with the quadrupoles near to the degrader, and the magnification consequently undesirably large. A compromise between acceptable quadrupole admittance and magnification therefore had to be made.

The quadrupole set was aligned on the beam first optically using the carefully surveyed beam path and finally with the proton beam.

The alignment of the quadrupole magnetic centres on the beam path was

obtained by moving the quadrupoles until the centroid of the beam spot on a fluorescent screen viewed by closed circuit television appeared to be undeflected for different settings of the quadrupoles. To facilitate the focusing of the quadrupole doublet, viewing boxes were placed at two positions after the quadrupoles (at z=437" and z=647") permitting quick visual adjustment to suit experimental conditions. The fluorescent screen in each viewing box is remotely controlled and swings into the beam at an angle of 45° . The screens are viewed through plexiglass windows by television cameras.

b) Switch Magnet. The switch magnet is located some 12 feet from the first quadrupole set and provides a means of deflecting the proton beam to any point at the end of the Beam Hall. The magnet is a uniform field H-frame bending magnet, designed in this laboratory and constructed in the same way as the 28° Bending Magnet. The pole gap is 1 5/8" and the entrance and exit edges of the poles are perpendicular to the undeflected central beam trajectory. The pole gap was enlarged at the centre of the magnet to allow room for a flexible 6" diameter stainless steel bellows section in the vacuum chamber. This design permitted a continuously variable direction of the exit of the vacuum chamber over an angle of + 150, without breaking the vacuum in the system. The aperture of the vacuum chamber is 5.5" wide by 1.375" high and focusing of the first quadrupole set was adjusted to clear this aperture. The sections of vacuum pipe from the quadrupole set to the switch magnet and after the switch magnet are 6" o.d. aluminum. Alignment of the switch magnet followed the same procedure as the previous magnets.

- c) Second Quadrupole Set. The second quadrupole set consists of a 6" quadrupole and a 4" quadrupole identical to those of the first The first quadrupole focuses vertically (normal polarities) and the 4" quadrupole horizontally to give the desired focus at a target. At full strength, spot sizes of the order of 10^{-2} square inches can be obtained. An example of the focused beam is shown in picture (6) of plate 1. The two quadrupoles were mounted on a carriage which pivoted about the centre of the switch magnet, making transport of the beam to any direction at the end of the beam hall a very simple procedure. quadrupole carriage also supports the vacuum pumping system, interlocks and controls for the external beam system. This quadrupole set was aligned in the same way as the first quadrupole set. However alignment was obtained at the undeflected position of the switch magnet, and consequently irregularities in the level of the floor (up to 1/16") will give rise at some positions to slight deflections of the beam centroid by the quadrupoles.
- d) Beam Sink. The beam sink consists of epoxy in a copper cylinder which forms a Faraday Cup to collect the transmitted beam current. This Faraday Cup has a depth of 28" and an aperture of 6". Epoxy is used to stop the proton beam because carbon produces fewer neutrons than most materials and produces no long lived radio activity. The Faraday Cup is enclosed in a structure of two tons of iron blocks to attenuate the neutron and gamma ray fluxes produced by the collected beam.

3.5 Magnet Power Supplies.

The magnet power supplies were designed and built in the laboratory and descriptions of the various supplies appear in internal Laboratory

reports. All the magnets are protected by water cooling interlocks. Regulation on the bending magnets has been observed by continuous monitoring of the voltage on the series regulator shunt, to be of the order of several parts in 10^4 over fairly long periods. The voltage was monitored by balancing most of the potential across a Rubicon type B potentiometer in series with a 10 mv Leeds and Northrup recorder. The quadrupole supplies are also regulated to a few parts in 10^4 .

3.6 Summary of Magnet Properties.

The properties and general parameters of the bending magnets are tabulated in table 2 and those of the quadrupoles in table 3. Table 2 includes a general purpose experimental 20° C-frame bending magnet which was designed and constructed the same way as the 28° Bending Magnet and Switch Magnet. The excitation curves for the 28° and 45° bending magnets are shown in Fig. 15. These were obtained by measuring the field in a uniform region of the magnets with a Hall Probe.

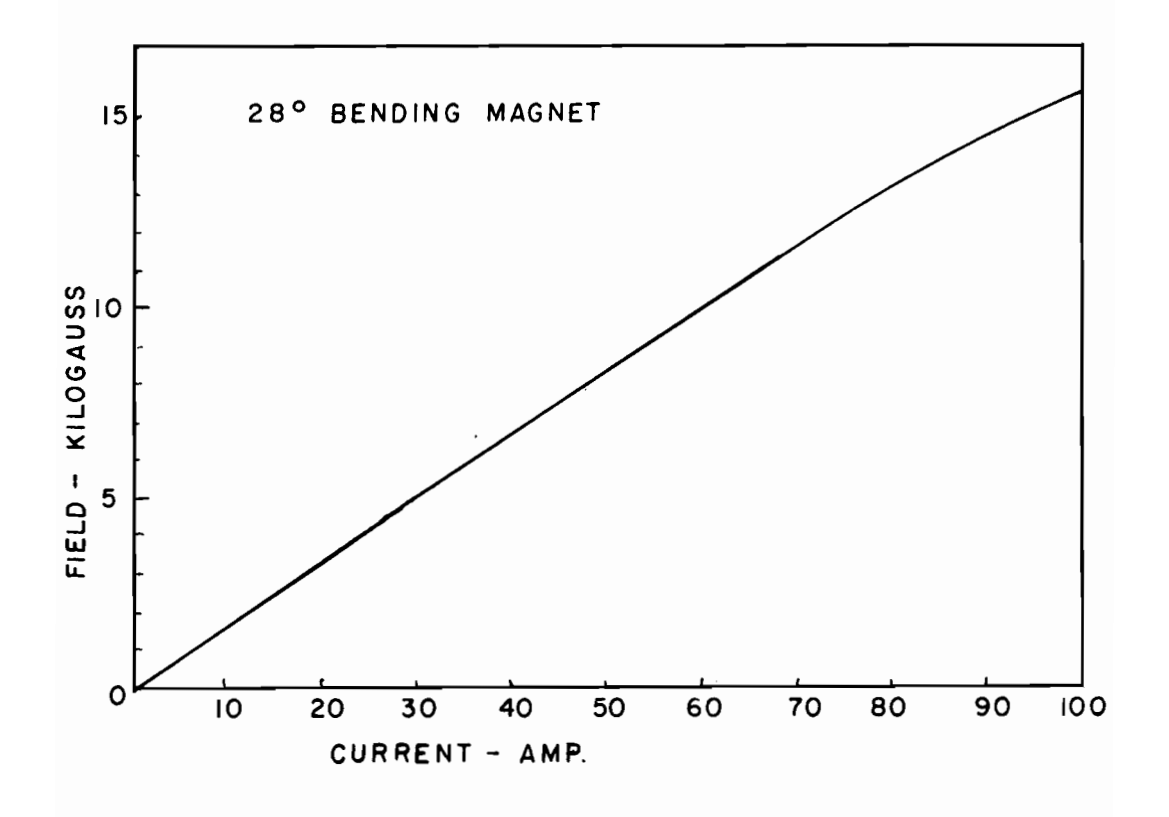
3.7 Performance of the Beam Transport System

a) Deflection System. Using the methods of Chapter 2 and the experimentally obtained beam emittance of Fig. 11, as a set of initial conditions, several properties of the deflection system were calculated theoretically, and are compared below with experimental results. Transfer matrices were calculated for the two bending magnets and the drift spaces involved and are tabulated in table 4. The beam envelope was then obtained by transporting the phase space ellipses of Fig. 11 through the system and the resulting profiles are shown in Fig. 16.

FIGURE 15:

EXCITATION CURVES

The excitation curves for the two bending magnets were obtained by measuring the field in a uniform region with a Hall probe.



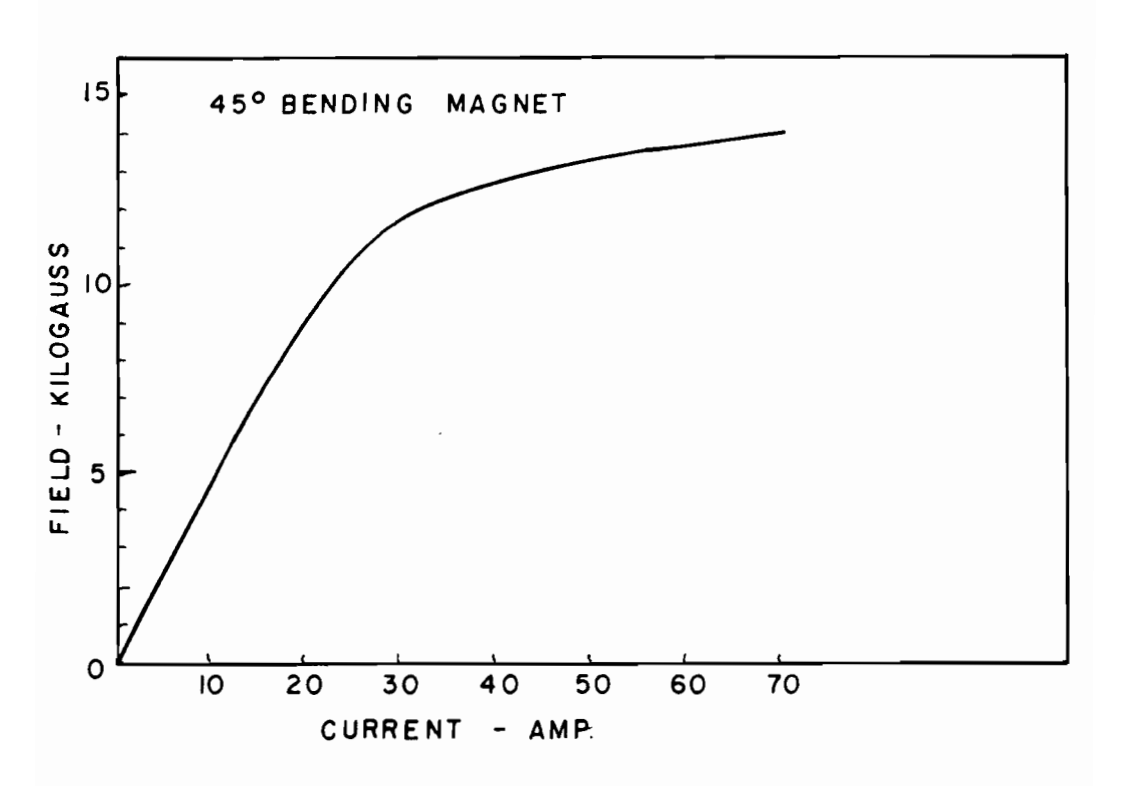


FIG 15 - EXCITATION CURVES

TABLE 2
Bending Magnet parameters

Magnet	Defl.	Pol	e edg	e angl	e s	Curvature	Lei	ngth	Apert	ure	Curre	ent
	Angle	Ste	eel	Effec	tive	ρ	Steel	Effective	Horiz.	Vert.	Max	Usual
	α	β_1	β_2	β_1	β_2	Inches	Iı	nches	Inc	hes	An	nps
28°	28°	45 ⁰	-25°	45 ⁰	-27 ⁰	42.9	18.0	21.0	2.84	1.34	100	86
45 ⁰	45.5°	-38°	U	-31°	_2°	43.6	33.5	34.6	5	0.94	65	52
Switch	to +15°	U	t o 15	0	to 150	Var.	12.1	13.7	5.5	1.37	100	Var.
Experimen	Pol	e tip	s to si	uit				5		150	Var.	
		exp	erime	nt								

TABLE 3

Quadrupole Parameters

Quadrupole Aperture		Aperture	Length	Turns	Field Gradient	Lens Power	Maximum	
			Steel Effective	per	per amp.	per amp.	Current	
		Inches	Inches	Pole	Weber/ m^3	Rad/m	amps	
4	inch	4	8 9.4	58	0.0434	9.46 x 10 ⁻³	300	
6	inch	6	10 12.6	100	0.0566	9.20 x 10 ⁻³	400	

Also shown in these graphs are the experimental values for the maximum sizes (2x, 2y) in the horizontal and vertical planes, obtained from the polaroid exposures of plate 2. The agreement is generally very good, in spite of the fact that no account was taken of the cyclotron fringing field, the transformation from the cyclotron exit to the 28° Magnet entrance being taken as a drift space. The behaviour of the horizontal phase ellipse is illustrated in Fig. 16a where the ellipse is plotted for several points through the system. The horizontal phase ellipse at $z = 160^{\circ}$ was projected backwards (using an inverse drift space transfer matrix) towards the cyclotron and the crossover point found to be at $z = -21.2^{\circ}$. The distance to the horizontal focus after the bending magnets can then be found from the matrix equation:

$$\begin{pmatrix} \mathbf{x} \\ \mathbf{x'} \\ \frac{\Delta p}{p} \end{pmatrix} = \begin{pmatrix} 1 & \ell & 0 \\ 0 & 1 & 0 \\ 0 & 0 & 1 \end{pmatrix} \mathbf{M}_{4} \mathbf{M}_{3} \mathbf{M}_{2} \mathbf{M}_{1} \begin{pmatrix} \mathbf{x}_{0} \\ \mathbf{x}_{0} \\ \frac{\Delta p}{p} \end{pmatrix} = \begin{pmatrix} \mathbf{a} & \mathbf{b} & \mathbf{e} \\ \mathbf{c} & \mathbf{d} & \mathbf{f} \\ 0 & 0 & 1 \end{pmatrix} \begin{pmatrix} \mathbf{x}_{0} \\ \mathbf{x}_{0} \\ \frac{\Delta p}{p} \end{pmatrix}$$

where ℓ is the drift space to the focus from the 45° Magnet exit, and M_1 , M_2 , M_3 , M_4 , are the horizontal transfer matrices for: the drift space from the crossover inside the cyclotron to the 28° Magnet entrance, the 28° Bending Magnet, the drift space separating the magnets and the 45° Magnet respectively. The condition for focusing, then, (at the central momentum p) is simply that the matrix element b of the product matrix be zero (since by definition x must be independent of x_0). This gives a focus distance $\ell = 7.2^{\circ}$ ($z = 267^{\circ}$) which compares very well with the experimental value of $\sim 9^{\circ}$ ($z = 269^{\circ}$). This is also shown in Fig. 16. Another property of interest is the momentum dispersion of the combined

TABLE 4

Transfer Matrices for Deflection System

	Horizontal					Vertical				
	а	b	c	d	e	f	а	b	c	d
28° Bending Magnet	1.352	20.15	00643	0.644	0.0502	0.00409	0.512	21.0	0174	1.249
45° Bending Magnet	0.273	31.0	0263	676	0.130	0.00703	1.477	34.6	0.0150	1.028
Drift Spaces:										
Cyclotron exit to 28° Entry	1	184.6	o	1	O	o	1	184.6	0	1
28° Exit to 45° Entry	1	19.5	υ	1	O	o	1	19.5	0	1
Drift Spaces: Cyclotron exit to $28^{\rm O}$ Entry	1	184.6	O	1	o	o	1	184.6	o	

Units are: x,y - inches

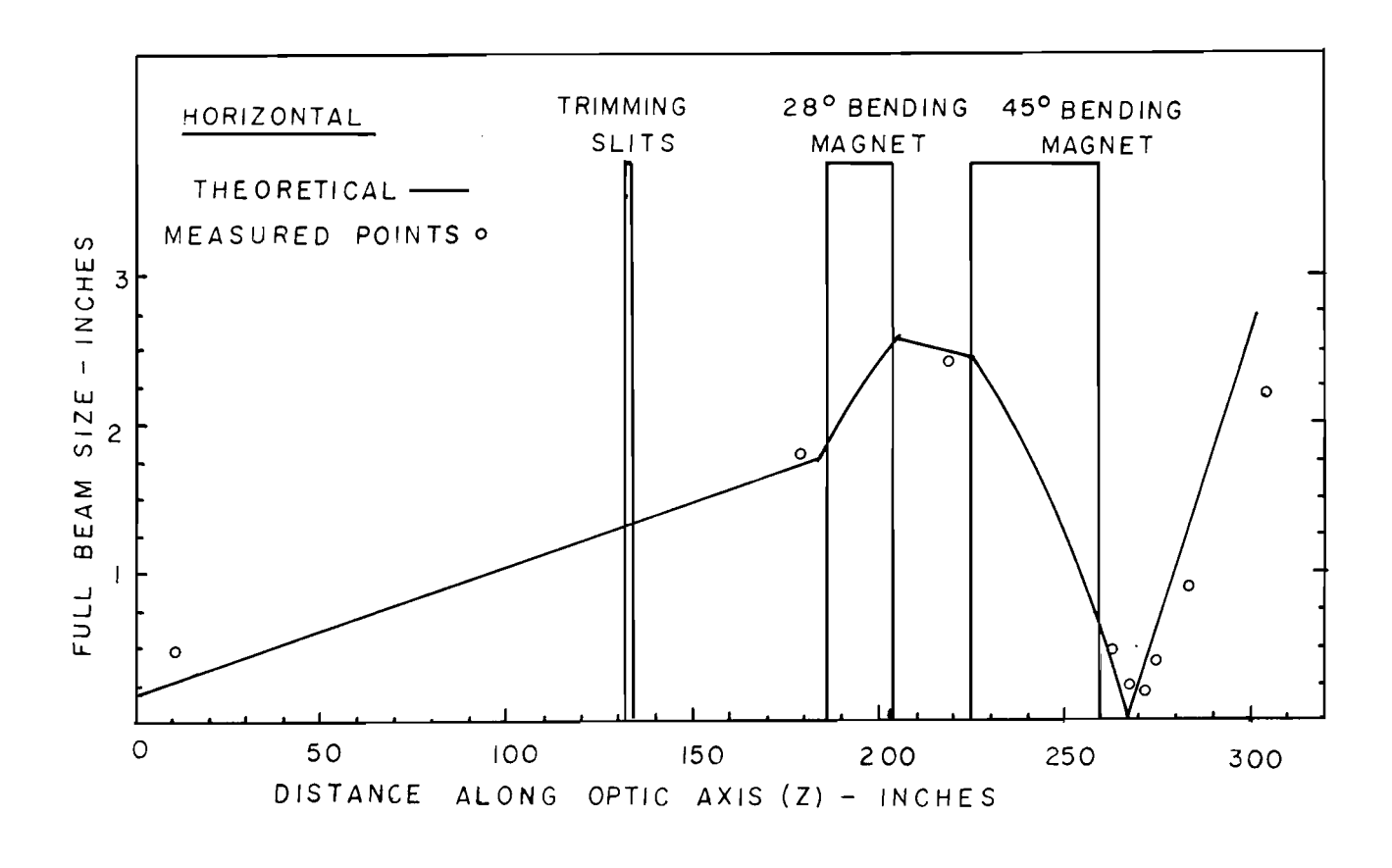
x',y' - milliradians

△p/p - percent

FIGURE 16:

BEAM ENVELOPE THROUGH DEFLECTION SYSTEM

The beam envelope obtained theoretically from the emittance plots of Fig. 11 is compared with points determined from sizes of polaroid exposures.



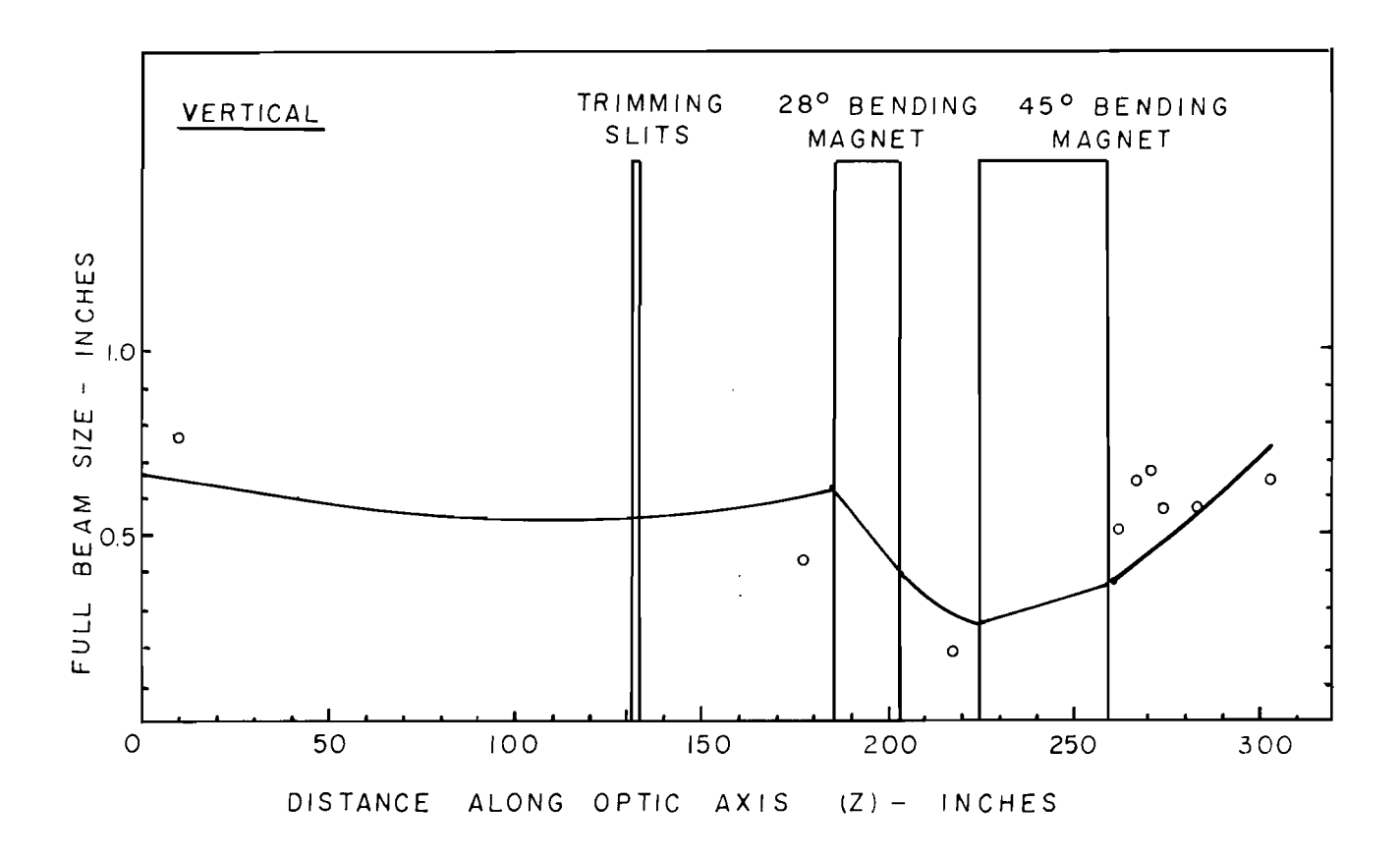


FIG 16 - BEAM ENVELOPE THROUGH DEFLECTION SYSTEM

FIGURE 16a:

HORIZONTAL PHASE SPACE ELLIPSES

These ellipses were obtained by transporting the horizontal phase space ellipse of Fig. 11 through the system.

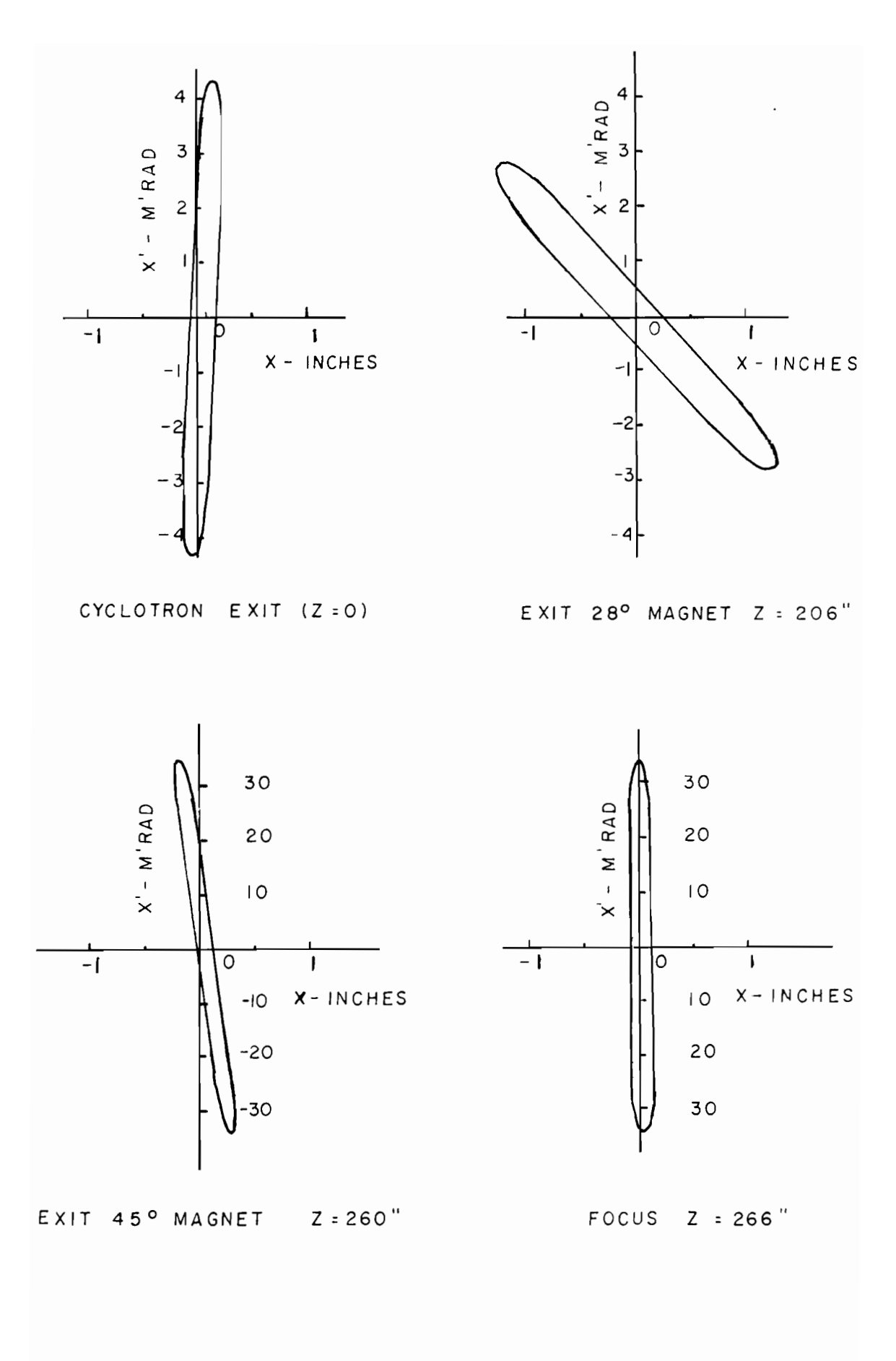


FIG 164- HORIZONTAL PHASE SPACE ELLIPSES

bending magnet system at the focus. This follows directly from the above matrix equation:

$$x = ax_0 + e \frac{\Delta p}{p} \qquad (b = 0)$$

here the coefficient a is the magnification and e the momentum dispersion. Using the transfer matrices of table 4, the dispersion is then calculated to be ~0.34 inches/% momentum spread (or approximately 6 Mev/inch).

The horizontal size of a mono-energetic beam at this point (diverging at 68 milliradians), from the conservation of phase space area, would be 0.012". The size obtained experimentally from the poloroid exposures (~0.2") must therefore be attributed almost entirely to energy spread of the beam. This, in fact, gives a very rough estimate that at least 95% of the beam is included in an energy spread of 1.1%.

- b) Quadrupole Doublets and Switching Facility. In the final alignment of the quadrupole pairs, both possible polarities (vertical focusing first, or horizontal focusing, in both doublets) were checked. The most flexible experimental arrangement uses vertical focusing first; although with horizontal focusing first it is possible to obtain large momentum dispersion due to the very short horizontal focal length of the first quadrupole set (and consequent large magnification). The switching magnet design and pivoted second quadrupole carriage was found to be very satisfactory. The unusual pole piece geometry of the switch magnet gave no apparent distortions due to non-linearities.
- c) Transmission of System. The overall transmission of the system was estimated by coupling a Faraday Cup to the end of the system and comparing the current measured there with that from the external beam monitor Faraday Cup. The transmission was found to be of the order

of 85%. It was suspected that beam losses were probably due to inadequate horizontal aperture of the 28° Bending Magnet. This was verified experimentally by measuring the transmission from the trimming slits to the exit of the 45° Magnet for varying slit positions. In order to avoid beam losses in the 28° Bending Magnet vacuum chamber, and the consequent "halo" of scattered protons of degraded energy, the horizontal trimming slits at z=132" were set at -1.0 cm and +1.7 cm, the 12% beam loss now being at the slits.

d) Reduced Intensity "Clean" Beam. Reducing the intensity of the external beam is an important consideration for many experiments, and if this is done by normal slitting, degraded energy slit scattered protons can significantly increase the accepted energy spread. To eliminate this problem a thin (" \triangle E") collimator of 1/32" copper which could be manually rotated into the beam was located before the trimming slits at z = 131". The present collimator is a 0.030" diameter hole. The degraded portion of the beam is deflected through a greater angle by the deflecting magnets and is stopped at the exit to the 45° Magnet by a brass full range collimator. The picture (5) in plate 1. taken at the exit to the 45° Magnet with the collimator in place, clearly shows the momentum discrimination. The loss in energy of 100 Mev protons in 1/32" of copper is ~ 3.6 Mev (Rich and Madey, 1954). Using these results the momentum dispersion (at the image of the collimator) can be found by the same method as 3.7a to be~ 0.37 inches/% momentum spread or alternately ~5.5 Mev/inch. This compares well with the energy "dispersion" calculated from the displacement and energy loss, ~5 Mev/inch. (These are only intended to be approximate).

It was shown that it is possible to reduce intensities by at least two orders of magnitude by using this thin collimator and produce negligible slit scattered protons.

4. MUMENTUM ANALYSIS OF THE EXTERNAL PROTON BEAM

4.1 Introduction.

The most extensively used method in the experimental determination of proton beam energies makes use of the theoretical range-energy relationship. The range of protons in various materials has been evaluated by a number of authors. An extensive tabulation of proton ranges up to energies of 10 Bev has been made by Rich and Madey (1954), who essentially enlarged upon the calculated values previously compiled by Aron, Hoffman, and Williams (1951). The calculation of the range is based on the Bethe-Bloch (1937) theory of the stopping of charged particles in matter. The ionization loss dE/dx which forms the basis for the range calculations involves the mean ionization potential I of the atoms of the stopping medium. The ionization potential is not calculated precisely by the theory however and must therefore be determined experimentally. Rich and Madey use the approximate relation I = 11.5 Z which was derived from experimental work by Wilson (1941). More recently Sternheimer (1959, 1960) has recompiled the ranges for protons in several substances (Be, C, Al, Cu, Pb, and air) using more accurately determined values for the ionization potential and including shell corrections for the energy loss at low energies. However, even with these refinements Sternheimer estimates an accuracy of only ~1%. Only a few points on the theoretical range-energy curve have been obtained experimentally using absolute methods of energy measurement (Mather and Segre, 1951 at 340 Mev, Bloembergen and van Heerden 1957 at 35 to 120 Mev, Hubbard and MacKenzie 1952 at 18 Mev and Bischell

Mozley and Aron 1957 at 6 to 18 Mev). In most cases the deviation from the theory is of the order of one or two percent.

Using the theoretical range-energy relationship, then, is unsuitable for any measurements to an accuracy of better than one percent.

It was decided, somewhat arbitrarily, to attempt to measure the energy of the McGill external beam to an accuracy of ~0.2%. This accuracy therefore necessitates an absolute measurement of the energy. However, an absolute measurement was felt to be, in itself, of limited practical value, since the energy of the beam depends on many cyclotron parameters and may vary significantly over a period of time. To provide a convenient means of accurately measuring the energy of the external beam at any time, it was therefore decided to obtain a precise experimental point on the range-energy curve in Aluminum near 100 MeV, the energy of protons available from the McGill cyclotron. This point could then be extrapolated sufficiently accurately over a small region about the 100 MeV range by use of the theoretical values for dE/dx, and range-energy then used as a secondary energy measurement.

Several methods for the absolute measurement of the energy of a charged particle beam were investigated to determine which method would be most applicable using the available facilities. A short review of the methods considered follows:

a) General Magnetic Rigidity methods: This method utilizes a bending magnet as a momentum analyser (usually with uniform-field and neutral entrance and exit angles). The accuracy attainable is limited mainly by the difficulty in precisely determining the magnet parameters.

Momentum calibration involves accurate measurement of the angle of deflection and a knowledge of the field map extending well into the fringe-field regions. This method was used very accurately by Bischell et al (1957) in measuring proton energies of 6 to 18 Mev. In general however, accuracies better than 1% are difficult to achieve.

- b) Time of Flight: As the name implies, the momentum of the particles in the beam is measured directly by timing over a known length flight path. With the techniques of fast electronics now available this approach might be feasible but would still be difficult for accurate results.
- c) Calorimetry: The beam energy is directly determined by measuring the temperature increase of a thermally insulated target which stops the beam (typically using thermistors in a bridge circuit: Chambers, 1963). This method is most usefully applied at low energies and has the advantage of being applicable to neutral beams. At higher energies however, a severe limitation in the accuracy is the difficulty in accurately correcting for nuclear (typically p, xn) losses, which are of the order of 15%.
- d) Čerenkov Radiation: A very elegant experiment using this method to measure the energy of a 340 Mev proton beam was performed by Mather (1951) and used in determining the range energy relationship at that energy (precisions of \pm 0.8 Mev). At lower energies however, it becomes difficult to find a suitable radiator with sufficiently high index of refraction. (For theory of Čerenkov radiation see Evans 1955). At 100 Mev diamond with an index of refraction of ~2.5 could be used, but its high dispersion makes precise interpretation of the Cerenkov

angle difficult.

e) The Floating Wire Technique. This method uses a bending magnet as a momentum analyser and in this sense is similar to a), however the problems associated with accurate measurement of magnetic fields are avoided. With some care very good accuracy can be obtained (Cronberg 1951, Citron et al 1959).

The floating wire technique makes use of the close analogy between the trajectory of a charged particle beam in a magnetic field, and the path of a flexible current carrying wire under tension. The basic equations illustrating this analogy are shown as follows: for equilibrium of an element of the wire, under tension \overline{T} , of length s, carrying a current \overline{I} through a magnetic field \overline{B} :

$$\frac{d\vec{T}}{ds} = -(\vec{i} \times \vec{B}) - \vec{G}$$

where \vec{G} represents external forces other than the amperian force (gravitational, friction, etc.). For a particle beam of momentum \vec{p} and velocity \vec{v} :

$$\frac{d\vec{p}}{dt} = e(\vec{v} \times \vec{B})$$

neglecting G and introducing the unit vector \vec{n} in the direction of the particle trajectory or wire configuration gives:

$$\frac{d\tilde{n}}{ds} = -i (\tilde{n} \times \tilde{B})$$
 for the wire

$$\frac{d\tilde{n}}{ds} = \frac{e}{p} (\tilde{n} \times \tilde{B})$$
 for the particle

When the trajectories of the wire and particle coincide, these two equations become identical and:

$$\frac{e}{p} = -\frac{i}{T}$$

using the relation $B\rho = mv/e$ this reduces to:

$$B\rho = -T/i \tag{1}$$

where Bp is the magnetic rigidity characterizing the particles in the beam. The negative sign in (1) indicates that a wire carrying a conventional current in a given direction represents the trajectory of a positive charged particle in the opposite direction. Thus, in principle, to obtain the momentum of a proton beam all that is necessary is to define the trajectory (using slits), and suspend a wire along the same path and measure the ratio of wire tension to wire current holding the field B constant. Tension and current can both be measured to high precision fairly easily; and the limitations to the accuracy of the method can be summarized as follows:

- i) the effect of gravitational force on the wire causes the wire to sag and introduces a correction to the tension T. This is negligible if very fine wires are used.
- ii) the effect of elastic forces due to the wire stiffness; this is also negligible for fine wires (stiffness of a cylinder is proportional to the cube of the diameter) and can be reduced experimentally by annealing the wire in the trajectory with heavier current for a short time.
- iii) the effect of pulley friction; this can be minimized by pulley design.

It was decided after these considerations that the floating wire technique was the most attractive for the purpose of a range energy determination for 100 Mev protons.

4.2 Experimental Apparatus and Procedure.

The essential features of the system are shown schematically in Fig. 17. The external beam switch magnet (described in the previous chapter) was used as the momentum analyser and the beam deflected by approximately 15° for range measurements.

a) Slit system for beam definition: an extremely monoenergetic and spatially well-defined pencil beam was obtained with slits 1 and 2 shown in Fig. 17. Slit I was located at the exit to the first quadrupole pair at z = 340" and slit 2 at the entrance to the switch magnet at z = 443". Both slits 1 and 2 consist of a thick (full energy) copper slit followed by a thin (Δ E) copper slit as shown in Fig. 17. Thin slits were used to define the pencil beam in order to minimize the energy spread and scattering effects of slit edge penetration. degraded components of the beam passing through the slits are effectively separated from the full energy component by the momentum dispersion of the switch magnet. Both slits 1 and 2 were insulated from the slit housings with plexiglass; this permitting the use of slit 1 as a monitor in the counting system and slit 2 as a contact to detect movement of the floating wire. A thin slit (slit 3) with a 1/4" vertical aperture to define the beam in the vertical plane was located at z = 444"; the final slit (slit 4) was located at z = 723" (at the end of the external beam system) and defines the deflected beam vector. This slit was thick enough to stop the full energy protons. All three horizontal slits could be moved across the beam to allow flexibility in alignment and slit I could be remotely adjusted by means of a "selsyn" servo motor.

FIGURE 17:

EXPERIMENTAL LAYOUT FOR RANGE ENERGY MEASUREMENT

In the floating wire momentum measurement, the balance frame was located at the exit of slit 4 and the wire clamped at the centre of slit 1.

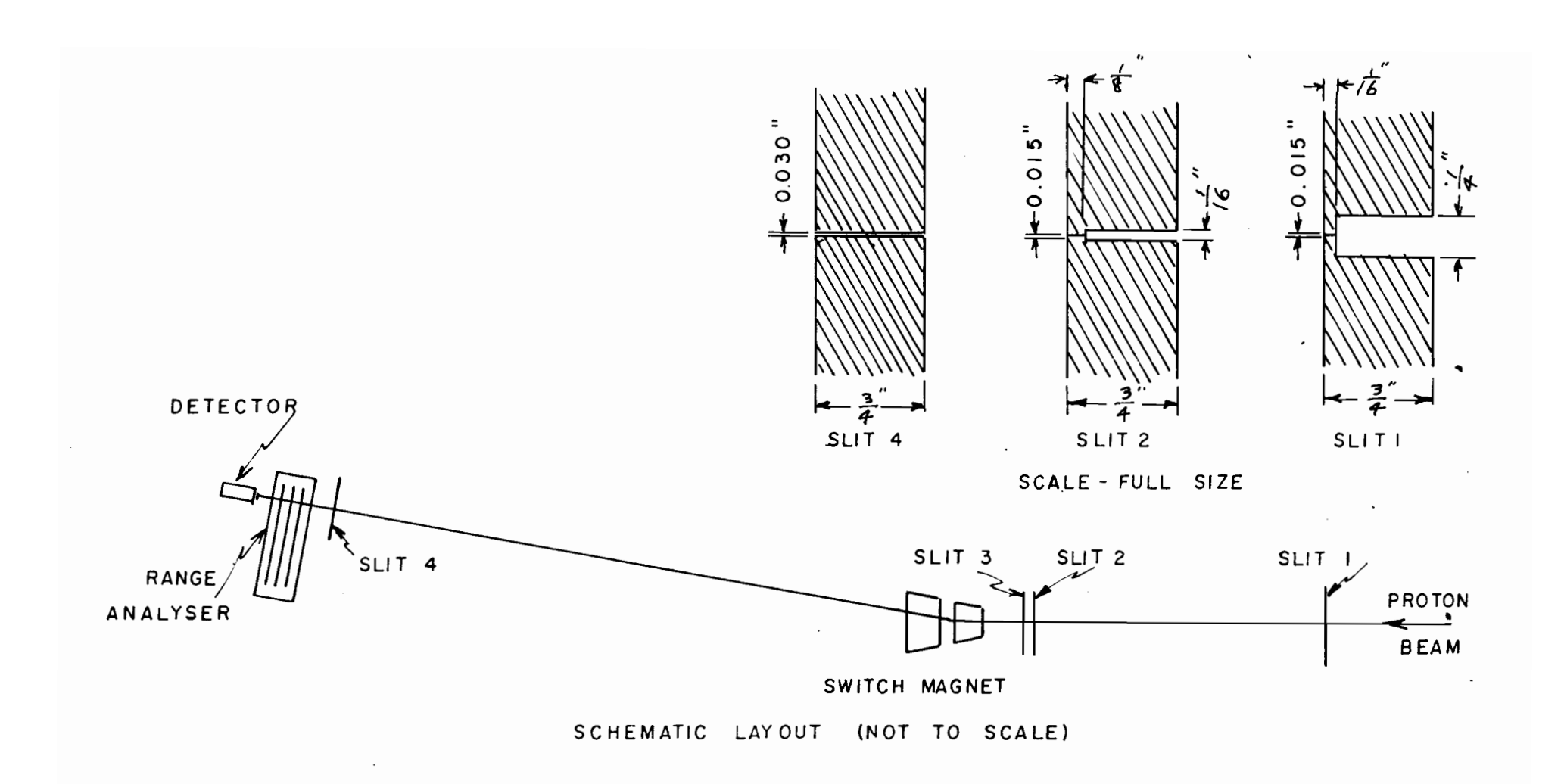


FIG 17 - EXPERIMENT LAYOUT FOR RANGE ENERGY MEASUREMENT

Slits 1 and 2 effectively define the horizontal area in phase space accepted by the system.

b) Proton Detection and Counting System. The vertical slits defining the pencil beam had an acceptance of approximately .05% of the total beam in the horizontal plane and the horizontal slit approximately 20% in the vertical plane. The overall acceptance was therefore .01%. Thus a beam flux of somewhat less than 10^{-12} amps or 10⁶ protons per second could be expected. This effectively eliminated the use of Faraday Cups or secondary emission techniques for the measurement of the beam current. Therefore a scintillation counter was used to detect individual protons which necessitated a further reduction of two orders of magnitude in beam intensity to avoid pile up in the detector. Two detectors were used during the course of the experiment. A full range plastic Naton scintillator 1 1/2" diameter x 3" coupled to an RCA 6342 photomultiplier was used to detect the protons while aligning the slit system on the pencil beam. A 0.1" x 1 3/4" diameter plastic Naton scintillator coupled to a CBS 7817 photomultiplier was used in the range measurement. The use of a thin scintillator minimized background scintillations from sources other than the protons themselves.

The energy deposited in the dE/dx scintillator varied from ~1.8 Mev at a proton energy of 100 Mev to a maximum of 15 Mev, corresponding to the maximum energy completely stopped in 0.1" of Naton.

Pulses from the eighth dynode of the photomultiplier were sent through a White cathode follower, amplified, and counted in a 256 channel kicksorter (Technical Measurement Corporation, Model CN-110).

Background counts which appeared almost entirely in the channels corresponding to proton energies below I Mev were subtracted by estimating the true proton counts in these channels from the overall count spectrum. The counting periods were normalized by use of a monitor on the first slit. The current incident on this slit was integrated by a Keithly micro-microammeter modified to indicate charge collected.

- energy measurement were made by stacking 3" diameter, 0.012" thick 99% pure (1S) aluminum discs. The mass per unit area of each absorber was very carefully measured to an accuracy of better than 0.05%. The absorbers were mounted on three motor driven wheels inside a vacuum chamber. The positions of these wheels and therefore the thickness of the absorber could be remotely controlled, and absorber thickness from 0 to 11 gm/cm², in steps as low as ~50 mg/cm², readily obtained. The range analyser vacuum chamber was coupled directly to the vacuum system of the external beam. A thin 0.001" aluminum alloy window at the exit of the analyser chamber permitted placing of the detector within 3/8" of the absorbers, to minimize counting losses due to multiple scattering. For this reason, too, the heaviest absorbers were mounted in the wheel closest to the detector.
- d) Floating Wire System: In the use of this technique, constant tension in the wire is generally provided by passing the wire over a pulley and hanging a known weight from it. In pulleys of conventional design however, the friction at the bearing gives rise to an uncertainty in the actual tension on the wire which is difficult

to reduce to less than 1%. A more accurate conversion of vertical into horizontal force can be achieved by means of a frame pivoting on a knife edge (Citron et al, 1959). The design used here is shown schematically in Fig. 18 and in more detail in the photograph of The frame is made of aluminum and the lever arms are Plate 3. approximately five inches long. The knife edge was made from an injector type razor blade and was mounted in the frame, held in a brass collar 1/2" in diameter. The knife edges rest on supports mounted on a heavy brass base. This base was supported by a platform with steel runners parallel to the wire. The motion of the base with respect to the fixed platform allowed the frame to be relevelled after a movement of the wire. A balancing screw was provided to allow leveling of the horizontal arm of the "pulley". Stable equilibrium was achieved by ensuring that the centre of gravity of the frame was approximately 1/8" below the knife edge.

A set of weights giving a range from ~60 gm to ~120 gm in ~20 gm steps was made and very accurately weighed on an analytic balance.

The wire used was 0.0035" diameter formel, copper wire. Where it was necessary to bare the wire for electrical contact, the formel was removed with "strip var" (Walsco Chemicals Ltd.). The wire was fixed in the centre of slit 1 with a specially constructed clamp having a 0.0075" lip which ensured positive centering in the 0.015" slit. Contact to this end of the wire was made through the slit. In order to hang the wire along the beam trajectory, it was necessary to break the system vacuum, and remove the vacuum pipe section between the first quadrupole set and the switch magnet, and the switch magnet and

FIGURE 18:

THE BALANCE FRAME

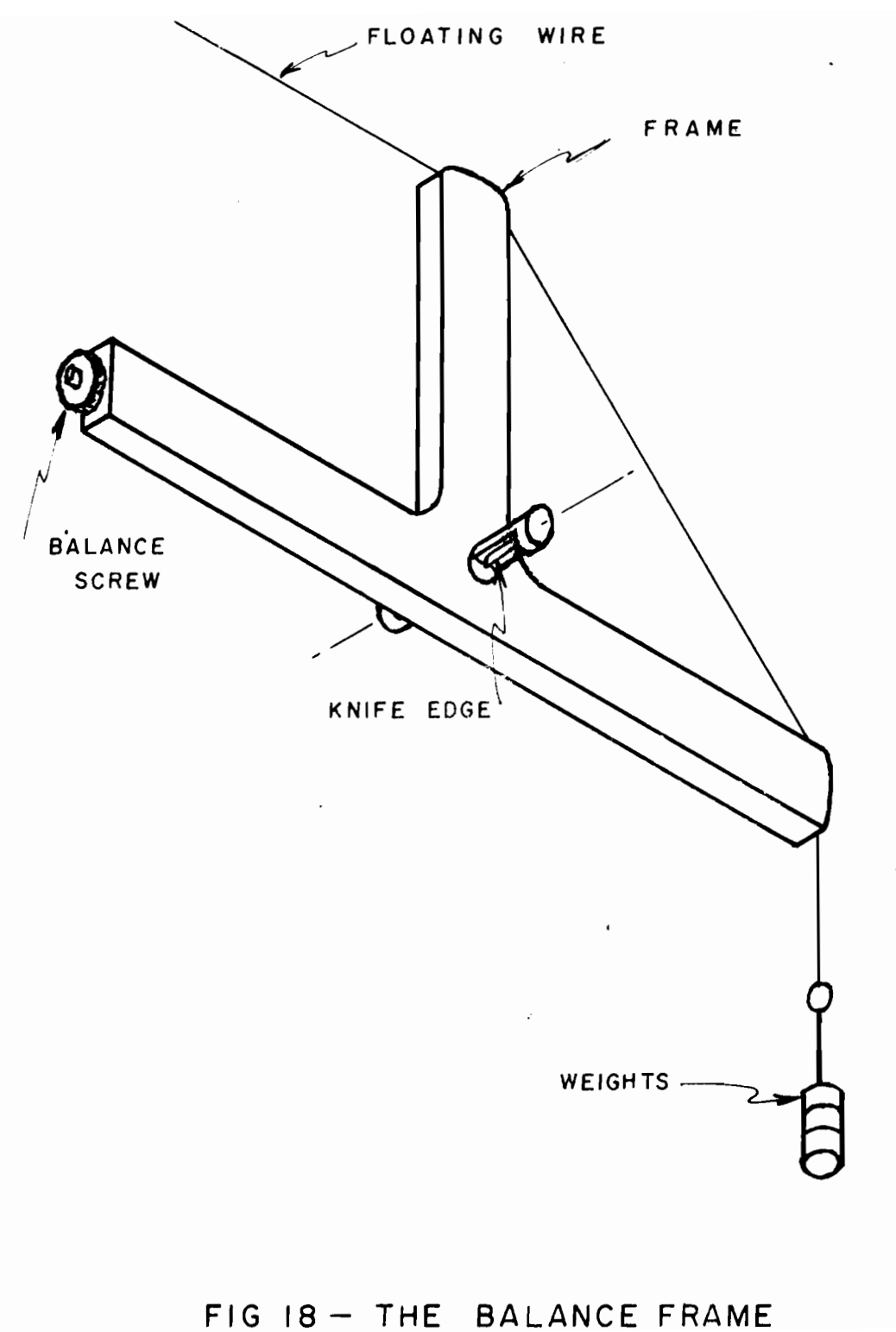
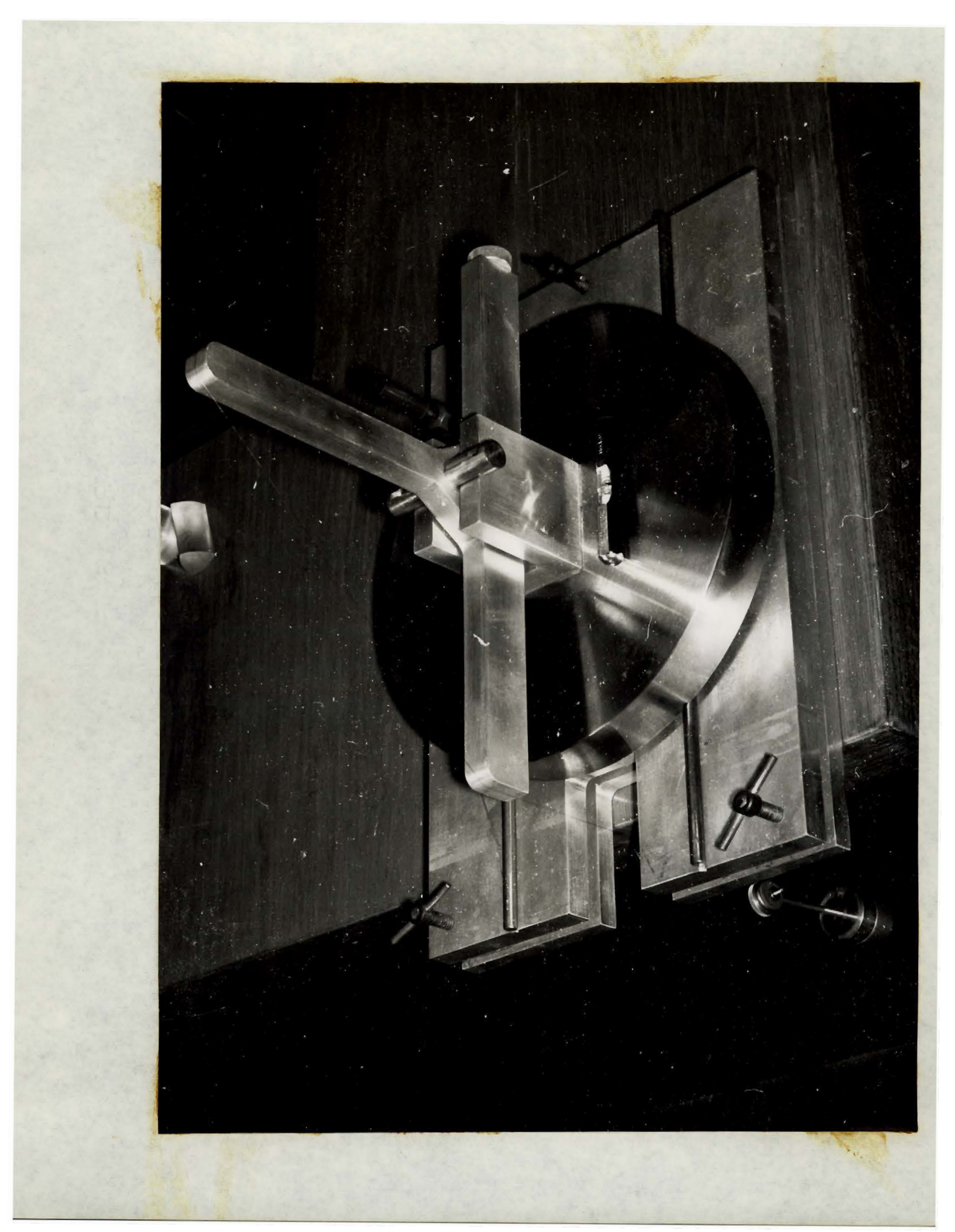


PLATE 3:

THE BALANCE FRAME USED IN THE FLOATING WIRE MEASUREMENT

This photograph shows the essential features of the Balance Frame. The leveling adjustment screw, and the knife edge resting on its supports can be readily seen, as can the configuration of the wire, and the hanging weight. The base slides on steel runners over a platform which can be levelled with three level screws.



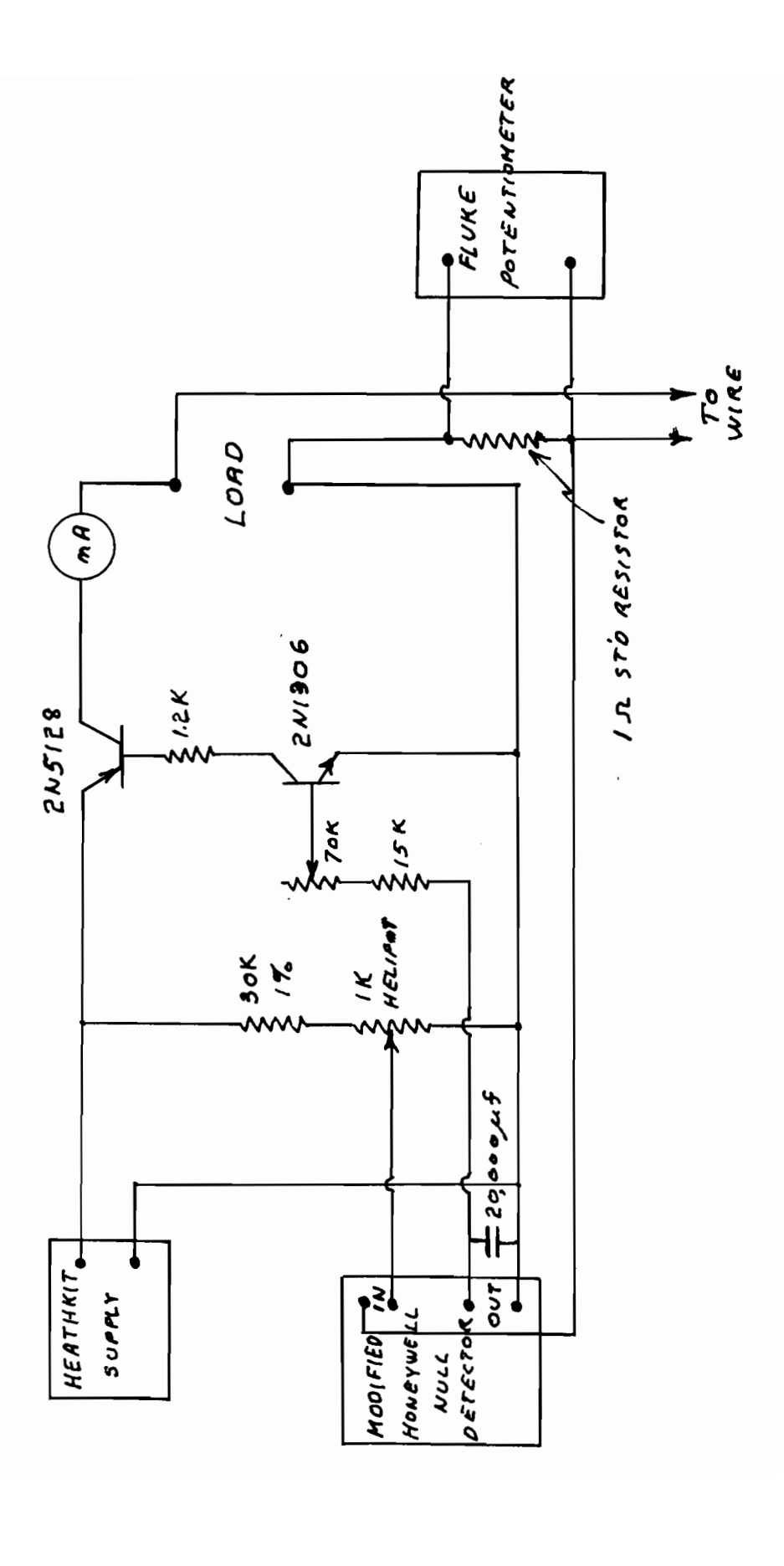
the second quadrupole set. The pulley was located immediately after slit 4 and the wire threaded through the slits and over the balance frame and attached to the known weights. Electrical contact to the wire at this end was made by baring the wire where it was in contact with the frame and fixing a terminal in the brass base. There was good electrical contact between the knife edge and the base. In operation the frame was initially levelled with a theodolite and a reference mark established for levelling with the wire in place. In aligning the wire two methods were used.

The portion of the wire passing through slit 2 was bared and contact between the wire and the slit was observed by measuring the voltage between slits 1 and 2 with an oscilloscope. In addition a theodolite was used as a telescope to visually centre the wire in the 0.015" slit 2. The wire was centred in slit 4 by eye. In order to centre the wire in the magnet gap, the sag (approximately 3/8" in 400 feet) was offset by raising the wire slightly at slit 1 and slit 4.

The current for the wire was provided by a Heathkit transistorized regulated 50 volt power supply (model IP20), with additional external series regulation. Details of the current regulator are shown in Fig. 19. It was found necessary to hang a 21,000 μ f capacitance across the output of the Honeywell D. C. amplifier to reduce a large 60 cps signal. Regulation was observed to be extremely good (one or two parts in 10^4). The current was determined by measuring the voltage across a standard precision one ohm resistor (Rubicon Bureau of Standards type 1100) with a John Fluke model 801 Potentiometric D. C. Voltmeter, which in turn was calibrated against a Rubicon type B potentiometer.

FIGURE 19:

FLUATING WIRE CURRENT REGULATOR



CURRENT REGULATOR WIRE FIG 19 - FLOATING

e) Switch Magnet Monitor. The voltage across the series regulator shunt in the switch magnet was continuously recorded throughout the experiment by balancing most of the voltage across a Rubicon type B potentiometer in series with a Leeds and Northrup 10 my recorder.

4.3 Experimental Range-Energy Results

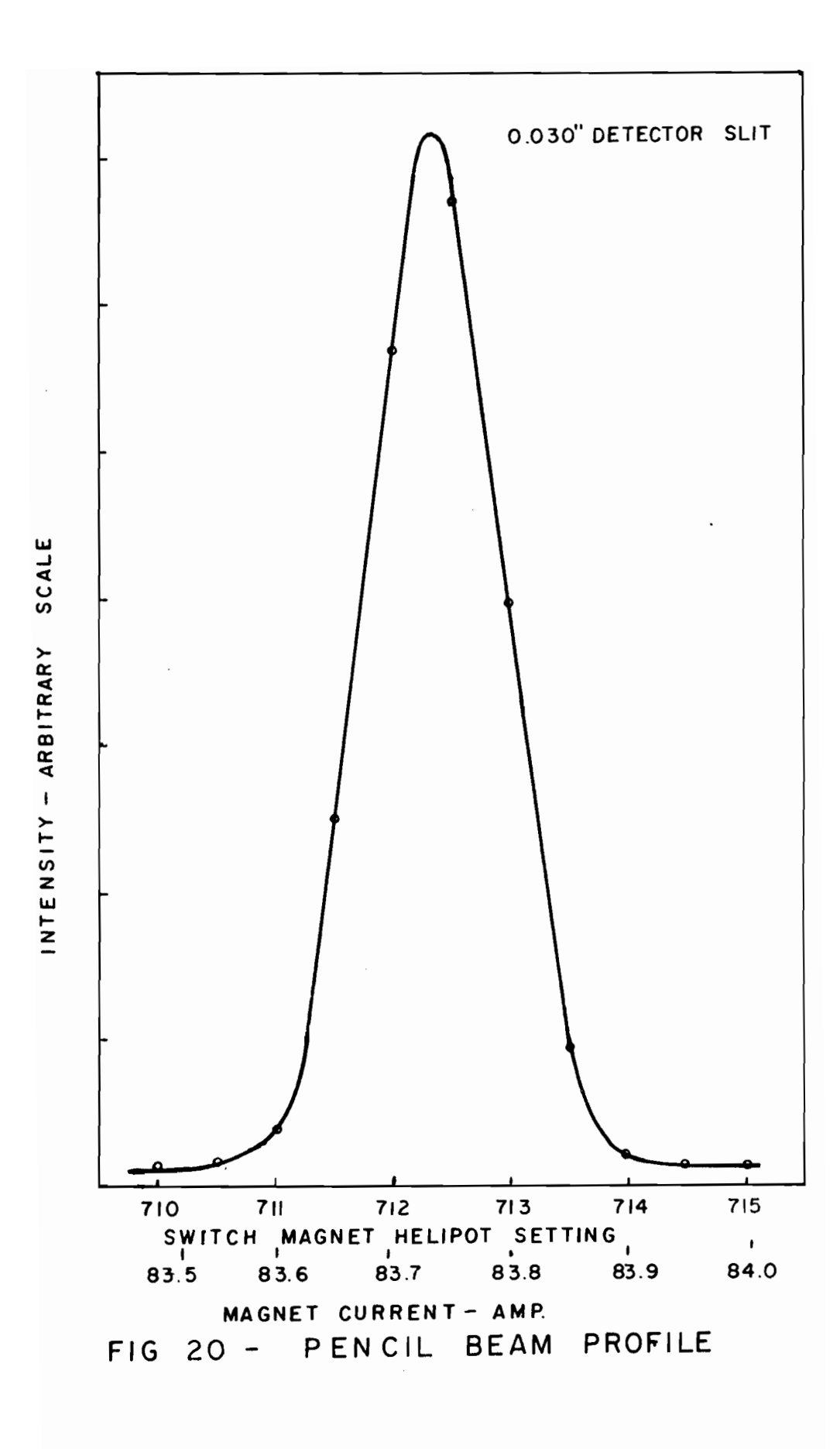
a) Alignment of Pencil Beam. Slits 2, 3, and 4 were fixed and the pencil beam aligned very carefully by sweeping the beam profile across the detector slit (4) with the switch magnet, and optimizing the settings of the two deflection bending magnets (28°) and 45° Magnets). This procedure was found to be very critical due to the size of the slits and the precision in alignment necessary. The first slit was then moved into position and all parameters adjusted for minimum slit scattered background. The full energy scintillation counter was used and it was found necessary to reduce the beam intensity by detuning the cyclotron(the oscillator plate voltage and dee voltage were reduced). The profile of the pencil beam obtained is shown in Fig. 20. The counting period was normalized by counting for a fixed monitor reading, Rough dead time corrections were made on the basis that the dead time of the counting system here an aptimeter (Model 361-R) triggered by a Tektronix oscilloscope (585) - was greater than the beam burst length, about 15μs. profile represents a spatial spread of about 1/8" as calculated using the transfer matrix for the switch magnet and later verified with a polaroid exposure.

The 0.030" slit (4) was then withdrawn to eliminate any possibility of slit edge penetration and degrading and the dE/dx

FIGURE 20:

PENCIL BEAM PROFILE

The profile was obtained by sweeping the beam across a 0.030" slit in front of the detector. The profile represents a spatial spread of approximately 1/8".



counter used for the range determination. Here again the counting period was normalized to the incident flux by the use of the monitor on slit 1. The transmission through the absorber plotted against the absorber thickness is shown for the end of the range in Fig. 21 (again corrected for dead time losses). The number of protons traversing the absorber was determined from the individual kicksorter spectra obtained at each point on the range curve. The kicksorter was energy calibrated by an estimation of the energy loss in the scintillator for several residual proton energies (using range energy tables for aluminum and CH by Rich and Madey, 1954). It was found that zero energy in fact corresponded to zero channel (with base line set at zero). Corrections were estimated for background, and for low energy protons that would have been counted in the inoperative first three channels of the kicksorter.

The thickness of aluminum absorber corresponding to the mean range was found to be $9802 \stackrel{+}{-} 7 \text{ mg/cm}^2$ (using the more accurate probability plot). The mean range is defined as the thickness of absorber at which half the protons are transmitted. Making corrections to the above range for the aluminum thin window at the exit of the analyser (7.4 mg/cm^2) and the aluminum foil used to cover the scintillator (4.7 mg/cm^2) gives a final mean range of $9814 \stackrel{+}{-} 7 \text{ mg/cm}^2$. The straggle (a gaussian distribution of the range of an initially monoenergetic beam, due to the statistical nature of the stopping process) obtained from the range curve was calculated to be $2.75 \stackrel{+}{-} 0.20\%$ full width at half maximum.

The energy measurement using the floating wire technique followed

FIGURE 21:

RANGE CURVE FOR ALUMINUM

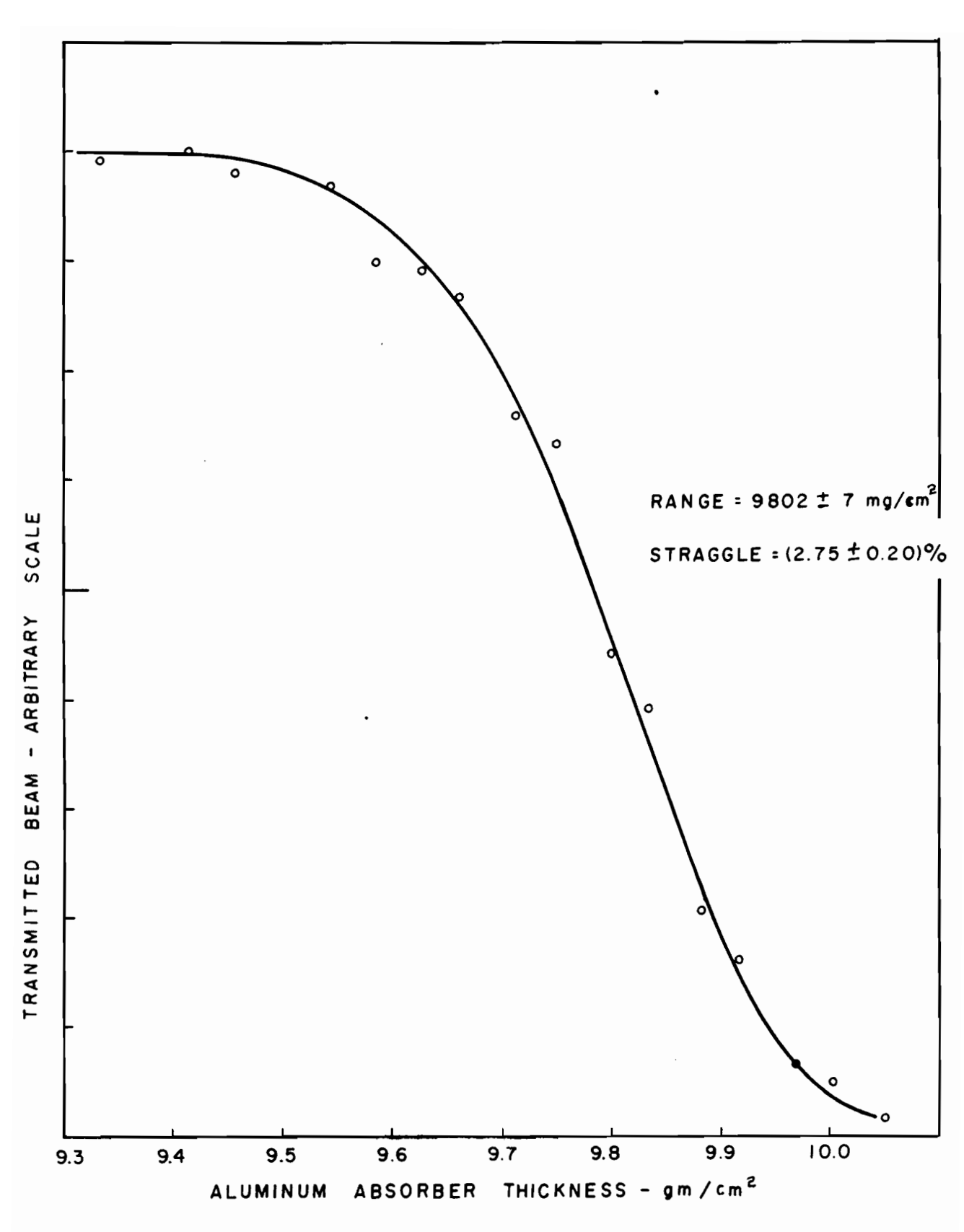


FIG 21 - RANGE CURVE FOR ALUMINUM

immediately after the range energy determination. Slit 4 was reset to the centre of the beam. Dismantling the vacuum system and hanging the wire was a fairly lengthy process and the switch magnet was therefore monitored continuously to detect any changes in the field over this period. The largest variations were of the order of 2 or 3 parts in 10^4 . The wire was very carefully aligned for four different weights and the results of these measurements are tabulated in Table 5 below.

TABLE 5

Floating Wire Energy Calibration

Weight	Tension	Current	Magnetic Rigidity	Energy
gms.	gms.	ma.	Bρ Kg.ins.	Mev.
62.451	62.072	410.7	583.5	99.89
81.953	81.456	539.0	583.4	99.87
102.010	101.391	670.9	583.5	99.88
121.519	120.781	799.2	583.5	99.88

(The value of g was taken to be 980.6 in these calculations).

The consistency of the results is a good indication of the precision with which this method can be used. The sensitivity of the pulley (an indirect test for any frictional couple) was investigated by adding a 100 mg weight when the system was in equilibrium. It was found that a corresponding 0.1% increase in current had to be made

to restore equilibrium. The two lever arms were very carefully measured with a traveling microscope, the results of several measurements yielding a mean value of 126.558 ± 0.020 mm for the horizontal and 127.331 ± 0.010 mm for the vertical arm. This introduces a correction factor of 0.99393 ± 0.0003 by which the weight must be multiplied to obtain the true tension.

An estimation of the errors involved in this measurement indicates a maximum error of $\pm 0.03\%$ in the momentum or $\pm 0.06\%$ in the energy. The width of slit 2 was found experimentally to represent an energy variation of $\sim 0.2\%$. The weight of the wire gave rise to a sag of approximately 3/8" for the lightest weight used and this represents a negligible correction to the tension. The energy measurement then is given as 99.88 ± 0.06 MeV. This new calibrated point on the range energy curve and its error limits are compared to the theoretical values of Rich and Madey (1954) and Sternheimer (1959) in Fig. 22. The deviations of the theoretical curves from the experimental point for a range of 9814 mg/cm^2 in aluminum are summarized below:

Rich and Madey give: 99.78 Mev differing from the experimental point by -0.1%.

Sternheimer's tabulation gives: 98.87 MeV differing from the experimental point by -1.0%.

The measured straggle of 2.75 $\stackrel{+}{=}$ 0.20% compares well with the value for 100 Mev obtained from a tabulation by Sternheimer (1960) of 2.83% (full width at half maximum).

FIGURE 22:

THEORETICAL RANGE ENERGY CURVES

The experimentally determined point 99.88 ± 0.06 MeV at 9814 ± 7 mg/cm² is shown compared to the theoretical range curves of Rich and Madey (1954) and Sternheimer (1959).

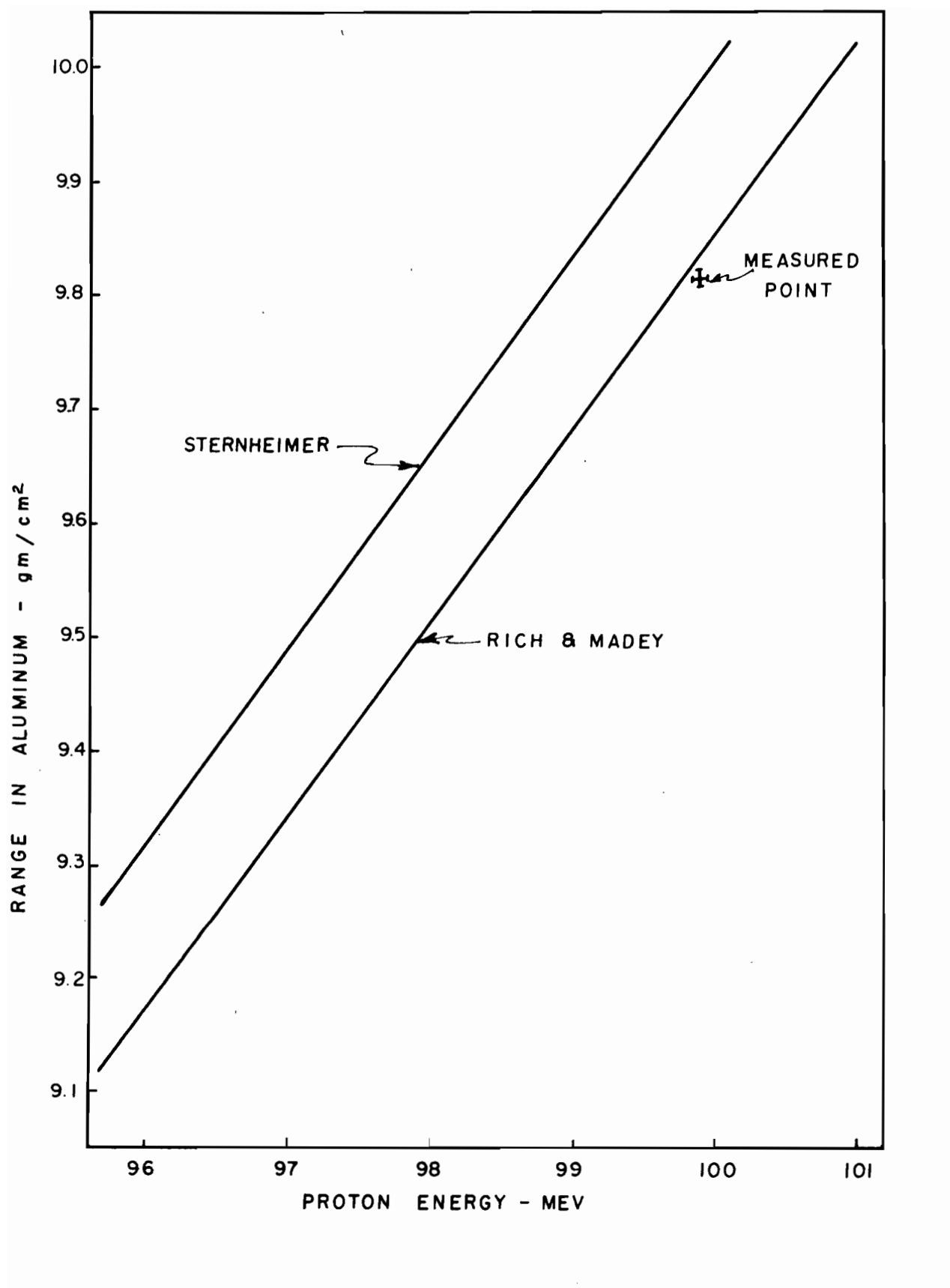


FIG 22 - THEORETICAL RANGE ENERGY CURVES

4.4 Determination of the Energy and Energy Spread of the External Beam

The range analyser was set up at the exit to the second quadrupole set and the proton beam focused to a small spot at the exit window was viewed on a fluorescent screen. A Faraday Cup was then coupled to the analyser in place of the exit window and a range energy curve obtained for the whole beam. (The trimming slit settings were -1.0, +1.7 horizontally and -1.0, +1.0 vertically). The current from the Faraday Cup was measured with a Keithly micro- microammeter, and was normalized by measuring the total beam current in the external beam monitor Faraday Cup. The resulting range energy curve is shown in Fig. 23. The first plot shows the complete curve and illustrates the initial attenuation of the beam due to nuclear losses (in this case 17% which agrees well with a rough calculation using a cross section of $2\pi R^2$ for removal of protons from the beam by nuclear The mean range in aluminum for the whole beam was found to be 9835 mg/cm² which corresponds to an energy of 100.0 Mev (using the experimental range energy point and extrapolating with Rich and Madey's theoretical value for dE/dx).

In order to get an indication of the energy spread of the beam, the analyser and Faraday Cup were located after a 0.030" slit at the horizontal crossover downstream from the 45° Magnet. The slit was moved horizontally across the beam by remote control utilizing a "selsyn" servo motor, and the beam profile obtained by measuring the current collected in the Faraday Cup at 0.025" intervals. Here again the measured current was normalized by using the external beam monitor cup. The profile obtained is shown in Fig. 24 and shows the same

FIGURE 23:

RANGE IN ALUMINUM OF TUTAL BEAM

This range curve was obtained with a Faraday Cup as the detector.

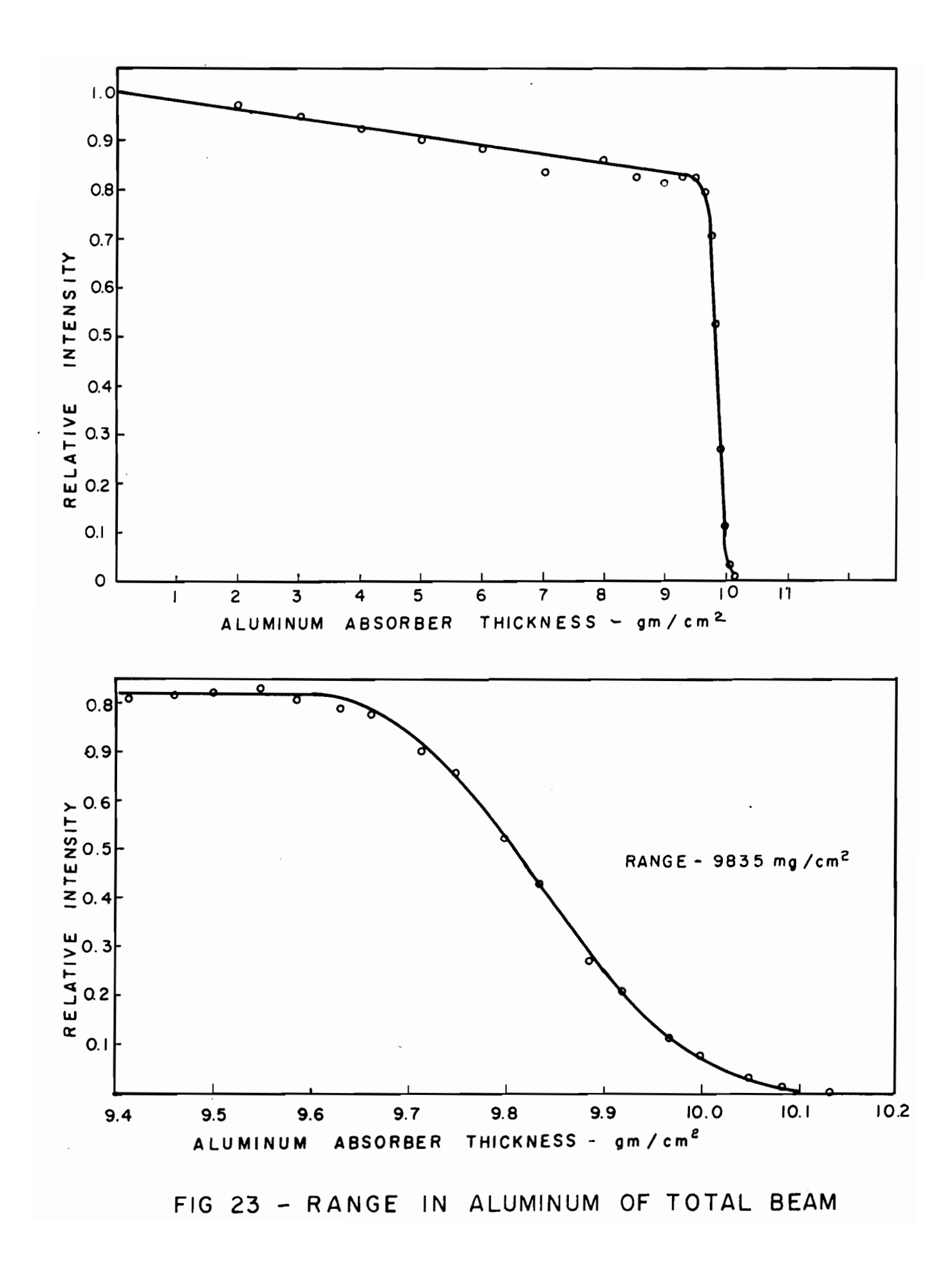
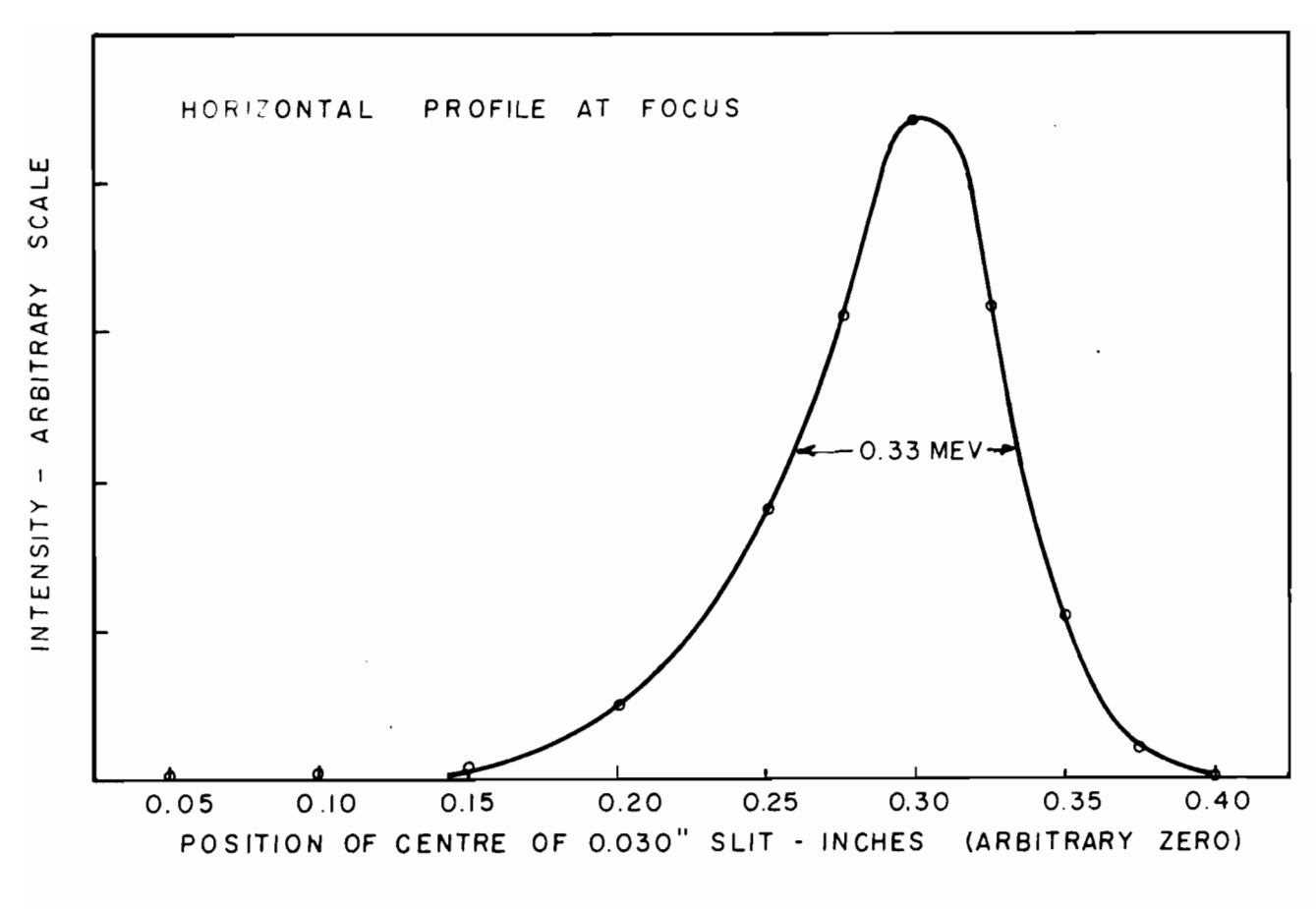
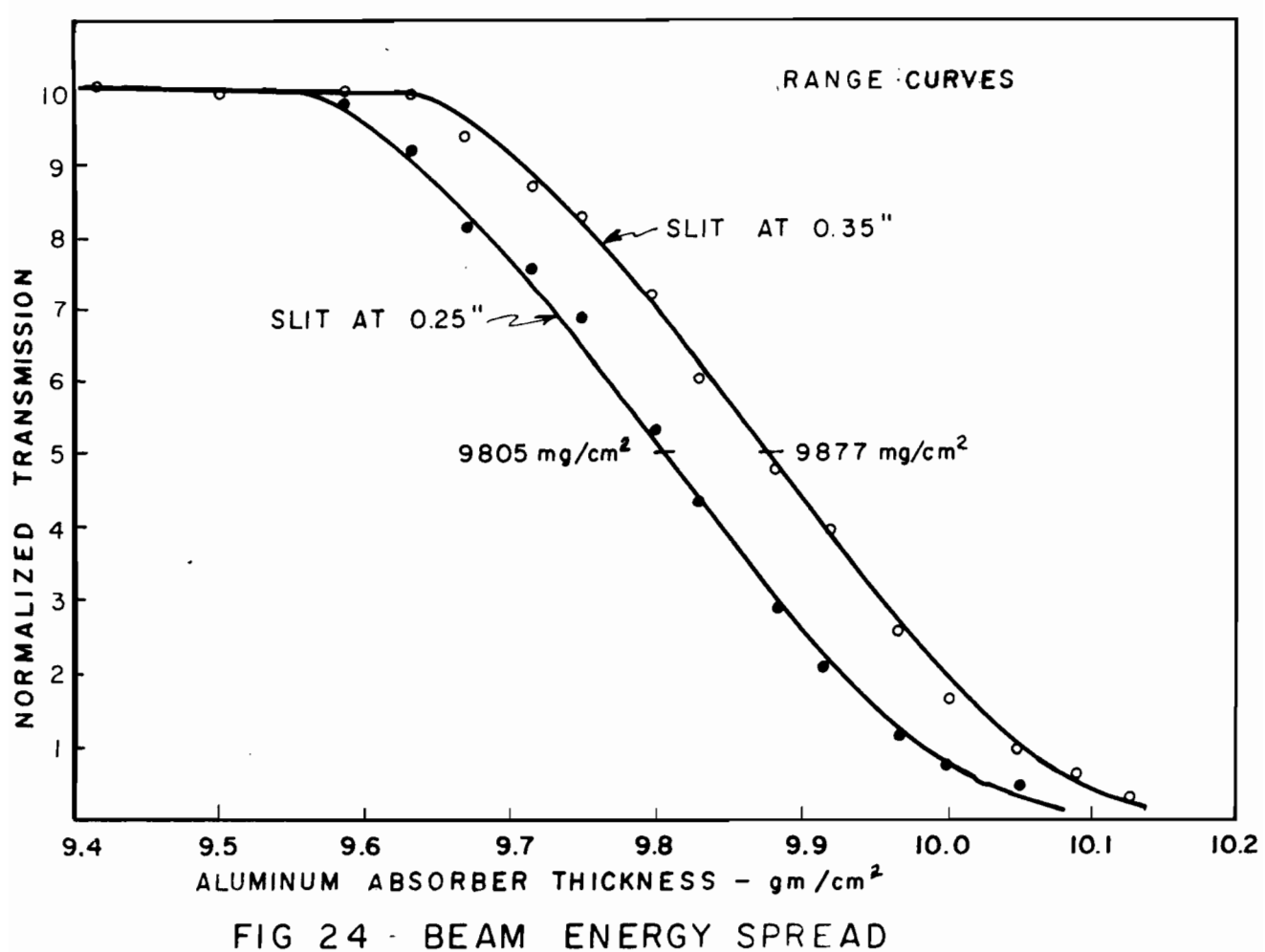


FIGURE 24:

BEAM ENERGY SPREAD

The first curve represents a horizontal profile obtained at the degrader focus by moving a 0.030" slit across the beam. The range curves were obtained with the 0.030" slit centred at 0.25" and 0.35" (arbitrary zero).





horizontal size as was indicated previously by polaroid exposures. A range energy determination was then performed with the slit defining a small portion of the beam on either side of the profile. range energy curves (also normalized) are also shown in Fig. 24. The mean ranges on the low and high energy sides of the beam were found to be 9805 mg/cm² and 9877 mg/cm² respectively. These ranges correspond to energies of 99.84 Mev and 100.28 Mev respectively. This indicates an energy dispersion of 4.4 Mev/inch (the measurements were made 0.10" apart). This is in good qualitative agreement with the results obtained earlier (see Chapter 3) by other methods. The horizontal size of the beam at this focus should be 0.012" on the basis of phase space area, if the beam were perfectly monoenergetic. It is therefore reasonable to consider the profile to be a momentum distribution of the beam. Assigning this profile the energy dispersion obtained in the range energy measurement above, an energy spread (full width at half maximum) of 0.33 ± 0.03 MeV is obtained (the uncertainty being mainly due to back-lash in positioning the slit). energy spread appears to be considerably larger due to a long, low energy tail. The energy of the centroid of the profile is 100.07 Mev which agrees well with the previous measurement of the total beam energy (the mean energy is somewhat lower, actually, due to the low energy tail).

5. CONCLUSION

No major difficulties were encountered in the installation of the external beam transport system, and in general its performance followed design predictions very closely.

The extraction system was optimized and a final external beam intensity of 2.5 x 10^{-8} amperes or 1.6 x 10^{11} protons/sec obtained for an extraction efficiency of ~2.7% (internal beam ~0.9 μ amp.).

The floating wire technique was used very successfully in the momentum analysis of the external beam. An accurate point at 99.88 ± 0.06 Mev corresponding to 9814 ± 7 mg/cm² was found on the range energy curve using a monoenergetic pencil beam. This point was used to calibrate a range measurement of the external beam and the beam was found to have an energy of 100.0 Mev with an energy spread of 0.33 Mev (full width at half maximum).

Photographs taken at the time of writing are included to illustrate some of the main features of the transport system.

Plate 4 shows the start of the beam transport system at the exit gate of the cyclotron. Plate 5 shows the thin collimator, trimming slits, and Faraday Cup; Plate 6, the elements of the deflection system, the 28° and 45° Bending Magnets; and Plate 7 a view of the switching magnet and focusing guadrupole facilities in the beam hall.

PLATE 4:

BEAM EXIT FROM THE CYCLOTRON

In the background are the cyclotron exit slits and further forward the exit gate and external beam fore-pump manifold can be seen. The exit gate is protected by a thermo-couple at the far end of the beam system and can be remotely controlled.

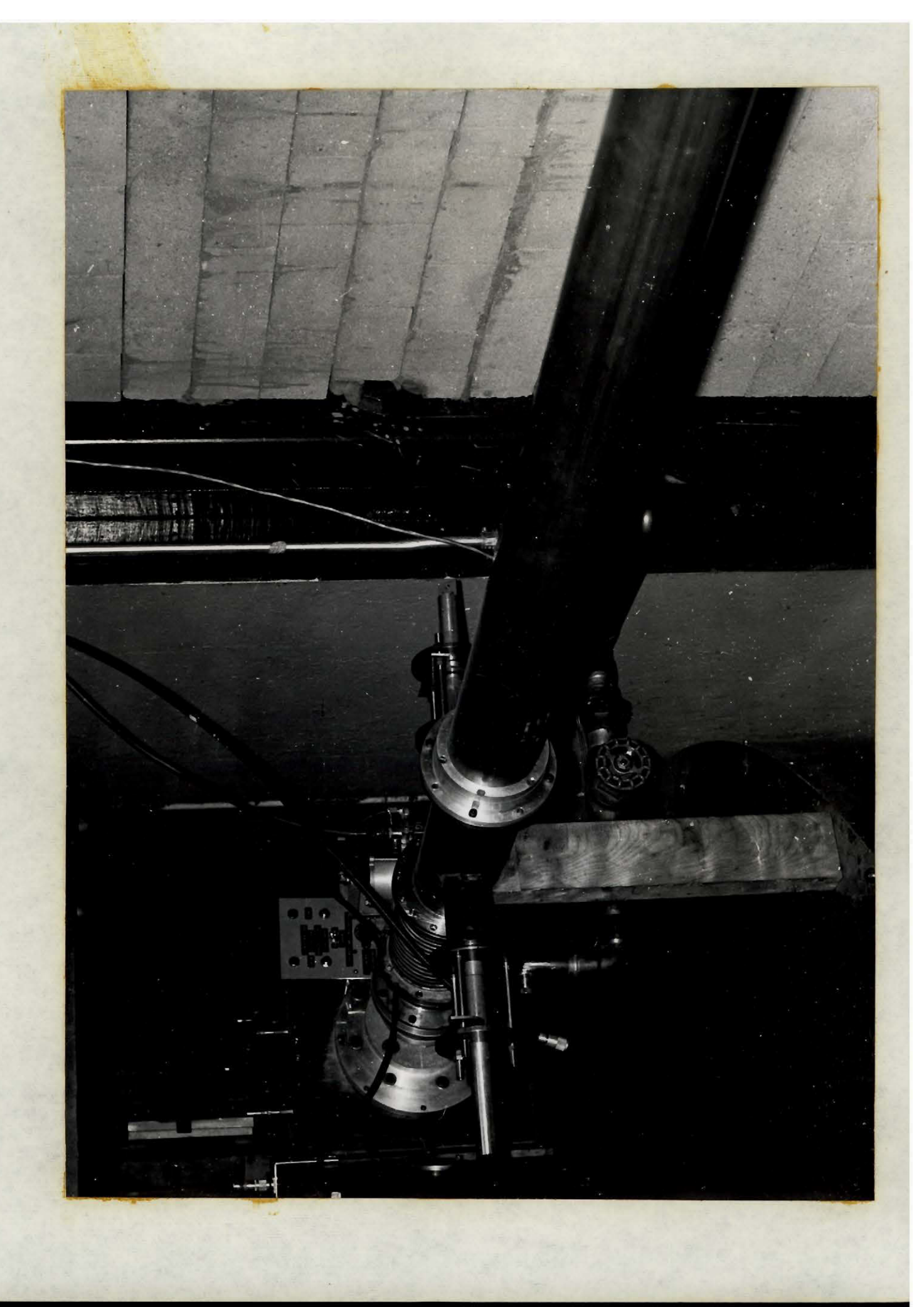


PLATE 5:

THE THIN COLLIMATOR, TRIMMING SLITS, AND FARADAY CUP

This photograph shows (from left to right), the thin collimator, position knob, the vertical and horizontal trimming slits, the cup bias ring, and the Faraday Cup. The solenoids used to rotate the cup end can be seen with their rack and pinion motion. In the rear is a "selsyn" servo motor used to drive the horizontal trimming slits remotely.

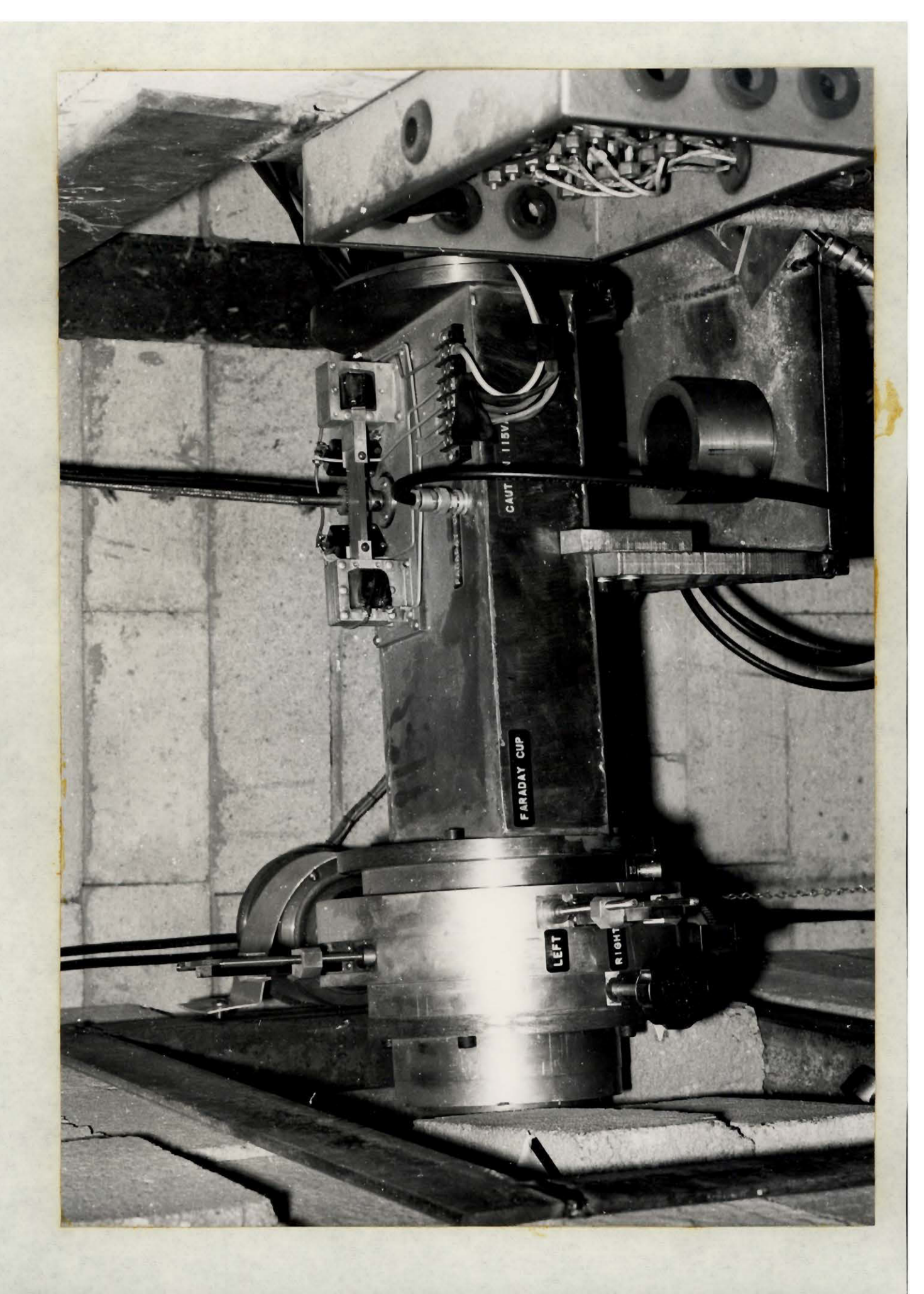


PLATE 6:

THE DEFLECTION MAGNETS

From left to right: the 28° H-frame bending magnet with the cooling system for the coils clearly evident, and the 45° C-frame bending magnet can be seen. Note also the straight through sections of the vacuum chambers which permit the setting up of auxiliary experimental stations.

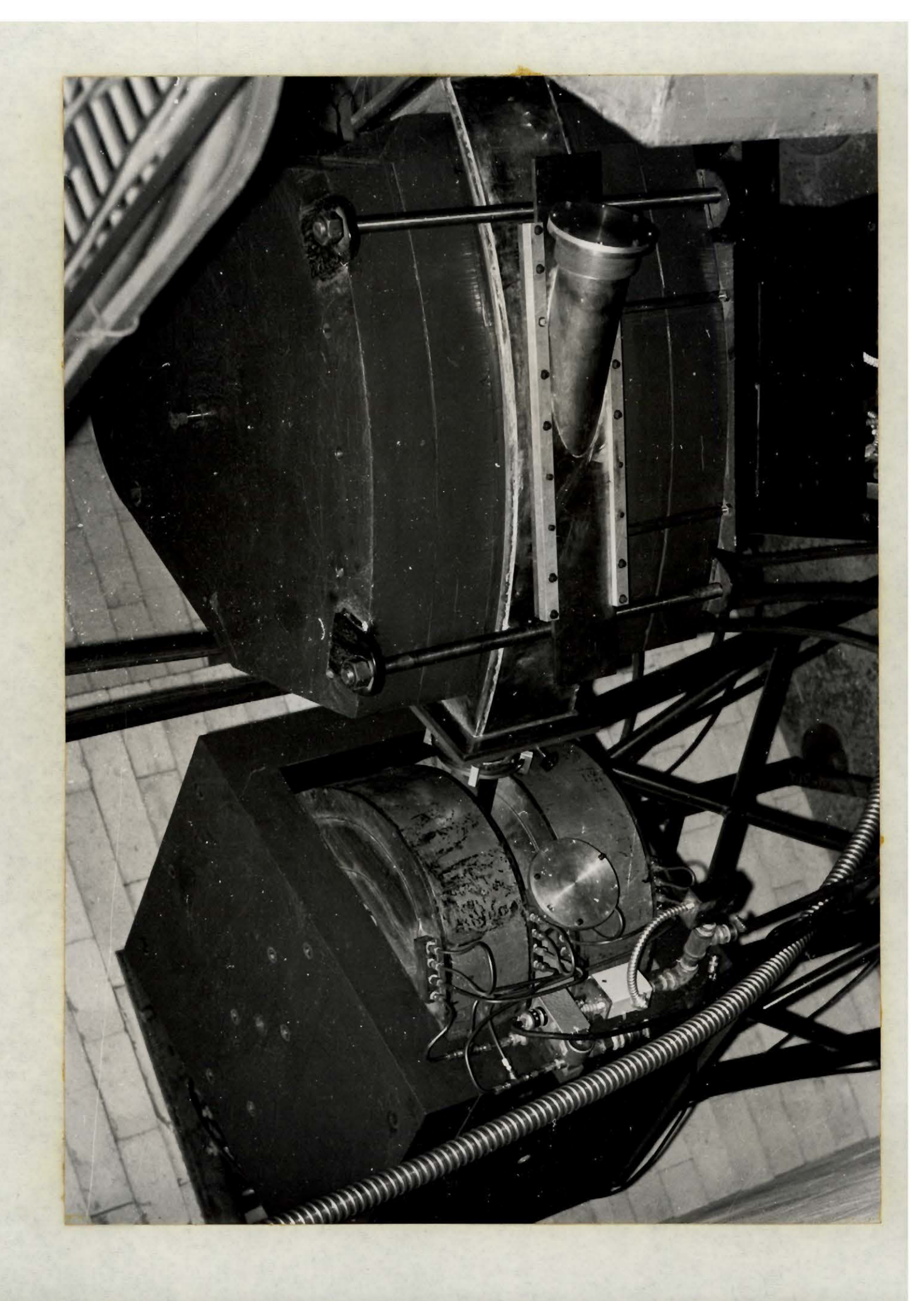
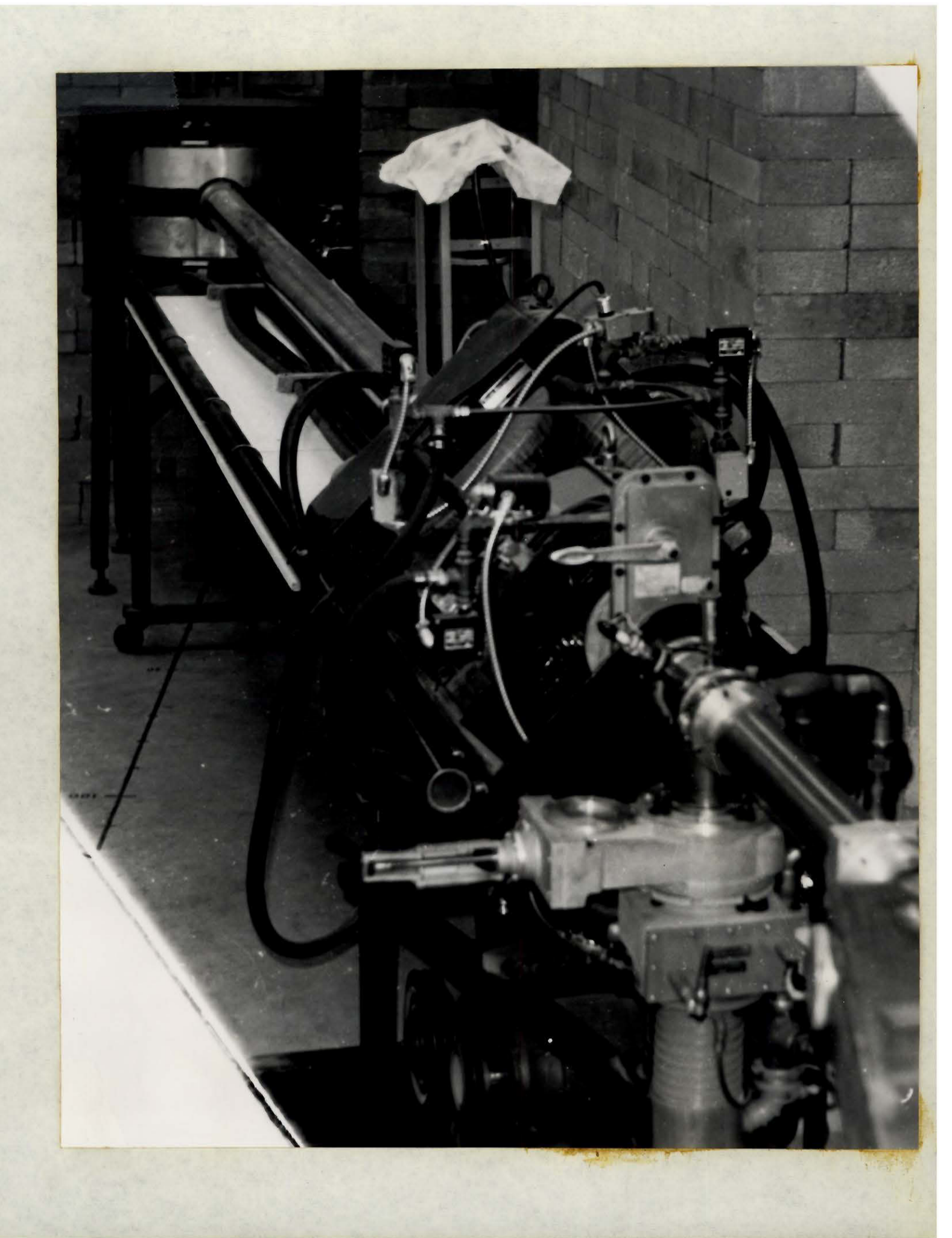


PLATE 7:

SWITCHING AND FOCUSING FACILITY IN THE BEAM HALL

The switch magnet can be seen in the background, and the carriage supporting the second quadrupole doublet, and much of the external beam vacuum equipment in the foreground. In the upper central part of the photograph is the television camera viewing the second view box which is out of view here.



BIBLIOGRAPHY:

ARON, HOFFMAN, and WILLIAMS. 1951. AECU - 663 (Unpublished)

BARTON, R. D., McPHERSON, R. 1963. Can. J. Phys. 41, 2007.

BISCHELL, H., MOZLEY, R. F. and ARON, W.A. 1957. Phys. Rev. 105, 1788.

BLOEMBERGEN, N., and VAN HEERDEN, P.J. 1951, Phys. Rev. 83, 563

BROWN, K.L., BELBEOCH, R. and BOUNIN, P. 1964. Rev. Sci. Instr. 35, 481

CHAMBERLAIN, O. 1960. Ann. Rev. Nucl. Sci. 10, 161.

CHAMBERS, E.S. 1964. Rev. Sci. Instr. 35, 95

CITRON, A. et al. 1959. CERN. 59-8

COGGESHALL, N.D., 1947. J. Appl. Phys. 18, 855.

CRANBERG, L. 1951. AECU-1670 (Unpublished)

ENGE, H.A. 1959. Rev.Sci. Instr. 30, 248.

ENGE, H. A.1964. Rev.Sci. Instr. 35, 278.

EVANS, R.D. 1955. The Atomic Nucleus (McGraw Hill, publ.) p.589.

HUBBARD, E.L., and MacKENZIE, K.R., 1952. Phys. Rev. 85, 107.

LIVINGSTON, M.S. and BETHE, H.A. 1937. Revs. Mod. Phys. 9, 261.

LUCKEY, D. 1961. Techniques of High-Energy Physics, ed.D.M. Ritson.

(Interscience Publishers) p.403

MATHER, R.L. 1951. Phys. Rev. 84, 181.

MATHER, R.L. and SEGRE, E. 1957. Phys. Rev. 84, 191.

MOORE, R. B. 1962. PhD. thesis, McGill University (unpublished)

PENNER, S. 1961. REV.Sci. Instr. 32, 150.

DE RAAD, B. 1963. CERN- 63-3

RICH, M., and MADEY, R. 1954. UCRL 2301 (unpublished)

STERNHEIMER, R.M. 1959. Phys. Rev. 115, 137.

STERNHEIMER, R.M. 1960. Phys. Rev. 117, 485.

STERNHEIMER, R.M. 1960. Phys. Rev. 118, 1045.

TOLMAN, R.C. 1950. The Principles of Statistical Mechanics, (Ox. Univ. Press)

WILSON, R.R. 1941. Phys. Rev. 60, 749.